Institute of Physics, Wrocław University of Technology
Technische Physik, Universität Würzburg

PhD Thesis

Optical properties of elongated nanostructures in III-V semiconductors

Anna Musiał

Supervisors: Prof. Dr. Jan Misiewicz
Prof. Dr. Alfred Forchel

Wrocław, 2013

I would like to acknowledge and express my gratitude to Prof. Dr. Grzegorz Sęk and all other people who contribute to this dissertation for their help, assistance, motivation, inspiration and keeping fingers crossed. This work has been supported by the Foundation for Polish Science (FNP) and Deutsche Forschungsgemainschaft (DFG) – COPERNICUS Award.

Contents

Motivation

Fundamental changes in electronic and optical properties of semiconductor structures due to quantum confinement result in observation of new physical phenomena and extraordinary application potential. Carriers become confined if a potential well is formed due to the band gap difference of adjacent materials. Depending on the spatial arrangement of the respective materials, structures of different dimensionality can be created. The 3D confinement seems to be the most beneficial for some of the optoelectronic applications, e.g., light sources. Superior performance of nanostructure-based devices has been predicted theoretically [Ara82] and proven experimentally many times afterwards [Gru02]. Decreased dimensionality of the active region offers advantageous output characteristics, i.e. higher characteristic temperature, overall better temperature stability, lower threshold current density, improved modulation bandwidth and wider range of spectral tuneability. These engineering opportunities are developed in two directions, i.e. exploiting new materials (alloys and multinary compounds) and different nanostructures geometries. Devices for spectral range most preferably coinciding with minimal telecommunication fibre losses and dispersion (i.e. at 1.3 and 1.55 μm), as well as with controllable additional characteristics (e.g., polarization state of the generated electromagnetic wave), are desirable. Further advantage would be to generate radiation with required properties by the active region engineering, without the necessity of additional post-generation signal processing. The latter would always make the light source less compact, increase the fabrication costs and cause additional losses. That can be crucial in novel photonic devices based on single photon generation and in realization of quantum protocols, where losses lower significantly the probability of success, increase the number of realizations necessary to gain sufficient level of fidelity and prevent easy scalability of quantum networks.

Generally, there are two important groups of applications with contradicting requirements. The first one concerns devices whose performance depends on characteristics of individual quantum dots (QDs) like, e.g., novel photonic devices such as single and entangled photon sources or nanolasers with ultimately single or a few dot active region. In this case the important requirements with respect to self-assembled nanostructures are: low planar density, high oscillator strength of fundamental optical transition and significant separation of the confined energy levels. The main goal is to ensure purely single photon emission, preferably with a very short radiative lifetime important for a high repetition rate of the source and emission in the spectral range where the single photon counting can be

efficiently performed. On the contrary, quantum dot ensemble-based devices, such as lasers or optical amplifiers, exhibit a need for high nanostructure surface density, allowing for high gain and simultaneous emission of a huge number of photons in the active region, necessary for reaching the stimulated emission conditions. In the case of tuneable laser sources and optical amplifiers, spectral response functions with large inhomogeneous broadening characteristic for quantum dot ensembles can be an additional advantage.

The structures investigated in this work are examples of these two trends. GaAs-based large quantum dots exhibit increased oscillator strength of excitonic transition due to the enlarged coherence volume beneficial for more efficient interaction with light. This enabled achieving for the first time the strong coupling between a single exciton and a single photon in a micropillar cavity [Rei04]. This was a very important step towards quantum information processing applications, requiring coherent control of a quantum state for quantum networks and data transmission [Cir97, Ima99, Khi06] as well as photonic circuits and optical switches [Eng12, Bos12]. The emission range of such dots coincides with the maximum quantum efficiency of many silicon-based detectors, which are very efficient and outperform other detectors with regard to the signal to noise ratio, allowing sensitive spectroscopic probing of single dot properties. The surface density of these nanostructures is on the order of $10^9/cm^2$, which simplifies greatly the isolation of single quantum dot (SQD)emission lines.

The second group of investigated structures is based on InP substrate which ensures room temperature emission in the wide spectral range of 1-2 μm [Rei07], covering two main telecommunication windows by just tuning the amount of deposited quantum dot material (InAs) [Sau05]. Their surface density is very high - on the order of $10^{11}/cm^2$ – which, together with rather large nanostructure sizes (largest dimension exceeding 100 nm), result in surface coverage above 50%, implying high gain in laser applications. These structures are strongly asymmetric (lateral aspect ratio - LAR - exceeding 5) and because of that are called quantum dashes (QDashes). This property makes them very prospective also in view of polarization properties engineering. The geometry of InAs/InP nanostructures is very sensitive to growth parameters and hence fabricating structures from almost symmetric and relatively uniform to highly non uniform ensembles of quantum dashes is feasible [Bra02, Gil10, Gon00, Sri09, Sti03]. They can also be candidates for demanded single photon emitters at 1.55 μm, but the non-classical emission has not been proven yet and more detailed study of single quantum dash (SQDash) properties is required. This will partially be covered within the presented thesis.

The goal of the performed experiments was to investigate in a systematic and comprehensive way the optical properties of those two groups of nanostructures of practical relevance. These were experimentally determined on both the whole nanoobjects ensemble and on a single nanostructure level. The obtained results can help understand the physics behind previously observed improved device performance as well as verify their potential for applications, and can reveal possibilities for new ones. Both groups of QD-like structures are very interesting from the point of view of the fundamental physical properties, as they differ significantly from standard quantum dots. The main differences are: broken in-plane symmetry, relatively large overall nanostructure size (volume) which weakens the strength of quantum confinement, changes the oscillator strength of optical transitions and alters the relative importance of Coulomb correlations. Because of that distinctive optical properties, especially regarding the polarization of emitted radiation and exciton decoherence, are expected and need to be verified experimentally. Both groups of investigated nanostructures differ essentially from each other in the depth of quantum confinement, which needs to be taken into account for the proper interpretation of the experimental data, which will be further supported by corresponding theoretical modelling in the framework of **k·p** formalism.

The detailed objectives of conducted research were as follows:

- to investigate the strength and the spatial character of the carrier confinement
- to describe the impact of the confinement regime and anisotropy on the wave function extension and symmetry
- to determine experimentally the polarization properties of emission and to verify existing theoretical predictions for asymmetric nanostructures (and the effect of both in-plane and the cross-section sizes)
- to identify the main photoluminescence quenching and decoherence mechanisms in order to verify the expected higher robustness of excitons confined in the investigated structures
- to study the Coulomb correlation effects and many body phenomena, i.e. identify the excitonic and biexcitonic emission, determine such parameters as the biexciton binding energy and the fine structure splitting to describe the physical mechanisms driving their changes in the case of large anisotropic structures
- to distinguish between the optical characteristics inherent to asymmetric structures and these determined rather by the strength of the quantum confinement independently of the system symmetry
- to evaluate the usefulness of investigated structures in practical applications.

All the spectroscopic measurements have been conducted in Laboratory for Optical Spectroscopy of Nanostructures, Institute of Physics, Wrocław University of Technology (WRUT). The materials have been fabricated and characterized with respect to their structural properties in the Department of Applied Physics, University of Würzburg. The interpretation of the experimental data was supported by available structural data and theoretical modelling. The latter is not the original part of the thesis, as this has been performed by colleagues from Institute of Physics, WRUT, Janusz Andrzejewski, Paweł Machnikowski, Piotr Kaczmarkiewicz and Łukasz Dusanowski. It has been provided by courtesy and on the scientific collaboration basis, and only used as a reference for the interpretation of the experimental results, which constitute the original part of the work.

1. Introduction to quantum dashes

Quantum dashes are relatively new nanostructures and are still not fully described in terms of their physical properties. Also the distinction between QDashes and QDs is not clear and both terms can be found in the literature used for nanostructures with similar lateral geometry. In the presented work the term elongated quantum dots will be used for GaAs-based nanostructures which is justified by their relatively smaller lateral shape anisotropy - (LAR on the order of 2) and a posteriori experimentally proven domination of the excitonic effects over the ones induced by the asymmetric geometry. In view of the optical properties they are similar to standard QDs, with the enhanced volume being the main distinctive feature. For InAs/InP nanostructures most properties can be traced back to the pronounced shape anisotropy (LAR exceeding 5). This is the reason for referring to those structures as quantum dashes.

In this chapter expected electronic and optical properties of QDashes are described, especially these distinguishing them from standard QDs (Section 1.2) and beneficial for the applications (Section 1.3). This analysis is preceded by the description of physical mechanisms that can lead to growth of anisotropic nanostructures (Section 1.1) to indicate the possibilities of engineering the geometry of the nanoobjects and as a result their optical properties.

1.1. Growth

In this section different physical mechanisms that can lead to breaking the in-plane symmetry and formation of nanostructures elongated in one of the lateral dimensions during self-assembled growth in different material systems will be described. There are generally two indispensable conditions to obtain QDash structure: first of all some kind of anisotropy in the system that will favour the accumulation of deposited material in one of the lateral directions, secondly the growth parameters that enhance atoms migration and accumulation so that the anisotropy can become significant. Understanding of the growth mechanism enables to control the nanostructures size and geometry which further determines their optical properties.

One of the first reports concerning quantum dashes and actually using this term was published in 1996 by Utzmeier and co-workers [Utz96]. They reported the abrupt change in

the nanoobject geometry when the amount of InSb deposited material is increased during the growth by molecular beam epitaxy (MBE) method on semi-insulating InP (001) substrate. The critical thickness for observation of the shape transition in the described experiment was 3.2 InSb monolayers above which the nanostructures grew in semi-cylindrical shape elongated in [110] direction. The lateral aspect ratio was about 2.5, with typical in-plane sizes on the order of 100 x 40 nm. InSb/InP differs from other material systems in a very large lattice mismatch between the substrate and quantum dot material equal to 10.4 %. For typical growth conditions it results in highly strained QDs of rather small base diameter and increased height when compared to standard InAs quantum dots. Here, to enhance the surface migration of atoms, a pulsed mode of the MBE growth was used for group V elements. The observed shape change is explained by the minimization of the surface energy accompanied by the anisotropic strain field in the substrate. Due to the applied growth mode, enhancing atom migration, neighbouring islands can exchange material during the growth process. This results in a preferable formation of bigger dots instead of the increase in the surface density by growing more dots.

Nowadays the best known material system in which QDashes are formed is undoubtedly InAs/InP. Indium phosphide was chosen as a substrate for self assembled growth to shift the emission of standard InAs quantum dots to the telecommunication range of 1.55 μm. It has also been theoretically predicted to be a better choice for sources of entangled photons, offering much smaller exciton fine structure splitting (FSS) [He_08]. The spectral range of emitted radiation has been successfully shifted towards near infrared up to 2 μm at room temperature [Rei07, Sau05], but at the standard MBE growth conditions spontaneous formation of QDashes was observed. Generally, the growth on InP substrates is much more complex than in GaAs-based materials and the growth parameters influence strongly the nucleation process. As a result, a wide variety of different geometries, i.e., quantum dots, sticks, dashes and wires [Faf96, Sch02, Bra02, Li_02, Kim03, Sti03] can be realized. The reduced lattice mismatch of 3.4 % is the main reason of the growth being more sensitive to kinetics. Highly asymmetric nanostructures are preferentially formed in this material system due to the reconstruction of InP surface and the anisotropy of diffusion length of In atoms, which as a result accumulate preferentially in [1-10] direction. Relatively low lattice mismatch between InAs and (001) InP substrate enables formation of rather big nanoobjects, with length on the order of 150 nm and lateral aspect ratio which can easily exceed 5. Another result of the reduced strain is enhanced sensitivity of final nanostructure geometry to any

anisotropy of the system. It is actually very challenging to restore full in-plane symmetry in this material system in MBE growth and different approaches are being developed to achieve this goal: varying the growth temperature, lattice mismatch or arsenic growth mode (As_2 vs. As_4) as well as using additional thin layers in between quantum dot formation process [Bra02, Sti03, Kim05, Sri07, Dup08].

As QDashes reveal both advantageous application performance and interesting fundamental properties which provide unprecedented conditions for testing quantum electrodynamics phenomena, anisotropic geometry has been also explored in GaAs-based nanostructures, taking advantage of the well established technology and efficient low noise Si-based detection systems. It occurred being technologically challenging but still large (20-30 nm x 50-80 nm) slightly elongated (LAR around 2) QDs could be obtained in InGaAs/GaAs material system [Löf06]. Increasing quantum dot size was possible in that case due to the indium content reduced to 30 %. As a result, the strain is decreased due to smaller lattice mismatch between the quantum dot material and the substrate (on the order of 2 %). This increases both the critical thickness for three-dimensional island formation and the following QD size. Additionally, low-strain growth conditions enable the surface anisotropy to play a role and distinguish between two in-plane crystallographic axes. It favours the accumulation of deposited material in [1-10] direction as opposed to standard, highly strained higher In content ($x = 0.5 \div 1$) InGaAs quantum dots, which are rather symmetric and small, ensuring strong quantum confinement [Leo98, Lia98, Löf06].

All previously cited results concern strained systems taking advantage of Stranski-Krastanow growth mode. It has been shown that QDashes can be also obtained in an unstrained system, when droplet epitaxy method introduced by Koguchi [Kog91] is utilized [Jo_10]. In this self-organized process isotropic QDs are formed, reflecting the in-plane symmetry of gallium droplet, which constitutes a seed for quantum island material accumulation. High symmetry of the following structures is influenced neither by growth temperature nor pressure during crystallization process. Elongation of nanostructures is in that case obtained by thermal annealing after nanoobjects formation and becomes more pronounced as temperature is increased [Jo_10]. As a result, QDashes with LAR up to 3.5 and length on the order of 100 nm are formed preferentially in the [-110] crystallographic direction to minimize the total free energy. An additional advantage of the annealing process is an increase in the crystalline quality, resulting in enhanced emission. Experimental observations of QD-QDash shape transition are explained by the anisotropy in the surface

step energy formed due to the surface reconstruction, which starts to play a role after thermally-induced atom migration.

The presented examples show that the in-plane rotational shape symmetry of the QD-like structures in III-V material systems can be broken if only there exists some kind of surface anisotropy in the substrate, favouring one of the crystallographic directions during growth, e.g., difference in atom migration length. This can be a result of the symmetry of crystal plane, which can be further modified during the surface reconstruction process. Fulfilling that condition is sufficient to obtain slightly elongated nanostructures with LAR in the range of 1-2. Further increase in the shape anisotropy can be obtained by enhancement of the atoms migration during growth process and weakening the strain in the system, which increases the sensitivity of the final nanostructure geometry to the inherent system anisotropies. The former can be realized by the growth conditions and the latter by properly choosing the materials of the QD and substrate such that the lattice mismatch between them is decreased. This results in highly asymmetric nanostructures (LAR up to 5) and can be realized in different growth techniques and material systems as has been shown on the presented examples.

1.2. Electronic and optical properties

The QDashes differ significantly from the standard QDs when it comes to geometry which is rather flat, with a lens-shaped, trapezoidal [Mis04] or triangular cross section [Sau05] and a substantial in-plane anisotropy (reported LAR values are in the range of 2 - 5 [Sau05, Cha09, Sri09, Gil10]). In this section resulting modifications of electronic structure, in comparison to QDs, and expected specific optical properties will be discussed. At first, a general description of fully confined system as a starting point for further considerations of QDash characteristics is given. There are predicted the trends in the physical property changes with increasing the in-plane shape anisotropy of the nanoobject. The methods of electronic structure calculations are reported and their usefulness and appearing difficulties in application to the QDash structures are pointed out. Exemplary results are presented in the case when the actual calculations for elongated QD structures or some preliminary experimental data are available in the literature. For example, there exist some theoretical predictions suggesting that the interaction with the solid state host material should be weaker for larger nanostructures exhibiting weaker confinement. This is very important for practical

reasons and make QDashes very promising nanostructures to reduce the decoherence processes. It is studied experimentally in the main part of the thesis and therefore a fragment of the theory of open systems which is indispensable for proper data interpretation is enclosed in Section 1.2.4. Different mechanisms of interaction between the carriers confined within the quantum structure and the environment are mentioned and some predictions are made on how their effect is going to change for the case of QDashes.

1.2.1. Carrier confinement

The first thing that need to be clarified for QDashes is the system dimensionality. It was not obvious at the early stage of research as they revealed some features characteristic for zero-dimensional nanostructures and some others making them similar rather to quantum wires (QWires) [Rei07, Der04]. This issue is addressed in this section where at first the carrier confinement in three dimensions specific for QDs is described and then its validity when it comes to QDashes is discussed. Next, the quantum confinement is analysed in more details as its strength can significantly influence the optical properties and will be important to properly interpret the experimental results presented in the main part of this thesis.

Three dimensional quantum spatial confinement results in full energy quantization and leads to atom-like spectra with sharp single absorption/emission lines corresponding to transitions between discrete energy levels grouped into shells, as higher energy levels are appearing. As a consequence, the momentum space is highly degenerated since the carriers cannot move freely in any of the spatial directions and, regarding the optical transitions, the momentum difference between electron and hole is not an issue any more. Discrete optical spectrum is an evidence of three dimensional quantum confinement. The basic changes in electronic structure of a quantum dot with the material system and size can be easily deduced based on the solution of Schrödinger equation for one dimensional and rectangular quantum well (QW) with an infinite barrier:

$$E = \frac{n^2 \hbar^2 \pi^2}{2ma^2} \qquad (1.1)$$

where: n is a natural number enumerating the energy levels, m is the carrier mass, a is the width of the potential well and $\hbar$ is the reduced Planck constant. As can be easily seen when the well width is increased (the QD is getting bigger), the ground state energy is lowered (the emission shifts towards longer wavelengths) and the energy level separation is decreasing

(more energy levels can be confined within a given QD). The choice of material system determines the ground state emission energy via the band gap energy as well as the electronic structure via the effective carrier mass and the number of confined states via mainly the well width (dot size). In a real structure, with finite barriers, there appears another parameter influencing the entire structure of confined levels, namely the band offset between the dot and the barrier material which determines the potential depth for both carrier types (Figure 1-2). The size of QDashes is typically larger than for standard QDs which leads to decreased separation of confined energy levels. This lifts the optical transition isolation and increases the influence of higher energy states. It also enables the observation of higher energy shells as the number of confined levels within the nanoobject is significantly increased and the electronic structure becomes much more complicated than for standard QDs.

One of the most important characteristics changing dramatically with the dimensionality of the system is the density of states. It describes a number of states n per unitary volume and elementary energy range dE. The standard definition of this quantity is as follows:

$$\rho(E) = \frac{dn(E)}{dE} \qquad (1.2)$$

This formulation is true under the assumption on the parabolicity of the energy dispersion. In the case of one-dimensional QWires the density of states has the following form (Figure 1-1):

$$\rho^{QWire}(E) \propto \sum_i \frac{1}{\sqrt{E - E_i}} \Theta(E - E_i) \qquad (1.3)$$

where Θ is the Heaviside function equal to 1 for non-negative and 0 for negative arguments, respectively and i numbers subsequent energy subbands. At energy equal to E_i the density of states has a sharp maximum with a high-energy tail.

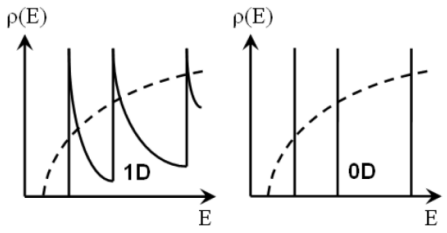

Figure 1-1. The density of states function for QWires (1D) and QDs (0D) - solid lines. For comparison the density of states for bulk crystal is shown - dashed line.

For zero-dimensional objects the density of states has a form of discrete delta-like function with sharp maxima at the energy coinciding with the energy of quantized levels E_i of quantum dot spectrum (Figure 1-1), which can be described in the following way:

$$\rho^{QD}(E) \propto \sum_i \delta(E - E_i) \qquad (1.4)$$

When compared to structures of higher dimensionality, the density of states integrated over the whole energy range is generally decreased but at a given energy E_i it is much higher - infinite in the ideal case and in reality lower e.g., due to the broadening related to finite carrier lifetime at respective energy state.

QDashes differ from this standard 0D picture due to strongly blurred density of states. The delta-like peaks are significantly broadened, which determines the optical properties of emission and following output characteristics of QDash-based devices. This quasi-continuous density of states can be traced back to the large inhomogeneity within the QDash ensemble and decreased energy level separation, what makes the density of states from different dashes and different states coincide in energy. This is why most of the studies concerning the gain analysis assume a wire-like density of states and show that the measured and simulated device performance are in good agreement, justifying this assumption [Der04, Wei05; Rei07]. The first qualitative discussion of the form of the density of states for QDash structures was carried out by J. H. Wei and K. S. Chan [Wei05] but the limiting factor of this analysis is the lack of both reliable structural data (sizes and their distribution among the ensemble) and model of strain, which can strongly influence the optical characteristics. QDashes are modelled as a one-dimensional structure but with rather big size fluctuation (up to 30 %), which in view of further studies, especially those of SQDash [Men03, Cha06], seems not fully realistic. Being aware of its qualitative character the research work presented was very pioneer and important for understanding the QDash uniqueness and pointing out their application advantages in comparison to structures of higher dimensionality. Further amplified spontaneous emission measurements as well as gain modelling indicate similarity to QWire-like density of states, which can overlap with continuum of states in the wetting layer (WL) for both type of structures [Rei07]. This results in ultra-wide gain which can be even three times broader than for QW in the case of InAs/InP material system. Later study on SQDashes revealed fully quantized energy levels [Sal05, Men03, Cha06], similarly to QDs. On this basis QDashes are categorized as quasi-zero-dimensional objects.

Once the dimensionality of the QDash structures is established, the issue of the strength of the quantum confinement need to be addressed. It influences the importance of

Coulomb correlations as well as the oscillator strength of optical transitions. The confinement strength is determined by the nanostructure volume, which is enlarged in the case of QDashes, and is expected to be the cause of further differences between them and common QDs. Generally two regimes of quantum confinement can be distinguished, i.e. the weak and strong one. The measure of the quantum confinement strength is the inter-level spacing of confined energy levels (Figure 1-2). Other characteristic energies in the system, responsible for different physical properties, are also marked in Figure 1-2 to establish the definition. The difference between the ground state energy of the QD and the energy of the substrate/barrier band edge is further referred to as the localization or activation energy and plays a role when the carrier escape mechanisms are discussed (Section 3.1.2, 3.2.2 and 4.1.2).

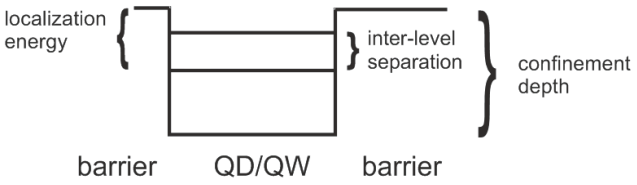

Figure 1-2. The scheme of 1D potential well with two confined levels and characteristic energies marked.

The important parameter to evaluate the strength of the quantum confinement more quantitatively, is the ratio between the physical nanostructure volume and the exciton coherence volume (defined by exciton Bohr radius of respective bulk material). The second criterion can be expressed in terms of energy and concerns the relation of the inter-level energy separation to the electron-hole Coulomb interaction energy (exciton binding energy) [Bry88, Sug95, And99, Mas02]. The confinement is considered as strong if QD volume is much smaller than the exciton coherence volume and the distance between adjacent confined energy levels exceeds the Coulomb energy. That is usually the case for small QDs of a few to no more than 10 nanometer diameters (depending on the QD material). The situation changes when QDashes are considered, as the change in the geometry is accompanied by the increase in the volume (dimensions on the order of single, a few tens and over hundred nm for height, width and length, respectively) and the intermediate or even weak confinement regime is expected. As far as the energy criterion is considered, for QDashes the inter-level energy separation is typically on the order of a few to above 10 meV [Mis04, Wei05, Mar13, Kac12, Syp13] comparable to the exciton binding energy (10 - 25 meV) [Vur01]. It shows that, whether the weak confinement regime is reached depends strongly on the exciton Bohr radius

which differs strongly between III-V materials (10 - 35 nm) [Ada04]. For truly weak confinement, only the centre-of-mass motion of the exciton is quantized [And99], Coulomb correlations dominate over the quantum confinement effects and determine the wave function extension. As a result the role of shape asymmetry is actually diminished, which results in the lifting of the anisotropy of optical properties. If a weak confinement regime is reached, increasing QD size results in the enhancement of the oscillator strength of excitonic transitions due to the increased coherence volume for light-matter interaction [Wim06, And99], which is beneficial for efficient light sources and quantum electrodynamics experiments. This shows that the physical properties of the structures with the same dimensionality can differ essentially as a result of confinement strength. QDashes are similar to QDs in their quasi-zero-dimensional character, but they can differ significantly in the strength of quantum confinement and the role of Coulomb correlations is much more important.

1.2.2. Electronic structure calculations

To predict and understand the optical properties of a nanostructures the modelling of their electronic structure is necessary. The methodology of calculating the electronic structure and the following optical properties of QDashes is as a whole inherited from QDs, where various effective mass [Cus96], perturbational effective mass [Fon98], 8 band **k·p** [Jia97, Jia97-1, Jia98, Pry98], empirical pseudopotentials [Mäd94, Can00] and tight binding methods have been applied. Hereafter, the most common approaches are briefly reviewed, pointing out those most useful and easily applicable to QDashes. The general picture of electronic structure is the same for both QDs and QDashes in a sense that quantized levels are grouping into shells, whose number and spacing depends on lateral size and shape of the nanostructure. The most important part of the modelling is to obtain a more realistic shape of the confining potential, for which a proper strain calculation is indispensable. The strain field is highly sensitive to QD size, shape and composition. It determines the piezoelectric fields, which in turn influence the energy spectrum of the nanostructure [Sch07, Sti99], the stronger the larger the nanostructure. All self-assembled nanostructures fabricated in Stranski-Krastanow growth mode are strained because the QD material is compressed, having larger lattice constant than the barrier which causes the displacement of atoms and enforced pseudomorphic growth of following layers.

There are generally two approaches to the strain calculations: continuous elasticity and atomistic models trying to apply methods well known from solid state physics, only with slight modifications to describe the energy spectrum of the nanoobject. The continuous approach is the extension of classical theory of elasticity, treating QD and surrounding material as continuous elastic media described by elastic constants. Its applicability to model nanoobjects is a little bit controversial and still under debate [Sch07, Sti99]. To reproduce the real structure and include strain-induced corrections to the confining potential part of the Hamiltonian, the total elastic energy is minimized by set of optimal displacements. In continuum mechanical model the total strain energy can be expressed in the following way:

$$U_{CM} = \frac{1}{2}\sum_{i,j,k,l} C_{ijkl}\varepsilon_{ij}\varepsilon_{kl} \qquad (1.5)$$

where: $\varepsilon_{ij} = \frac{\partial u_i}{\partial x_j}$ is the element of the strain tensor, $\boldsymbol{u}$ is the displacement vector and C are the respective compliances/elastic moduli. The most common example of continuum elasticity models is the **k•p** approach based on envelope function approximation and utilizing Bloch function basis. In the full **k•p** model the Hamiltonian is built up from 8 bands: electron, heavy hole, light hole and spin-orbit, all twofold degenerated due to spin and all coupled, which excludes analytical treatment and makes the problem solvable only numerically. The parameters of the model are extracted from bulk and treated as effective ones, sometimes with slight modification. The atomistic character of QD-barrier interface is not included, which is the main objection to the application of this theory to QDs. Despite that the usefulness of **k•p** model and good agreement between the results in comparison to more sophisticated and complex methods, trying to describe QD-like objects more accurately, has been undoubtedly proven [Sti99, Sch09]. One of the possible explanations of this phenomenon is the lack of exact structural data (in terms of geometry, overall composition and composition distribution), forcing the need to assume or extrapolate some input parameters required in atomistic modelling. Furthermore, the possibility that the details of atomic arrangement are smeared out due to intermixing effects, alloy fluctuations and other randomness in the structure makes the effective description sufficient to capture the most important characteristics of the system. The most problematic features of the continuous elasticity models are the fixed number of Bloch functions (8) used for wave function expansion and arbitrary matching conditions for the envelope functions at the heterointerfaces. In the case of Stranski-Krastanow QDs, the WL accompanying the nanostructures formation cannot be

modelled properly due to its exceptionally low thickness in a single nanometer range. Another drawback is the restriction to the Brillouin zone centre, as the **k•p** model is optimized to model energy dispersion in the vicinity of critical points. On the other hand, this approach enables modelling a QD structure of any shape, size and composition. It is straightforward how to include strain and piezoelectricity (also of the second order) as well as valence band mixing and interband interactions in the model [Sti99, Sch07, And10, And13]. All this can be realized with much less computational resources than in the case of atomistic-based methods.

In atomistic approaches the elastic energy is described in terms of stretching and bending interatomic bonds between individual atoms, summed over the whole region of interest. The parameters of the model are microscopic and derived through first principle methods from the atomistic structure of the QD. Those methods are computationally very challenging and time consuming and because of that can be utilized only for small QDs and are almost inapplicable in the case of QDashes. The most advanced atomistic based approaches are semi-empirical pseudopotential theory proposed by Kim et. al. [Kim98], empirical pseudopotentials developed by Zunger and co-workers, very useful in capturing the material-dependent trends in optical properties [He_08] and tight binding approach combined with configuration-interaction method [Zie10, Zie12].

In principle, the atomistic-based methods potentially have a better accuracy than **k•p** models, but require quite exactly known input parameters, which is one of the limitations of this approach. This is the reason why the final results are similar to those obtained by applying 8-band **k•p** calculations but both differ substantially from one band effective mass theory, which is certainly insufficient for proper description of QD systems. The direct comparison of different approaches to model strain in nanostructures was done by Bimberg and co-workers [Sti99]. Results obtained by those two strain models differ only slightly in calculated strain distribution, which influences the energy levels, the transition energies, polarization and oscillator strengths of excited states transitions. The low accuracy of input parameters for valence force field model needs to be pointed out and at the end this is the source of main differences between the models and not their different character, i.e., continuum vs. atomistic. It seems that the continuum mechanical models are closer to reality and the more advantageous the larger the investigated objects are.

In the first attempt to model the absorption of the InAs/InP QDashes a non fully discrete energy spectrum was suspected [Mis04] but later SQD spectroscopy experiments dispelled those doubts [Men03, Cha06]. Simplified theoretical model taking into account only

heavy hole transitions and utilizing one band effective mass **k•p** Hamiltonian with effective masses, energy gap and potentials renormalized with strain and excitonic effects included only via energy shift of the spectrum as a whole enabled to satisfactorily reproduce the experimental emission spectrum of QDashes. Theoretical modelling so far has focused either on the prediction or explanation of the InP QDash-based device performance using either QWire-like density of states [Der04] or simplified **k•p**-based quantum box models [Hec09]. Not much attention has been paid to construct and investigate a more realistic QDash model in view of fundamental characteristics, e.g., strength and spatial character of confining potential or polarization properties of emission and the actual impact of geometry on the optical properties, i.e., the distinction between shape and symmetry influence. Those issues are experimentally addressed in the following thesis together with citing the respective **k•p**-based calculations supporting the interpretation of the experimental data.

Electronic structure calculations of QDashes reported so far in the literature were mostly done in the **k•p** framework. In the case of QDashes, the application of continuous elasticity models is much more justified than in the case of standard QDs, due to their increased physical volume. Simultaneously, the atomistic modelling is rather difficult to perform because of the large number of atoms that constitute individual QDash structure (40 nm base diameter QD consists of about 1 million atoms and the average dimensions of a QDashes are even bigger), which increases strongly the computational effort and complexity of the numerical problem. One of the very important issues in electronic structure calculations is the number of subbands that need to be taken into account, which is strongly dependent on the regime of quantum confinement defined in the previous section. In the strong confinement regime the ground state is composed mainly of the lowest-energy subband states, as opposed to the case of large nanostructures, in which higher energy levels need to be included even in the construction of the ground state wave function. In the case of QDashes a high subbands mixing degree and large number of levels need to be accounted for. Due to the increased lateral size of QDash structures, much more energy levels (shells) are expected to be confined within the nanostructure, as the energy level spacing should be decreased. A model of a QDash is either trapezoidal [Mis04], lens-shaped [Rud05] or triangular [Sau05] in cross-section - all realistic in view of structural data and the choice between them is rather the matter of the microscopic images and the interpretation of their contrasts. The most important difference between various cross-sectional geometries is the inter-dash interaction, which can have an impact on the emission properties of QDash-based devices in the high excitation

regime. It has been evaluated [Ryc13] that in the case of cross-sections with sharp tip at the top, the wave function is rather localized in the top part of the QDash and the inter-dash interactions/coupling are negligible even for nanostructures adjoined at the bottom.

1.2.3. Excitonic complexes

Due to the three dimensional spatial confinement in QD-like structures electrons and holes are so close to each other that their Coulomb interactions are strongly enhanced. Such correlated electron-hole pair is called exciton by analogy to excitons in bulk crystal. In the extreme case of a strong quantum confinement it can even prevail over the carrier correlation and exchange interactions. Because of that carriers can become trapped in energetically unfavourable spatial arrangement in which Coulomb repulsion is stronger than attraction but cannot overcome quantum confinement effects.

Depending on the type and number of carriers trapped within the QD various excitonic complexes can be formed. The simplest ones, involving the lowest number of carriers and hence the most probable, are: neutral exciton (a correlated electron-hole pair), trions formed of three carriers (a negatively or positively charged exciton - with additional electron or hole, respectively) and neutral biexciton (composed of two electrons and two holes). All of them can be spontaneously formed in QDs, but in standard structures, without intentional doping in adjacent layers, the probability of neutral complexes formation is much higher than for charged ones.

What is easily probe in the experiment is the recombination energy of excitonic complexes. This is the energy difference between the initial i and final f state of the QD within the recombination process and equals the energy of the emitted photon in the case of the radiative recombination. The main contribution to the recombination energy originates from the QD material band gap energy but it can be tuned even up to hundreds meV range by the size of the QD and again the dependence is different for various excitonic complexes. The driving factor of those changes is the size dependence and the relative values of Coulomb and exchange energies between carriers of both the same and different types. The recombination process can have radiative (the energy is released as a photon) or non-radiative character (the energy is transferred to the crystal lattice or to another carrier to promote it to higher energy level). The topic of decoherence mechanisms of excitons in QDs is covered by the next section.

Another characteristic energy important in the description of excitonic complexes is the binding energy. It is strongly enhanced in nanostructures (in comparison to bulk crystal) as a result of stronger overlap of electron and hole wave functions due to the spatial confinement. The binding energy Δ is defined with respect to the ground state of dissociated excitonic complex and is equal to the amount of energy that one has to add to the system to destroy the respective excitonic complex:

$$\begin{aligned}
\Delta(X) &= \left(\varepsilon_o^e - \varepsilon_o^h\right) - E(X) \\
\Delta\left(X^-\right) &= \left(\varepsilon_o^e + E(X)\right) - E\left(X^-\right) \\
\Delta\left(X^+\right) &= \left(-\varepsilon_o^h + E(X)\right) - E\left(X^+\right) \\
\Delta(XX) &= 2E(X) - E(XX)
\end{aligned} \qquad (1.6)$$

where the symbols in parenthesis denote the type of the complex (X - stands for a neutral exciton, XX for a biexciton and $X^{+/-}$ for a trion) and $\varepsilon_o^{e,h}$ are the single particle energies of electron or hole, respectively. The binding energy of each of the excitonic complexes depends on the size of the QD and in the case of very small nanoobjects it can even become negative, when the carriers are so strongly localized spatially that they cannot form energetically favourable complex and are trapped in an antibinding state. The negative biexciton binding energies were reported [Sti01, Nar05, Cha06] also for very large nanoobjects and in that case it can be explained by the decreasing overlap of electron and hole wave function enhanced by the piezoelectric effects increasing with the QD size. Only the biexciton binding energy is easily accessible experimentally. It can be directly measured from the emission spectra as an energy difference between the exciton and biexciton emission energy. In the standard III-V QDs this energy is in the single meV range [Mas02, Mic03].

The identification of respective excitonic complexes is an important issue in SQDs investigation. The easiest way to distinguish between them experimentally is to examine the power dependence of emission intensity and polarization of individual emission lines. Another approach is to apply magnetic field, which lifts the degeneracy of different spin configurations and can mix them, which enables the observation of states that cannot be detected optically otherwise, because they do not couple to the light. Study on charging the QDs with individual carriers by electric field tuning can also provide information about specific excitonic complexes by creating conditions favouring formation of only the selected ones. The time correlation between photons emitted as a result of different excitonic complexes recombination can be measured directly in Hanbury Brown and Twiss experimental configuration. This is another way to prove excitonic complexes origin of the

same QD. Application of external fields and correlation spectroscopy measurements are beyond the scope of presented thesis and because of that are not described in more details.

The dependence of the emission intensity on the excitation power for various excitonic complexes can be predicted based on the rate equations describing the changes in the occupation probabilities due to generation/recombination processes in the cascade evolution model [Dek00, Sen05, Bar07]:

$$\frac{dp_i}{dt} = G(t)\,p_{i-1} + \frac{p_{i+1}}{\tau_{i+1}} - \frac{p_i}{\tau_i} - G(t)\,p_i \qquad (1.7)$$

where: p_i is the probability that *i-th* state of the system is occupied, *G(t)* is the generation rate and τ_i are the characteristic lifetimes of respective states. The changes in the occupation are of two types: promoting from the lower *i-1* level and recombination from the higher *i+1* level - first two terms on the right-hand side of equation above. The next two terms describe processes leading to decrease of the occupation probability p_i. Such analysis is valid under the assumption that transitions within the ladder of states are possible only between adjacent levels, which is justified as the other transitions are much less probable. Another simplification of this model is the disregard of the fine structure of excitonic complexes related with different possible spin configurations, which are in general not degenerated. This splitting does not need to be considered in all the cases when it is not resolvable experimentally and only the effective response of all spin states is measured. To calculate the emission intensity dependence on the generation rate, the stationary conditions need to be assumed, i.e. the left-hand side of above equation equal to 0, meaning that the occupation probabilities do not change in time. This is the case when the system is excited in a continuous way with constant excitation power. The system reaches an equilibrium in which the balance between generation and recombination processes is established. The problem simplifies greatly as instead of a set of differential equations only the set of linear equations needs to be considered. Additionally, the normalization condition for the occupation probabilities for all *N* states included in the model must be fulfilled:

$$\sum_{i=0}^{N} p_i = 1 \qquad (1.8).$$

With this restrictions the dependence of occupation probabilities on the generation rate can be determined:

$$p_i = p_0 G^i \prod_{j=1}^{i} \tau_j ,$$

$$p_0 = \frac{1}{1 + G\tau_1 + G^2\tau_1\tau_2 + ... + G^N \prod_{j=1}^{N} \tau_j} \qquad (1.9)$$

To translate it into the language of experimentally accessible quantities, one has to notice that the generation rate can be assumed proportional to the excitation power. In an ideal situation of 100 % efficient generation each photon creates one exciton but in practice due to losses these numbers are never equal. To evaluate the emission intensity *I* it is enough to remind that it is proportional to the oscillator strength of analysed transition, which in turn is equal to the product of the level occupation probability and its recombination rate (inversed lifetime). What is worth mentioning, in weak confinement regime, the bigger the QD is the larger the oscillator strength of respective transition. In the case of nanostructures of increased volume the emission intensity should be in general stronger than for standard QDs. This was argued theoretically when the limit of weak confinement and resulting center of mass quantization is considered [And99] and was indirectly proven experimentally as it helped to create conditions beneficial for strong coupling realization [Rei04]. Under these assumptions the expressions for the generation rate *G* (excitation power) dependence of the emission intensity *I* derived from the rate equations can be written as:

$$I_i \propto \frac{p_i}{\tau_i} = \frac{G^i \prod_{j=1}^{i-1} \tau_j}{1 + G\tau_1 + G^2\tau_1\tau_2 + ... + G^N \prod_{j=1}^{N} \tau_j} \qquad (1.10).$$

This is enough to capture the most essential characteristics of the simplest excitonic complexes in low and intermediate excitation power range, for which the higher order processes are less probable. For low excitation powers (but high enough to enable formation of respective excitonic complex) the emission intensity dependence is approximately linear for exciton, quadratic for biexciton and in-between (superlinear) for trions and other charged states. The example of an exciton-biexciton cascade is discussed in details in Section 3.2.1.

Another way of distinguishing between different carrier configurations confined within the quantum dot is to examine the polarization properties of emission. First important observable is the degree of linear polarization of emission (DOP) defined as:

$$DOP = \frac{I_{\parallel} - I_{\perp}}{I_{\parallel} + I_{\perp}} \qquad (1.11)$$

where I is the intensity of light polarized parallel and perpendicular to selected direction. For QDs emission the degree of linear polarization reflects the anisotropy of confining potential. The elliptical polarization of the excitonic transition is a result of increased heavy-light hole mixing because the light hole admixture introduces opposite circular polarization [Kou04]. The direction of the polarization axis can differ strongly from dot to dot. It is mainly determined by the local strain and the shape of a QD. In the case of asymmetric structures the elongation direction (usually coinciding with the crystallographic axis) is preferred but it can be modified even in the range of 20° by the local strain field [Ohn11]. This polarization direction reflects the phase of valence subbands coupling element. To fully understand the polarization properties of emission the fine structure of respective excitonic complexes needs to be examined in details. In further considerations a mainly heavy hole character of the hole ground state is assumed, which is well justified in self-assembled QDs because of compressive strain increasing the light and heavy hole levels splitting. In the case of neutral exciton there are four possible spin configurations resulting in two optically active (bright) states with a total angular momentum equal to 1 and two dark (not coupling to the light field) excitons for which it is 2. When the quantum dot exhibits full in-plane symmetry and the electron-hole exchange interaction is neglected the exciton state is fourfold degenerate and all the states are eigenstates of the total angular momentum and are denoted as {|+1>, |-1>, |+2>, |-2>} (Figure 1-3). The emission of each of the optically active excitons is circularly polarized just like in the case of QW excitons.

This simplified picture breaks down when the exchange interaction of carriers forming the exciton is included. The general Hamiltonian of electron-hole exchange can be written as:

$$H_{ex} = -\sum_{i=x,y,z} \left(a_i J_{h,i} \cdot S_{e,i} + b_i J_{h,i}^3 \cdot S_{e,i} \right) \qquad (1.12),$$

where J and S denote the spin of the hole and electron, respectively.

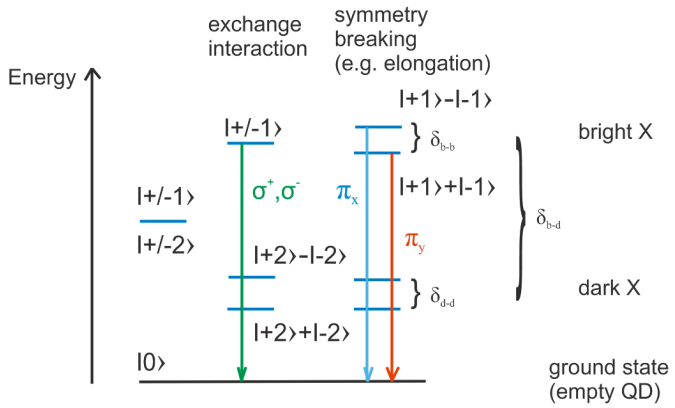

Figure 1-3. The scheme of exciton fine structure and the degeneracy of exciton levels, from left to right: for high symmetry QD without and with exchange interactions included, for QD with in-plane symmetry broken. Arrows indicate optically active transitions together with the polarization state of emitted radiation.

When the light hole admixture to the valence band ground state is neglected and the projection of the spins on the growth direction are chosen, the Hamiltonian can be rewritten in the angular momentum eigenstates basis as:

$$H=\frac{1}{2}\begin{pmatrix} \delta_{b-d} & \delta_{b-b} & 0 & 0 \\ \delta_{b-b} & \delta_{b-d} & 0 & 0 \\ 0 & 0 & -\delta_{b-d} & \delta_{d-d} \\ 0 & 0 & \delta_{d-d} & -\delta_{b-d} \end{pmatrix} \begin{matrix} |+1\rangle \\ |-1\rangle \\ |+2\rangle \\ |-2\rangle \end{matrix} \qquad (1.13)$$

with matrix elements related to the coefficients occuring in the general exchange Hamiltonian in the following way [Bay02]:

$$\begin{aligned} \delta_{b-d} &= 1.5\left(a_z + 2.25 b_z\right) \\ \delta_{b-b} &= 0.75\left(b_x - b_y\right) \\ \delta_{d-d} &= 0.75\left(b_x + b_y\right) \end{aligned} \qquad (1.14).$$

This Hamiltonian has a block-diagonal form as the bright and dark states do not mix with each other and the respective eigenenergies equal:

$$\begin{aligned} E_b &= \frac{1}{2}\left(\delta_{b-d} \pm \delta_{b-b}\right) \\ E_d &= \frac{1}{2}\left(\delta_{b-d} \pm \delta_{d-d}\right) \end{aligned} \qquad (1.15)$$

The inclusion of the exchange interaction lifts the degeneracy between dark and bright states and differentiates between two dark states which are mixed and are no longer eigenstates of the angular mometum independently of the system symmetry. To further split the bright excitonic states, lowering the symmetry of the confining potential is necessary. This symmetry breaking can be caused by QD shape anisotropy, strain-induced piezoelectricity [Gru95], interfacial symmetry lowering or underlaying crystal lattice intrinsic anisotropy (the two latter cause splittings in the single μeV range referred to as intrinsic fine structure splitting [Bes03, Bes05]). The FSS can also differ between the dots due to atomic scale randomness effects. This results in a broad distribution of splittings within the QD ensemble [Mli09]. This effect of symmetry breaking can also be introduced externally, e.g., by the application of magnetic field in the direction not coinciding with the symmetry axis, by rapid thermal annealing or by in-plane electric field [Vog07, Kow07, Kad10]. The lack of the in-plane rotational symmetry enables the anisotropic part of the electron-hole exchange interaction to play a role and to split the optically active excitonic states. This splitting is an important parameter both for fundamental study as a measure of confinement anisotropy and for applications, e.g. indistinguishable photon sources. For the latter the FSS unresolved spectrally, i.e. smaller than single exciton state emission linewidth, is required. On the other hand, for linearly polarized single QD-based lasers FSS large enough to ensure coupling between only one of the optically active excitons with polarized microcavity mode is advantageous. The FSS is generally in the μeV range, with the record value of 1 meV for III-V material systems observed by Finley and co-workers for strongly confined InAs/AlGaAs QDs [Fin02]. Splitting of the bright excitons is not the only effect of the reduced symmetry. Also these states are no longer total angular momentum eigenstates |+1> and |-1> but their linear combinations:

$$|X\rangle = \frac{1}{i\sqrt{2}}\left(|+1\rangle - |-1\rangle\right)$$
$$|Y\rangle = \frac{1}{\sqrt{2}}\left(|+1\rangle + |-1\rangle\right) \qquad (1.16)\cdot$$

Emission from these states is linearly polarized, with two orthogonal polarization directions coinciding with the crystallographic axis. If the valence band mixing, i.e., the admixture of

the light hole into the mainly heavy hole-like ground state is included, the bright exciton states are elliptically polarized with the polarization axis tilted with respect to the crystallographic direction and can be expressed as:

$$\left|\pm\tilde{1}\right\rangle = \sqrt{1-\beta^2}\left|\mp\frac{1}{2},\pm\frac{3}{2}\right\rangle + \beta e^{\pm 2i\Psi}\left|\mp\frac{1}{2},\mp\frac{1}{2}\right\rangle \qquad (1.17)$$

where β is the amplitude and ψ the phase of the valence subbands mixing and the values in the ket represent the electron and hole spin projections, respectively. Additionally, the smaller the light hole-heavy hole energy splitting, the larger the degree of mixing. Linear combinations of this bright exciton states constitute the neutral exciton eigenstates:

$$\left|\tilde{X}\right\rangle = \frac{1}{i\sqrt{2}}\left(\left|+\tilde{1}\right\rangle - e^{2i\theta}\left|-\tilde{1}\right\rangle\right)$$
$$\left|\tilde{Y}\right\rangle = \frac{1}{\sqrt{2}}\left(\left|+\tilde{1}\right\rangle + e^{2i\theta}\left|-\tilde{1}\right\rangle\right) \qquad (1.18)$$

where the angle θ is the deviation of the QD elongation axis with respect to the crystallographic axis, which is in general different than the angle ψ. Both linearly polarized excitonic transitions can be observed in the experiment if the detection is linear polarization-resolved and the spectral resolution of the setup is high enough. The FSS is one of the arguments that the observed emission line originates from the neutral exciton recombination. It can also evidence the excitonic and biexcitonic emission from the same QD. This is due to the fact that the biexciton itself does not possess the fine structure (it is just a single level) but it recombines to the final state of a neutral exciton having the fine structure. Hence, the biexciton emission line reflects the inverted fine structure of the exciton (opposite energy order of a given polarization components) but only if both lines come from the same nanoobject. Thus this fact can be used as a proof of a common source of emission if the emission energy of two lines exhibits an out-of phase oscillation as a function of polarization angle. The situation is much simpler for the trions in the ground state because the electron-hole exchange interaction vanishes due to parallel spins of two carriers (Pauli exclusion principle). This causes that the trion state is twofold degenerated independent of the symmetry.

To predict the exciton FSS for QDash structures at least two important effects need to be taken into account: the influence of size and elongation (geometry). There exist some theoretical predictions regarding the dependence of the FSS on lateral aspect ratio in the case of strongly confined QDs. However, the considered changes in the in-plane shape symmetry are rather subtle - far below the elongation range typical for QDash structures [Kad10]. The general tendency revealed by this study shows increasing FSS with more pronounced QD lateral anisotropy. In the case of QDashes it will be very interesting to separate the size and elongation contributions to the FSS. It has been shown that the dominant effect can be identified based on the FSS dependence on the exciton emission energy, but again for rather symmetric InAs/AlGaAs/GaAs QDs [Seg05]. FSS from -100 μeV up to 520 μeV have been measured and increasing size of the dots has been identified as the determinant of this trend, based on numerical simulations. With increasing size of the QD the shearing strain component is enlarged due to the lattice constant mismatch between the QD material and adjacent layers. This results in stronger piezoelectric fields and as a consequence a larger FSS. This leads to the conclusion that the FSS should increase with lowering the emission energy. Opposite trend has been predicted if the elongation of the structure (with conserved QD volume) is considered as the underlying cause of FSS changes. Some attempts have been taken to compare QDs and more asymmetric nanostructures in a form of quantum sticks or QDashes in InAs/InP material system but the results are far from being complete and are not very systematic, and most of the interpretation is still rather speculative [Cha06, Cha06-1]. The experimental results obtained by Chauvin and co-workers are in contradiction to the simple picture of the FSS value increasing with elongation of the nanoobject. They have not resolved exciton fine structure splitting for QDashes and at the same time measured FSS as large as 250 μeV for QDs, what excludes both the piezoelectricity and the elongation as driving factors of the FSS. The results are interpreted as reflecting the dependence of the splitting on the value of exchange energy after a model proposed by Tsitsishvili, assuming anisotropic lattice structure [Tsi01]. He concludes that the splitting increases with the exchange energy, which on the other hand increases strongly for smaller dots. This is related to the exchange energy dependence on quantum confinement, which can be responsible for higher sensitivity of excitons to the asymmetry of confining potential in the case of small QDs than for QDashes. For large nanostructures, exhibiting weakened confining potential, the exchange interaction efficiency is much lower. Abovementioned examples of the FSS measurements and calculations evidence that predictions on energy separation of bright

excitons are not easy in the case of strongly asymmetric nanostructures, as the asymmetry role depends strongly on the confinement regime and its exact value is the result of a trade-off between piezoelectric fields and QD elongation. To sum up, the FSS can be either smaller or larger than for standard symmetric QDs, depending on which factor becomes dominant for a specific system.

1.2.4. Exciton dephasing mechanisms

Epitaxial QDs are surrounded by semiconductor material, what is an important difference between those 'artificial atoms' and real atomic systems. Both can be in a a good approximation modelled as two level system but QDs cannot by treated as isolated one due to strong interactions with the environment. This coupling is a reason of a non-unitary evolution of the state of the dot, which is the main drawback whenever applications are considered. This is why studies on decoherence mechanisms are of great importance to predict on the application potential and to discover a way to minimize their influence. In general, the decoherence processes are of two types. First of them is a phase decoherence, also called pure dephasing, which does not lead to changes in occupations within the system. The second one is relaxation (decay) or amplitude decoherence of the quantum state, in which it is destroyed and some energy is released. The latter is changing the diagonal elements of the density matrix describing the system, and so its eigenstates, and the former is influencing only its off-diagonal part. The decoherence affects both charge and spin of the excitation of the QD. This is the reason why the optical properties of excitonic emission of QDs are determined not only by the electronic structure of the nanoobject itself but also by the environment, its character and the coupling to the carriers confined in QDs.

The main mechanisms of exciton relaxation are: recombination, interaction with phonons (discussed in details at the end of this section) and Coulomb interactions with other carriers (present in the same quantum dot, neighbouring quantum dots or in adjacent layers or confined on defects or other carrier traps etc.). At low temperatures the radiative recombination dominates but with increasing temperature the contribution of non-radiative processes (e.g., Auger recombination with promoting carriers to higher levels instead of creating a photon) increases and influences strongly the exciton dynamics. On the other hand, the population decay differs a lot depending on the excitation conditions. With increasing number of carriers in the system the broadening of the emission line increases due to the final

state damping by rapid relaxation of the multiexcitonic states (Auger or phonon mediated) in the presence of carriers in the QD excited states [Bor00, Usk01, Yua01, Bor02]. Those processes dominate exciton relaxation at low temperatures (typically below 30 K).

Another reason for a homogeneous broadening of emission line related to the presence of a large number of carriers in the system that comes into play at elevated temperatures (typically above 100 K) is the pure dephasing due to the interaction with delocalized carriers in neighbouring layers. At room temperature it becomes the predominant factor. It is important to notice that this mechanism is strongly confinement-dependent (values from 9 [Bor01] up to 25 meV [Bor00] have been reported), as the confinement depth influences the thermal carrier population of the WL/barrier. At elevated temperatures also the phonon-induced pure-dephasing comes into play, which indicates the important role of acoustic phonons.

The simplest approach to model the decoherence effects is to describe the exciton dephasing in the relaxation-time approximation in which the system decays exponentially to the equilibrium state. With this approach a measurable parameter, so called dephasing time (dephasing rate) is introduced. It indicates how fast is the decoherence and so the robustness of the system against the interaction with the environment and so evaluates it usefulness in practical applications. This is a general description which does not depend on the underlaying physical mechanism leading to the exciton dephasing. Essential assumptions are that the two level system approximation is applicable and the exciting light field is resonant with only one transition (ultra short pulse with narrow spectrum) and off-resonance with all the other and, furthermore, that the environment is a thermal bath without memory (Markovian approximation). Under those conditions the dephasing rate can be written as:

$$\frac{1}{T_2} = \frac{1}{2T_1} + \frac{1}{T'_2} \qquad (1.19),$$

where: T_2 (often called the dephasing time) describes the decay of the polarization, T_1 is the decay time of population of the excited state due to spontaneous emission (without interaction with an external light field) and T_2' is the pure dephasing time and describes the decay of macroscopic polarization due to elastic processes. Factor of two between the time decay due to elastic processes and radiative recombination originates from the fact that the population inversion is proportional to the excited state occupation probability and the polarization to the amplitude of this probability. What is evident from Equation (1.19) is that the radiative lifetime influences the dephasing time and as a consequence makes it strongly QD size

dependent. This is due to the fact that the radiative lifetime is almost constant and in the range of 1-2 ns in the strong confinement regime but decreases down to hundreds of ps with increasing dot size in the intermediate and weak confinement regimes, due to the increase in exciton coherence volume [Bel98]. The pure dephasing rate is also strongly confinement dependent. It increases linearly in strongly confined systems like CdSe nanocrystals [Sch93] and is dominated by a nonlinear part in the case of weak confinement (e.g., GaAs islands [Mas02] and CuCl nanocrystals [Ito91]).

In the following paragraph the phonon-induced decoherence, being the main source of dephasing in the case of epitaxial QDs, is discussed. The exciton-phonon coupling in QDs is increased in comparison to bulk because the quantization energy is comparable to phonon energy in the crystal lattice. Two regimes of exciton-phonon coupling can be distinguished. In the weak coupling regime exciton and phonon are still the eigenstates of the system and exciton-phonon coupling can be treated perturbatively. On the contrary, when the interaction is very strong, polarons - mixed states of exciton and phonon - are formed. From different phonon modes the longitudinal ones of both acoustic and optical types contribute mostly, with the dominance of longitudinal acoustic (LA) phonons due to their broad linear dispersion, in spite of a lower value of the coupling constant. Moreover, only the long-wavelength phonons are effectively coupled to carriers confined in QDs because the carrier energy is not sensitive to the band structure modulation on a scale much smaller than the size of the wave function extension [Gro05]. This is the reason for exponential cut-off in the carrier-phonon interaction if the harmonic confining potential is assumed. The cut-off frequency is inversely proportional to the wave function extension in a given direction (related to the QD size). For example, for a QD of a single nanometre sizes the cut-off energy is in the range of 1-2 meV. Generally, the phonon-induced dephasing time is proportional to the QD size and inversely proportional to the group velocity of phonon modes, which translates into linear and quadratic dependence on QD size for LA and longitudinal optical (LO) phonons, respectively.

The Hamiltonian of the system under consideration is composed of exciton, phonon and interaction parts. The interaction term can be written in a form:

$$H_{\text{int}} = \sum_{\vec{k};n,n'\geq 1} |n\rangle\langle n'| F_{nn'}(\vec{k})\left(b_{\vec{k}}^{+} + b_{-\vec{k}}\right) \qquad (1.20),$$

where n numbers the excitonic states and b^+ and b are the creation and annihilation operators of a phonon mode with wave vector $\boldsymbol{k}$, respectively, and F is a measure of the strength of the coupling. There are three main mechanisms of exciton-phonon interactions [Gro05], i.e.,

Coulomb interaction with the lattice polarization due to a relative displacement of charged sub-lattices in polar compounds (LO phonons) or with crystal deformation-induced piezoelectric field (LA, transversal acoustic phonons), and via deformation potential when the electronic structure shifts because of lattice deformation (LA phonons). The coupling via deformation potential is related to the deformation-induced shift of the energy bands, which is proportional in the leading order to the relative volume change. The deformation itself is a result of absorption - the presence of photogenerated carriers distorts the crystal lattice. Only the longitudinal phonon modes can modify the volume of the unit cell. The coupling constant is proportional to the deformational potential and the form factor containing information about geometry of the confinement and the properties of the wave functions. The piezoelectric coupling is a result of polarization field generated by a phonon propagating in the piezoelectric medium. This polarization field influences carriers via Coulomb interaction and is proportional to the product of piezoelectric and strain tensors. It has opposite sign for electrons and holes. Another source of polarization field is the LO phonon propagation in a polar medium. This polarization results from the relative shifts of the ions of opposite signs. This mechanism is called Fröhlich coupling and the strength of this interaction is described by dimensionless Fröhlich constant which is strongly increased in the case of nanostructures in comparison to bulk material. Both piezoelectric and Fröhlich couplings are associated with Coulomb interaction between carriers and phonon-related polarization.

Interactions with phonons are evidenced in the optical spectrum as sidebands in the case of LA phonons and phonon replicas for LO modes, accompanying the central emission line (so called zero phonon line - ZPL). All those spectral features are temperature and QD size (confinement regime) dependent.

First of all, the ZPL broadening (full width at half maximum - FWHM) shows linear and temperature activated increase with increasing temperature *T*, which can be described by the relation:

$$FWHM(T) = FWHM_0 + aT + \frac{b}{\exp(E/kT) - 1} \qquad (1.21)$$

where the first term is the width of the ZPL due to radiative decay (lifetime-limited due to Heisenberg uncertainty principle) and the third corresponds to phonon-assisted transitions, with *a*, *b* and *E* being parameters which can be extracted from the fit to experimental data [Bor05, Bay02-1]. The linear term is well known from structures of higher dimensionality and should appear if the transition is to the state separated by less than thermal energy *kT,* which

is a condition not easily realized in strongly confined QDs but possible in the case of QDashes. The linear term can be also interpreted as due to elastic interactions with phonons scattered on the etched surfaces if patterned samples are considered or interacting with charges in the environment [Ort04, Rud06, Fav07, Fer09]. The broadening of ZPL below 100 K can also result from pure dephasing, but this is a higher order effect.

At low temperatures excitons interact mainly with acoustic phonons, as they are the only ones available due to their energy, but cannot promote the exciton from the ground state to a higher state and thus those processes add to the pure dephasing. With increasing temperature the processes with occupation changes can appear, which is manifested as the acoustic phonon sidebands accompanying the ZPL in the optical spectrum. At low temperature those sidebands are asymmetric, as the processes with phonon absorption are less probable due to low occupation of phonon states, with one exception however, when the cut-off energy for exciton-phonon coupling is smaller or equal to the sidebands width. This is the case for large dots (small cut-off energy) for which all the phonon modes that contribute to the coupling are occupied already at low temperatures and the broadening of the sidebands does not change much with temperature. The phonon sidebands are narrower for larger QDs and additionally their contribution to the overall integral emission intensity is decreased in favour of ZPL. For strongly confined QDs the symmetry of the acoustic phonon sidebands is restored at elevated temperatures and the sideband width increases with temperature (due to increased phonon occupation), until the cut-off energy is reached. The ratio between the phonon sidebands and ZPL intensity changes with temperature in favour of phonon sidebands and can be described by the Huang-Rhys factor (the coupling strength), which can be extracted from the experiment from the relative contribution of ZPL and phonon sidebands to the emission. Based on the abovementioned considerations in the case of QDashes both the strength of the coupling with phonons and the cut-off energy should be greatly reduced due to a large size in the elongation direction and the resulting increased wave function extension. This would be very beneficial in view of applications. The main drawback seems to be the dense optical spectra of the QDashes resulting from their relatively large physical volume. The smaller the separation between the levels and the more levels confined within the nanostructure the stronger the dephasing (due to a large number of possible final states for the scattering process). Due to the enlarged size mainly in one direction, the maintenance of the strong confinement regime is possible even for relatively long nanostructures. Thus for

QDashes the advantage can be taken of the increased QDash volume without the reduction of the confinement strength.

In the case of LO phonons, phonon replicas (in first order approximation not broadened), separated by LO phonon frequencies, appear in the optical spectrum. As the coupling to LO phonons depends on local charge density (difference between electron and hole wave function), the replicas become narrower but their peak intensity increases for larger dots.

1.3. Current and potential applications

The application potential of QDashes is a result of the spectral range of their emission, high non-uniformity within the ensemble of nanostructures, high surface coverage, increased physical volume and finally high in-plane shape anisotropy. Due to the growth kinetics and decreased strain, the surface coverage is generally much higher as a result of both, the increased volume of a single dash as well as higher nanostructure density. It is one of the reasons of increased, in comparison to typical QDs, gain in QDash based devices. Also predictions considering the phonon-induced decoherence described in more details in the previous section work in favour of Qdash structures.

Emission range of typical GaAs-based nanostructures coincides with the maximum efficiency of silicon detectors. That is beneficial for some of the photonic devices as well as quantum protocols relying on a single photon detection due to high detection probability (low photon losses) and high signal to noise ratio, combined with low dark counts level. This results also in higher probability of success of the read-out process in quantum protocols or verification if the quantum state manipulation/initialization was successful and requires less repetition of the same procedure to gain adequate level of fidelity in statistical measurements. In the case of InAs/InP QDashes the emission is shifted into near infrared range up to 2 µm and covers broad range of telecommunication wavelengths from 1.2 up to 2 µm [Utz96, Guo97, Wan01, Sch02, Ukh02, Sau05, Rei07]. This extremely broad spectrum is highly desired for ultra-wide bandwidth optical amplifiers as well as short pulses generation. The change of the material system to InP-based was very important to reach 1.55 µm in view of minimizing the losses during long distance data transmission. The long wavelength limit for previously strongly explored InAs/GaAs QDs was 1.49 µm – the record value obtained due to additional pseudomorphic buffer layer [Ust98]. Recently 1.52 µm emission has been reported,

which was possible as a result of strain engineering and bilayer structure [Ru_03, Maj11]. Further increase in QD size to redshift the emission energy was not possible due to the increasing strain in the system, leading to material degradation. Additional advantage of InP-based nanostructures is easy spectral tuning via changing the amount of QDash material deposited in the growth process [Sau05], which results in designing devices with tailored spectral gain profile. QDash-based active region for optoelectronics combines all the advantages of QD-based one with distinct features of QDashes, i.e., low-threshold current, low-temperature sensitivity, high-quantum efficiency, small chirp, high modulation frequency, local carrier recombination, fast response time, small linewidth enhancement factor, spectrally inhomogeneously distributed gain [Rei07 and ref. therein] and emission wavelength tuneability. QDashes offer broader gain function, highly desired in some optoelectronic applications, e.g., tuneable lasers or optical amplifiers [Rei07]. Slight reduction of spectral gain due to the high inhomogeneity within the QDash ensemble is compensated by the high surface density of those nanoobjects. QDashes are very good examples of the possibility to control and engineer the output characteristics of a device by geometric parameters of the nanostructures. In that case the optical properties can be tailored to realize optimized gain bandwidth at telecommunication wavelengths for multi-wavelength optical amplification with no crosstalk, at data rates of 10 Gbit/s, pattern-free and with reduced noise level [Rei07 and ref. therein].

One of the specific features of QDashes is the ultra-wide gain, theoretical analysis of which [Der04, Wei05] revealed the possibility of spectral tuning without significant increase in the injected carrier density; much smaller (ten times) sensitivity of the refractive index to changes in the injected carrier density; so called large-signal chirp (important in evaluating modulation characteristics of the laser) as well as order of magnitude smaller chirp in comparison to higher dimensionality structures and comparable to the one observed in the case of self- assembled QDs. On the other hand, the differential gain even in highly optimized structures reaches only half the value of QWs and there is no improvement in linewidth enhancement factor. Further improvement of QDash-based lasers performance was obtained utilizing the effect of intermixing caused by post growth sample annealing [Dji08]. As a consequence a narrower linewidth due to improved dash homogeneity, lower threshold current densities and higher internal quantum efficiency were observed.

Another important characteristic than can be tuned in the broad range is the degree of polarization of emitted radiation of both surface and edge emission [Yu_99, Kit02, Fav05,

Rid07, Sai08, She08, Wan08, Hei08, And10, Roy10, Ike11, Usm11, Mus12]. The asymmetry of confining potential leading to increased light hole contribution to valence band states is governing the changes in polarization properties of emission [Kou04] and can be controlled via changing the shape anisotropy of QDashes. This enables to avoid external polarization optics to control the polarization state of the emitted radiation which strongly reduces the output power as well as compactness of the actual devices. The theoretical analysis of the polarization properties of emission from InGaAsP/InAs/InP QDashes and resulting gain characteristics can be found in [Hec09]. On the other hand, obtaining fully polarization independent gain in the case of QDashes is more challenging but can be realized in the edge emission in nanoobjects with enhanced size in the growth direction, so called columnar quantum dashes [Pod08]. Another possibility to equalize the intensity of perpendicularly polarized transitions is to enlarge the structure up to a point where the Coulomb interactions dominate over the confinement energy and the regime of the centre of mass wave function quantization is reached [And99].

Similarities to QDs ensure that single quantum dashes are promising candidates also for more sophisticated futuristic optoelectronic and photonic applications, i.e., micro- and nanolasers, non-classical light sources - single and indistinguishable photon sources as well as quantum bits for quantum computation and information processing and communication networks [Cha09, Yam09]. Practical implementation of all-optical coherent control of a single electron spin in SQD as a qubit by ultrafast pulses has been demonstrated [Pre08]. In principle, the proposed solution should work also for QDashes with the remark that the energy spectrum is denser and there are generally more states confined within the individual QDash in comparison to QDs, so the energy level of interest might be less isolated. One of the advantages of QDashes results from the increased physical volume of the nanostructures and, as a consequence, the increased coherence volume for light-matter interaction [Wim06, And99].

In the case of indistinguishable photon sources the figure of merit is the exciton fine structure splitting. It has been theoretically predicted that InAs/InP material system is much more suitable than InAs/GaAs for obtaining high level of indistinguishability as the bright excitonic transitions are much closer in energy [He_08]. However it is not straightforward to predict the value of the splitting for highly elongated nanostructures and this needs to be examined in details both experimentally and theoretically to evaluate their usefulness. What can be stated for sure is that InAs/InP nanostructures are promising candidates for micro- and

nanolasers as well as single photon sources for 1.55 μm but to practically utilize their potential both fundamental study and progress in InP-based microcavities design and growth has to be made.

2. Experimental

In this chapter the spectroscopic techniques (far field photoluminescence - PL, also in versions with increased spatial resolution and polarization-resolved) employed for the realization of the experimental part of the thesis are reviewed and the actual setup configurations are presented. The advantages and drawbacks of the used approach are pointed out and the physical basis of data interpretation is given. The second part of this chapter is devoted to the detailed description of the samples under investigation in view of growth and structure design. Two groups of nanostructures in different III-V material systems are considered: InGaAs elongated QDs on an GaAs substrate and InAs QDashes grown on InP. Available structural data concerning embedded QDs is cited and the differences between the samples within the series are stressed, as they are crucial for proper interpretation of the results of optical experiments.

2.1. Photoluminescence

Photoluminescence is a well-established experimental spectroscopic technique in which the excitation of the system is provided by the electromagnetic field and the PL signal is the radiation emitted, when the system releases this extra energy in a process of radiative recombination of electron-hole pairs and comes back to its thermal equilibrium. Different modes and excitation schemes are discussed in the following chapters and some variations of the standard method (increased resolution, polarization sensitive measurements) are described.

2.1.1. Fundamentals

The photoluminescence as a process of radiative emission of the excess energy in the solid state requires a non-equilibrium carrier distribution, which in this technique is created by the optical excitation. The fundamental process that constitutes the PL signal in semiconductor materials is the radiative recombination of an electron and a hole, in which a photon is emitted. There are three main excitation schemes that can be distinguished based on the relation between the energy of the exciting beam and the emitted photon (transition energy):

a) ***non-resonant excitation*** - one deals with this kind of excitation if the amount of energy supplied to the system highly exceeds the energy of emitted photon. In the case of bulk semiconductor the photogenerated carriers are excited to high energy states and at first they relax to the energy band minima and only then recombine radiatively. The energy of the emitted photon is close to the band gap of the semiconductor material. Carriers do not recombine radiatively immediately (in the excited state, where they are created) because the relaxation processes are much faster than the radiative recombination and due to the restriction of the wave vector conservation principle. This is one of the important limitations of all emission techniques that in most cases they are restricted to the fingerprints of the ground state (band minimum) and it is hard to probe the whole electronic structure of the material. This picture can be enriched by increasing the excitation power (increasing the number of photogenerated carriers), which can enable emission from excited states (so called hot luminescence of not fully thermalized carriers). In that case energy bands are occupied up to some level from which the radiative recombination process can take place. Photons emitted from excited states have energy larger than the band gap. In the case of low excitation power (when the average number of created excitons in the timescale of exciton lifetime is lower than 1) the energy of the emitted photon in the single particle picture is a sum of the band gap energy and the energy of the lowest electron state (level) and the first hole state (level), with respect to the corresponding band edges. Again the recombination process is preceded by the relaxation (although relaxation mechanisms can differ from the bulk case). This energy is generally decreased by the binding energy (Coulomb interaction energy) of the respective excitonic complex that is formed after carrier generation. When the excitation power is increased, the ground state emission saturates and the emission from higher states (levels) or the formation of more complicated excitonic complexes becomes possible. This is called feeding up the states or a state filling effect and is evidenced in the spectra by a blueshift of the emission band maximum or an appearance of higher-energy emission bands, depending on the inter-level spacing. In that case the PL can probe more than the ground state energy. In the multilayer structure with QDs in the non-resonant excitation scheme only some of the carriers are absorbed directly in the dot layer, but it is the minority, as the other layers have higher absorption due to much larger physical volume (absorption cross-section). However, carriers absorbed in other parts of the structure can be restored in the relaxation processes and still emit from the QD ground state, as the structures are designed in a way that this is the lowest state of the entire system.

b) ***quasi-resonant excitation*** - the energy of the exciting beam is close to the transition under study, but still a little higher. In that situation relaxation is required to reach the energy of the transition but usually it is realized in a single relaxation process (or very few ones). This is sometimes beneficial as the time delay between absorption and emission process can be easier predicted and does not differ a lot between subsequent absorption-emission processes of the same type - the dynamics of the system is much less complicated than in the case of non-resonant excitation scheme and the number of possible relaxation processes is limited. Also, the creation of charged exciton complexes is limited in that case, which simplifies the spectrum and allows for its easier interpretation. A good example of the realization of this excitation scheme in the case of structure with QDs can be the excitation energy coinciding with the states in the WL that can in some cases even partially overlap with the high-energy part of the QD ensemble absorption band, or the excitation into one of the QD excited states.
c) ***resonant excitation*** - the excitation energy is equal to the transition energy. In this scheme only carriers directly involved in the process under study are created and the absorption in the other part of the multilayer semiconductor structure is minimized, as the excitation energy is matched to the particular transition, which is most often lower than the band gap energy of adjacent layers. In that way the background radiation is strongly suppressed. Also some of the carriers are lost due to non-radiative processes but most of them recombine radiatively and add to the PL signal. The drawback of this approach is the abovementioned low absorption cross-section of a SQD. The most striking technical issue in the case of resonant excitation is filtering out the excitation beam as it has the same energy as the signal but in typical situation it is much stronger and can imprint some features (e.g., temporal/spatial/phase coherence) into the investigated system. One of the solutions is to take advantage of the isotropic character of spontaneous emission and guide the excitation and emission via different optical paths. A slight difference between the energy of absorbed and emitted photon can be also used, occurring due to distortions in the crystal lattice and following shift of the energy bands extrema caused by the presence of optical excitation changing the adiabatic potential for nuclear motion.

When the excitation conditions are further considered two excitation modes can be distinguished: continuous wave and pulsed excitation. In the continuous mode the energy is constantly supplied to the system and it reaches equilibrium, in which the average occupation of each state is constant. In this excitation mode and at high excitation conditions a local sample heating becomes an issue. On the contrary, in the case of pulsed excitation there are

generally much higher instantaneous powers (power in the pulse maximum) available but the sample is subjected to it for a very short period of time so the average power is much lower. This enables to create locally in a very short time a very high number of carriers and real-time observation of how their distribution evolves (time-resolved PL).

Another important external parameter that influences the PL signal is the temperature of the sample. In the system with a given number of excitons at 0 K only the lowest states (levels) are occupied. As the temperature is increased, the occupation distribution changes in favour of higher energy states (levels). In QDs the process is not continuous as the energy spectrum is discrete but adding the thermal energy to the system increases the probability of occupation of higher energy states. If the thermal energy kT is comparable with the energy state separation it leads to the depletion of the ground state. In the case of a highly inhomogeneous QD ensemble, slight increase in the temperature in the low temperature range results in the redistribution of carriers within the ensemble (between dots of different sizes). At low temperatures a carrier is trapped by one of the nearest dots due to the insufficient thermal energy for escape. The energy of the carrier localized in this dot is not necessarily the lowest possible. When the additional thermal energy is supplied, the carrier can be released and minimize its energy, reaching the dot with lower ground state energy. This is observed in the experiments as a redshift of the QD ensemble emission band and a lower broadening of the emission peak. When the temperature is further increased the excitons can dissociate (in the case of QDs this means releasing at least one of the carriers from the dot), but again, this is a gradual process in which the probability of observation of the excitonic emission decreases. The decay of the exciton can have multiple causes, depending on the details of the physical system under investigation, i.e., dissociation when the thermal energy exceeds the exciton binding energy (this is the reason of instability and difficulties with observation of excitons in bulk but is partially overcome in the case of lower dimensional structures due to spatial confinement), promotion of one of the carriers to a higher state, escape of one of the carriers (or both) to adjacent layers, e.g. WL, barrier, substrate etc.

Measurement of the intensity decay of the PL signal as a function of the temperature (photoluminescence quenching) provides the information about the temperature dependence of the energy gap, possible energy/excitation transfer within the structure and energy scale of the emission quenching mechanism(s). The first figure of merit to be analysed is the energy position of the maximum of the PL signal. In the case of bulk semiconductor it reflects the temperature dependence of the band gap energy, which decreases with temperature due to the

thermal lattice expansion and electron-phonon coupling. Some empirical or semi-empirical models to describe this relation more quantitatively have been developed. In the approach proposed by Varshni [Var67] the band gap energy dependence on temperature is described in the following way:

$$E_g(T) = E_g(0) + \frac{AT^2}{T+B} \qquad (2.1),$$

where the first term is just the value of the band gap energy at the temperature T = 0 K and *A* and *B* are parameters characteristic to the given material, all three being the fitting parameter when confronting with the experimental results. This formula works well for most of the III-V and II-VI materials. It accounts for the low temperature behaviour of the band gap energy (asymptotic quadratic dependence) but some deviations become apparent at higher temperatures.

The second most often used model is the Bose-Einstein model [Lau86], taking into account the electron-lattice interaction:

$$E_g(T) = E_g(0) - \frac{2a_B}{\exp\left(\frac{\Theta_E}{T}\right) - 1} \qquad (2.2),$$

where a_B describes the strength of the electron-phonon coupling and Θ_E stands for Einstein characteristic temperature defined as an average temperature of phonons interacting with the electronic subsystem. Bose-Einstein formula is more general and so more reliable in a wide temperature range and as the Einstein temperature can be estimated for most semiconductors it has only one fitting parameter.

Presence of additional localization centres within the system influences the temperature dependence of emission energy. The carriers can be trapped at low temperature and the increase in the temperature is crucial to releasing them so they can occupy the global energy minimum. This is evidenced in the PL spectra as a local minimum of the emission energy as a function of temperature in the low temperature range, the so called 'S - shape' [Cho98]. Similar behaviour will be observed in the case of carrier redistribution within the QD ensemble. Generally, the emission from the ground state is quenched when the temperature is increased due to the carrier redistribution in favour of higher energy states and carrier losses (in the case of low dimensional structures due to thermally-activated escape from the confining potential). This behaviour can be described by the following formula:

$$I(T) = \frac{I_0}{1 + \sum_{i=1}^{N} C_i \exp\left(-\frac{E_i}{kT}\right)} \qquad (2.3),$$

where: I denotes the intensity of the PL, I_0 corresponds to the 0 K limit of the PL intensity (its maximum value). Each component under the sum is related to one quenching mechanism with characteristic activation energy E_i and efficiency C_i. Fitting the Arrhenius plot (logarithm of PL intensity as a function of inversed temperature) with this dependence enables to obtain characteristic activation energies and relative importance of PL decay mechanisms. Further comparison with theoretical calculations helps to identify the respective quenching mechanisms based on the determined specific energy scales. Furthermore, the temperature-induced energy transfer can appear in some systems and can drastically change this picture as it superimposes the relative changes of the emission from different parts of the structure on the thermal PL quenching. As far as the PL from a QD ensemble is considered, the PL signal intensity is constant at low temperatures even though carrier redistribution within the ensemble can be activated via the thermal energy. This is due to the fact that when the carrier migrates within the ensemble it is not lost in view of the emission of the QD ensemble - the integral PL intensity is constant but the emission band can have a little different shape due to the altered contribution of the emission from different dots. The PL intensity starts decreasing significantly only when the thermal energy becomes comparable to the energy necessary for escape of one type of the carriers from the confining potential of QDs or non-radiative processes start to play a role. In the system with additional localization, the ground state emission intensity has a maximum as a function of temperature as it is fed by the carriers released from the trapping centres thanks to the thermal energy.

Another observable of temperature-dependent measurements is the broadening of the emission, e.g., its full width at half maximum. The emission band broadens with the temperature because of the enhanced excited state emission due to the thermally changed carrier distribution and increased decoherence (mainly phonon-induced). The latter is well evidenced in the single exciton emission (the detailed discussion of the width and lineshape changes as a result of exciton dephasing is included in Section 1.2.4).

2.1.2. Experimental configuration

In order to obtain results presented in the main part of the thesis, there has been used the standard far field photoluminescence setup (Figure 2-1).

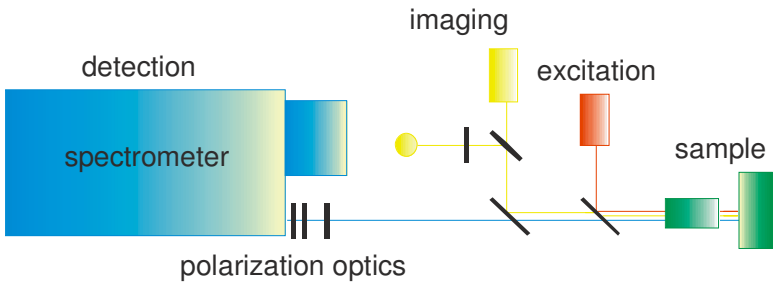

Figure 2-1. Scheme of the PL experimental setup. Optical paths of different functional blocks are marked with different colours and shifted horizontally for clarity: excitation (red), imaging (yellow) and detection (blue).

In that configuration the sample is mounted in the liquid-helium continuous-flow cryostat which enables the temperature-dependent measurements from 4.5 K up to room temperature, with a resolution and stability in the range of a fraction of the degree thanks to the feedback loop system between the heater and a set of temperature sensors. The change of the position on the sample surface is realized by the motion of the whole cryostat. The excitation is typically provided by a single-mode semiconductor laser working in a continuous wave mode at 660 nm, which is non-resonant for all the investigated structures (well above the band gap energy of the substrate). The excitation power can be varied in the range from single nW up to 60 mW with neutral and variable density filters. The laser beam is introduced into the main optical axis via the spectrally selective optical element - cold mirror - which reflects the visible light (excitation) and effectively transmits the infrared radiation (signal). This has additional advantage of axial (perpendicular to the sample surface) excitation, which enables the use of the same optics to focus the excitation on the sample surface and to collect the emitted signal. Thus it is easier to ensure that the detection takes place from exactly the same place on the sample surface that is excited, without additional optical elements. Moreover, the cold mirror filters out the laser beam reflected from the sample surface from the main optical axis (and so the detection system), decreasing the background radiation. Despite that an additional longpass filter, with the cut-on wavelength of 700 nm, was mounted on the entrance of the monochromator. The excitation beam is focused on the sample surface to the spot of about 0.1 mm in diameter. The signal is then focused on the entrance slit and further

dispersed by the 0.55 m single grating monochromator. There are available three possible gratings, with different number of grooves per mm and blazes within the infrared range. The detection is provided either by the InGaAs multichannel linear array detector with detection window up to 1.6 μm or a single channel InGaAs photodiode with lower sensitivity but the spectral range extended to 2.4 μm. The detection system based on the photodiode is realized with a homodyne nanovoltmetre (lock-in amplifier) with modulation of excitation beam provided by a mechanical modulator (276 Hz).

2.1.3. Single quantum dot spectroscopy

To investigate properties of single nanoobjects (observe emission from a single exciton state) the spectral and spatial resolution of the PL setup has to be greatly enhanced, as the radiative lifetime-limited width of a single emission line and the exciton fine structure splitting are in the single μeV range.

A very successful approach enabling optical measurements with SQD resolution is the near field spectroscopy. In this technique the free space light propagation is replaced by the fibre optics and the excitation is provided via the near field interactions between the evanescent radiation and the dot (distanced from the source below the wavelength of the excitation light). In that scheme the spatial resolution is not diffraction-limited (restricted by the wavelength of the exciting light) but determined by the size of the aperture and the distance to the sample surface, as the excitation beam is confined to an area on the order of the size of the aperture. This results in a tens of nanometres scale resolution, enabling the excitation of individual nanoobjects on the sample surface. However, this technique has also its limitations, with the most problematic ones being a very short working distance and extremely shallow depth of field. The first one makes it challenging to conduct experiments at low temperatures, when the sample has to be mounted in the cryostat (and so the fiber transmitting excitation beam) and the latter restricts the region of interest to the tens of nanometers below the sample surface at most. The experimental setup is rather sophisticated and requires a very good mechanical and thermal stability to destroy neither the sample surface nor the fibre tip.

As an alternative, the conventional far field spectroscopy can be adapted to perform experiments in the SQD regime. There are many ways to improve this standard approach, which has unprecedented advantages of simplicity and non-destructivity. First of all, the

selection of proper optical elements plays an important role. The spatial resolution can be enhanced up to a single micrometer range (or even below) by replacing the standard focusing lens with microscope objective, with the bottom limit only due to diffraction, determined by the wavelength of applied excitation and dependent on the numerical aperture of the employed optics. Diffraction-limited size of the excitation spot is the reason why in the case of self assembled QDs with typical surface density of $10^{10}/cm^2$ it is not possible to ensure the excitation of only one nanoobject but always at least about 100 of them. That makes the emission spectrum more complex, as it is composed of optical response of many emitters, however sometimes still distinguishable spectrally due their emission energy dispersion. Additionally, choosing the spectral range near the edge of the ensemble distribution decreases the probability of having two QDs with ground state energy overlapping within the spectral resolution of the setup. To further improve the resolution of the experimental setup and signal intensity the so called immersion lenses can be used. Those are made of materials with high refractive index and when positioned exactly on the sample surface (i.e. placed between the sample and the objective lens) they increase the light collection from the sample by increasing effectively the numerical aperture of the optics as it depends on the refractive index of the medium the light is transmitted through [Moe03, Liu05]. Another way to improve the signal quality and the selectiveness is to apply the spatial filtering with confocal configuration. In that scheme the light is guided through a pinhole which reduces the background level by eliminating the out-of focal plane radiation and enables to investigate the signal coming from different parts of the structure in depth (in the growth direction in the case of the surface emission). Eventually, to limit the number of excited QDs the sample surface can be patterned by a post-growth processing. This can be realized by electron beam lithography combined with the reactive ion etching to fabricate submicrometer objects on the sample surface (mesas). As the QD layer is etched-off everywhere except for the mesa region, the number of excited QDs is determined by the QD surface density and the mesa size. It is no longer defined by the excitation spot size further enlarged due to the carrier diffusion. Additional advantage of this approach is the possibility of repeating the measurements on the same QD, which is impossible in the case of unpatterned sample. Alternatively, a metallic mask can be deposited on the sample surface with hundred nanometer-sized apertures but in that case filtering the reflected and scattered excitation radiation is indispensable. However, the abovementioned procedures cannot be usually scaled down to a mesa/aperture size containing only one QD, because if the mesa/aperture becomes smaller, the surface effects and

imperfections of the mesa sidewalls (e.g., roughness, carrier trapping centres, fluctuating electric field) become significant. They can strongly influence the QD emission, which is highly undesired.

The actual experimental setup used for SQD investigations is the far field microPL setup described in the previous section equipped with an infinity-corrected microscope objective with high numerical aperture (0.4) and long working distance (20 mm) allowing for the low-temperature measurement in the liquid-helium continuous-flow microcryostat, using an InGaAs linear array detector.

2.1.4. Polarization-resolved measurements

To investigate the polarization properties of emission the polarization characteristics of the experimental setup itself and the background radiation have to be taken into account. It is also important to ensure that the orientation of the sample (and so crystallographic directions) and/or the elongation direction of the QD structures is known and well-defined with respect to the optical axis of the experimental setup in order to interpret the results of polarization-resolved measurements correctly.

One of the possible ways to describe the polarization state of light is the Stokes vector formalism which can describe any possible polarization state, even if the light is polarized only partially. There are four coordinates constituting the Stokes vector (also called Stokes parameters). The first component - S_0 - is equal to the overall radiation intensity. The rest of them - S_1, S_2, S_3 - describe the supremacy of the respective polarization contributions: horizontal over vertical, diagonal over anti-diagonal (horizontal and vertical in a 45 degree rotated basis) and right-handed over left-handed one. To obtain those values quantitatively the formula below needs to be applied for each coordinate separately:

$$S_i = \frac{I_x - I_y}{I_x + I_y} \qquad (2.4)$$

where I_x and I_y are intensities of light polarized horizontally and vertically in the case of the S_1 coordinate and analogically for the others. Most often the Stokes vector is normalized by the total emission intensity and so its first coordinate equals 1. In that case the contributions of different polarization states are calculated as follows:

$$P = \sqrt{S_1^2 + S_2^2 + S_3^2} \qquad (2.5)$$

for polarized light P,

$$N = 1 - P \qquad (2.6)$$

for unpolarized light N,

$$P_{linear} = \sqrt{S_1^2 + S_2^2} \qquad (2.7)$$

for linearly polarized light P_{linear}. The contribution of circularly polarized light is simply equal to S_3.

The most accurate method to experimentally determine the polarization state of light is just to measure the intensities of overall emission and respective linear and circular polarization contributions and use them to determine the coordinates of the Stokes vector. One has to keep in mind that the polarization state of light can change during reflections and/or transmission through optical elements (due to antireflection coatings or multilayer design) as the amplitude coefficients of reflection/transmission can differ for s- and p-polarized light and the phase relation between the components of the electric vector can be altered. To avoid such effects the setup configuration has to be arranged in a way that the signal is guided through the polarization insensitive elements or such that their polarization characteristics are well specified and can be taken into account in data analysis. The element that is always polarization sensitive is the monochromator grating as the efficiencies for s- and p-polarized light differ and are spectrally dependent. One solution is to measure the polarization characteristic of the whole experimental setup, including the monochromator and to determine a calibration curve that will be used to post-process the experimental results. The advantage of this approach is that the characteristic of the whole experimental setup can be included simultaneously. On the other hand it cannot account for light phase changes and will not work properly in the case of complicated and completely unknown polarization state of light. It is also not sufficient if there is a significant and/or varying background contribution. Such a polarization calibration curve was successfully utilized in the polarization-resolved measurements on the nanostructure ensembles presented in Section 3.1.3 and 4.2.2. The disadvantage of this method is its non-universality and approximate character. Additionally, it is not suitable for very low signals since the grating efficiencies can differ strongly and as a result, the intensity of one of the polarizations will be much weaker (below the detection sensitivity). One can overcome this difficulty by ensuring that light entering the monochromator will always have the same linear polarization, which can be realized by placing the linear polarizer in front of the monochromator. This will always be in the same position, corresponding to the linear polarization direction for which the grating efficiency is

higher. In that way two issues are addressed simultaneously - intensity of the emission signal and the polarization sensitivity of gratings. The next step is to transform the polarization state that one wants to measure into the linear polarization that can be transmitted through the fixed linear polarizer - for linear polarizations of different orientations a half wave plate is used to rotate the polarization axis and then the quarter wave plate converts the circular polarization into the linear one. Again, for QDs with well assigned optical axis and two linearly polarized components expected, it is sufficient in a first approximation to determine only the contribution of different linear polarization components to the emission by rotating the half wave plate in front of the fixed linear polarizer. The light of different than linear polarization state constitutes a constant background that can be simply subtracted. This approach is further utilized to determine the polarization properties of emission from SQDs as it outperforms the previously described method, when the intensity of different linear polarization components for very low signals is considered.

In the case of an unknown polarization state of light, intensities of six different polarization components entering formulas for Stokes parameters need to be measured. This enables to fully characterize the polarization state but introduces one technical issue. The elements on the optical axis have to be exchanged between different measurements and so can alter the overall emission intensity (different transmission of half and quarter wave plate, repeatability of their positioning, slight change of the optical path) from one measurement to another, lowering the accuracy of the outcome of the experiment.

Results presented below were obtained using the nanoparticle film (ensuring no distortion in a beam path) linear polarizer with extinction ratio exceeding 100 000:1 and the average transmission of 85 % in the spectral region of interest, combined with an achromatic half wave plate. Their performance was confronted with a liquid crystal variable retarder and an achromatic depolarizer. The first one is not very convenient to operate in a broad spectral range as the retardance dependence on the input voltage is rather flat. The retardance is also averaged over time as it is altered with a frequency limited by the nematic particles orientation dynamics and the latter design imposes an oscillatory pattern on the intensity of transmitted radiation, which cannot be neglected in the case of the single quantum dot signal. To exclude the influence of the polarization of the excitation beam on the emission of investigated nanostructures the photoelastic modulator has been used to depolarize the laser radiation (nominally linearly polarized), despite its minor role in the case of the non-resonant excitation.

2.2. Investigated structures

In this chapter the detailed description of structural data and basic properties of investigated structures is presented. All the structures contain epitaxial nanoobjects formed spontaneously due to self-organization in Stranski-Krastanow growth mode. The thesis contains detailed analysis of two groups of application relevant nanostructures in view of both ensemble and SQD properties. First group is constituted by GaAs-based large and elongated QDs designed for emission at silicon detection maximum, whereas the second group takes advantage of the InP substrate to shift the emission further towards the infrared range. For both groups the full in-plane rotational symmetry is not preserved and the physical volume is much larger than for standard strongly confined and strongly strained QDs. They differ significantly in geometry (mostly LAR) as well as in the details of the confining potential, which results in substantial differences in their optical properties.

2.2.1. InGaAs/GaAs elongated quantum dots

The first group of investigated structures is GaAs-based. The substrate is undoped and (001) oriented. The subsequent layer arrangement is as follows: 300 nm GaAs buffer, alternating AlAs/GaAs superlattice stopping layer preventing the propagation of defects from the substrate, an InGaAs active region and a 50 nm GaAs cap (Figure 2-2).

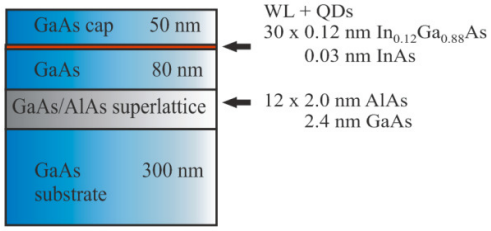

Figure 2-2. Scheme of layer arrangement for 30 % indium InGaAs/GaAs QD structure.

The active region for all the samples is a low indium content InGaAs layer of 4.5 nm thickness (estimated from the growth calibration) grown by submonolayer deposition. Low In content is the underlying reason of reduced strain, in comparison to InAs/GaAs material combination [Löf06]. The nominal indium content varies from 27% up to 36% and determines the active region dimensionality and morphology (Figure 2-3).

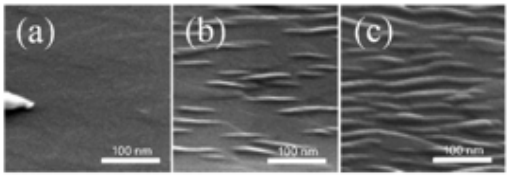

Figure 2-3. Surface SEM images of uncapped InGaAs/GaAs structures for various In content equal (a) 27%, (b) 30% and (c) 33% [Pol06].

For the lowest In content the growth is pseudomorphic and a thin InGaAs QW is formed. The surface roughness visible in the Scanning Electron Microscopy (SEM) image corresponds to the QW thickness and/or composition fluctuations on a monolayer scale. The two dimensional growth proves that the critical thickness for three dimensional island formation has not been reached. This parameter strongly depends on the strain resulting from the lattice mismatch between the active region and the underlying substrate. Lattice mismatch is in that case changed by the In content. The thickness of this layer estimated from optical experiments is approx. 3 nm, slightly below the one predicted from growth conditions, probably mainly due to MBE apparatus calibration procedure overestimating this parameter. This thin InGaAs QW can be treated as a reference for further QD investigations to learn about the accompanying WL as its essential properties should be the same in the full structure with QDs. Indium content increase to only 30 % is sufficient to assure conditions for three dimensional quantum island formation for a given amount of InGaAs deposited material. This is mainly due to the increased strain for higher In content InGaAs layer, resulting in a decreased critical thickness of pseudomorphic growth. In that case large $In_{0.3}Ga_{0.7}As$ QDs are created on top of the 2.7 nm thin WL [Pol06, Löf06]. The increased physical volume and typical geometry of those nanostructures (20 x 50 x 3 nm^3) can be traced back to low strain growth conditions enabling enhanced accumulation of the deposited material. Another consequence is that the growth kinetics is more sensitive to inherent substrate anisotropies (in our case surface diffusion coefficients), leading to in-plane shape asymmetry, i.e., QD elongation in the [1-10] direction. The abovementioned factors result in large nanostructures (for which weakened confinement regime is expected) of low surface density of approx. 5 x 10^9 /cm^2, beneficial for single dot spectroscopy in far field microPL approach. Low surface density of QDs is a result of fixed upper limit of deposited InGaAs material, which is divided between WL and QDs. The properties of the WL in this structure were independently verified in the Atomic Probe Tomography (APT) experiment. Estimated thickness of 3.2 nm and 29 % In content are in agreement with expectations based on growth conditions [Löf06] and previous optical study [Pol06]. In Figure 2-4 atom concentration depth profile obtained by APT measurements is

presented. The In content in the active region is on the level of 14.5 % of all atoms. This is equivalent to 29 % of metallic atoms (Ga + In), which is typically referred to as the indium content. Due to the low nanostructure surface density there are no QDs in the probed area (approx. 60 nm in diameter).

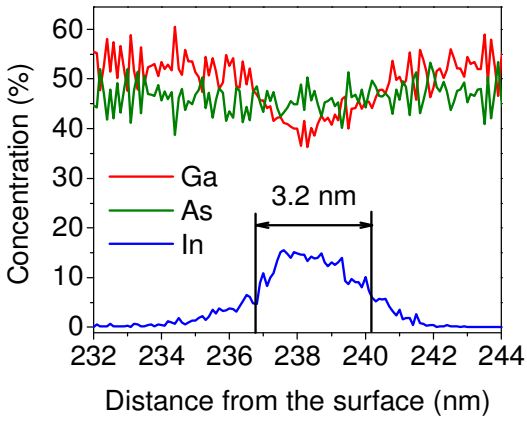

Figure 2-4. Depth profile of atom concentration in 30% InGaAs/GaAs structure.

This sample is considered to be the most interesting from the whole series in view of applications and fundamental study due to its low surface density combined with large nanostructures volume, resulting in the increased oscillator strength of optical transition. It is very promising to test fundamental electrodynamics effects in conditions much different than for standard small strongly confined QDs, i.e., weakened and shallow confinement regime as well as broken in-plane rotational symmetry in both weak and strong light-matter coupling regimes [Rei04, Rei09].

Further increase in the indium content leads to slight increase in QD size limited by the increased strain and higher QD surface density reaching 10^{10} /cm^2 typical for self-assembled QDs. This is caused by the increase in relative amount of material spent for QD formation as a result of diminished critical thickness. Emission energy is in that case a result of a trade-off between the energy gap change due to different InGaAs alloy composition and the size-related quantum effects.

For single quantum dot spectroscopy part of each of QD samples has been patterned.

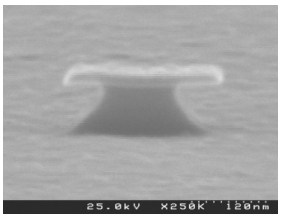

Figure 2-5. Top view SEM image of QD structure with 240 x 240 nm^2 mesa etched on the sample surface.

At first the designed pattern was imposed on the sample surface via electron beam litography and then etched, leaving squared areas with full structure containing QDs - mesas (Figure 2-5), surrounded by pure GaAs (Figure 2-6).

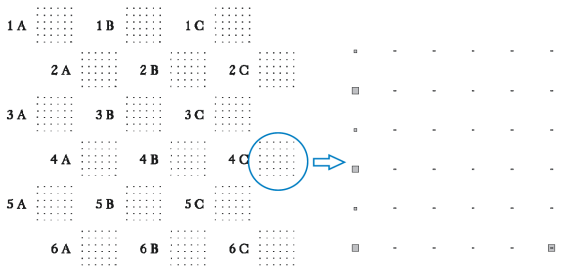

Figure 2-6. Scheme of the sample surface patterning with one of the fields enlarged.

The size of the mesas are in the range of 1 µm down to 100 nm (Table 2-1), which combined with the low surface density of the investigated nanostructures opens up the possibility of finding a mesa with only one QD and typically with a few of them for small enough mesa sizes. The distance between neighbouring mesas is 30 µm to ensure that only one mesa is excited at a time. At each row there are three matrices (A, B, C) with mesas of the same size marked by numbers (Table 2-1). There is always one column of reference mesa structures of 2 and 5 µm size. They act as markers for rows of submicrometer mesas not visible on the sample surface image.

Large $In_{0.3}Ga_{0.7}As$/GaAs QDs are the subject of the third chapter where all optical measurements are reported and discussed.

Table 2-1. Mesa sizes for InGaAs/GaAs QD structures.

Row	36% In	30% In	33% In
1	2000nm	2000nm	2000nm
2	1750nm	1750nm	1750nm
3	1500nm	1500nm	1500nm
4	1250nm	1250nm	1250nm
5	1000nm	1000nm	1000nm
6	900nm	900nm	900nm
7	800nm	800nm	800nm
8	700nm	700nm	700nm
9	600nm	600nm	600nm
10	500nm	500nm	500nm
11	400nm	400nm	400nm
12	300nm	300nm	300nm
13	290nm	290nm	290nm
14	280nm	280nm	280nm
15	270nm	270nm	270nm
16	260nm	260nm	260nm
17	250nm	250nm	250nm
18	240nm	240nm	240nm
19	230nm	230nm	230nm
20	220nm	220nm	220nm
21	210nm	210nm	210nm
22	200nm	200nm	200nm
23	190nm	190nm	190nm
24	180nm	180nm	180nm
25	170nm	170nm	170nm
26	160nm	160nm	160nm
27	150nm	150nm	150nm
28	140nm	140nm	140nm
29	130nm	130nm	130nm
30	120nm	120nm	120nm
31	110nm	110nm	110nm
32	100nm	100nm	100nm
33	90nm	90nm	90nm
34	80nm	80nm	80nm

2.2.2. InAs/InP quantum dashes

The second nanostructures of interest are InP-based QDashes. They have been designed for second and third telecommunication window (1.3 and 1.55 μm) emission as such strong redshift of the emission with GaAs-substrate is rather challenging [Ust98, Ru_03, Maj11] and usually accompanied by deterioration of the structure optical quality. The InAs/InP material system is also not strongly strained (3.4 % lattice mismatch) but differs significantly in the growth kinetics which is much more complicated and resulting nanostructure shape/size is very sensitive to the details of the growth conditions. The investigated structures represent QDashes strongly elongated in [1-10] direction (with LAR typically exceeding 5). The series consists of three samples differing in the amount of InAs deposited during growth, which layer thickness equals 0.7 nm, 1.05 nm and 1.3 nm,

respectively. They are all grown on (001) InP substrate and 200 nm $In_{0.53}Ga_{0.23}Al_{0.24}As$ buffer layer. The same quaternary barrier is placed on top of the InAs active layer, followed by a 10 nm InP cap (Figure 2-7).

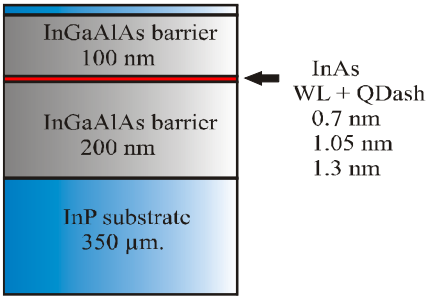

Figure 2-7. Scheme of layer arrangement of InAs/InGaAlAs/InP QDash structures.

It has been shown that the amount of InAs deposited during the growth of the QDash layer changes mainly the cross-sectional dimensions, preserving the triangular geometry [Sau05] which determines the emission energy. Utilizing the InAs layer thickness as a tuning parameter structures for a demanded spectral range can be easily designed [Sau05, Rei07], covering the broad range from 1 up to 2 µm. The structure with 1.05 nm InAs has been designed for 1.55 µm emission at room temperature. The typical geometry is in that case approx. 16 x 3 nm^2 in cross-section (after ref. Sau05) and more than 100 nm in the elongation direction. The surface density of those nanostructures is very high - up to 10^{11} /cm^2, which together with a large physical volume of a single nanostructure assures surface coverage above 50% and so increases greatly the direct absorption in comparison to small QDs of lower density. This results in increased gain and has been utilized in development of lasers and optical amplifiers [Rei07].

The emission energy could make these InAs/InP QDashes also very promising candidates for single photon sources at 1.55 µm, e.g., for data transmission in quantum telecommunication networks. Their potential in view of SQD properties and applications has not been systematically and comprehensively tested so far and is partially covered by this thesis. Another advantageous property of the investigated structures is their strong in-plane asymmetry expected to lead to polarization properties that might enable selective coupling to single microcavity mode and so obtaining fully polarized emission due to inherent properties of the active region, without post emission selection or modification of the signal.

As previously indicated, the InAs amount influences mostly the cross sectional size, which for 0.7 nm and 1.3 nm InAs can be estimated to be 12 x 2.5 nm^2 and 20 x 3.5 nm^2, [Sau05] resulting in emission at around 1.3 and 1.6 µm, respectively. For all the samples the length of the dash is much bigger than the size in the two remaining dimensions. The quantum dash surface density is only slightly altered, showing an increase with increasing amount of the deposited QDash material (Figure 2-8).

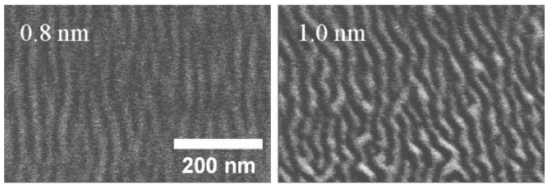

Figure 2-8. Top view SEM images of QDash structures with various nominal amounts of InAs material [Rud06-1].

To enhance the spatial resolution and limit the number of simultaneously excited QDashes the sample surface has been patterned via the combination of electron beam litography and reactive ion etching. There are fields with different mesa sizes marked by numbers (Table 2-2). The details of the patterning are the same as in the case of InGaAs/GaAs QDs presented in Figure 2-6. Mesas have rectangular shape (Figure 2-9) and sizes in the range of 2.2 x 1.1 $µm^2$ down to 550 x 275 nm^2 (Table 2-2), which limits the number of excited nanostructures down to a few tens (about 20), which can be further spectrally separated due to the self-assembled growth resulting in pronounced size dispersion within the QD ensemble, reflected in the ground state energy dispersion.

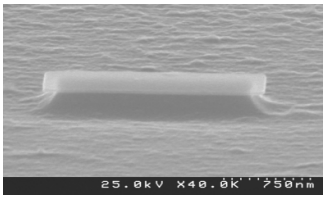

Figure 2-9. Top view SEM image of QDash structure with 2.2 x 1.1 $µm^2$ mesa etched on the sample surface.

Results of optical study on this series of InAs/InGaAlAs/InP QDashes are presented in Chapter 4.

Table 2-2. Field designation with corresponding mesa sizes for InAs/InGaAlAs/InP QDash structures.

Field	Length	Width
1	2200	1100
2	2100	1050
3	2000	1000
4	1950	975
5	1900	950
6	1850	925
7	1800	900
8	1750	875
9	1700	850
10	1650	825
11	1600	800
12	1550	775
13	1500	750
14	1450	725
15	1400	700
16	1350	675
17	1300	650
18	1250	625
19	1200	600
20	1150	575
21	1100	550
22	1050	525
23	1000	500
24	950	475
25	900	450
26	850	425
27	800	400
28	750	375
29	700	350
30	650	325
31	600	300
32	550	275

3. Optical properties of InGaAs/GaAs elongated quantum dots

The optical properties of the series of InGaAs/GaAs structures differing in the In content and as a result in QD size/density have been investigated by means of photoluminescence both on the ensemble and in the SQD regime. In the first part of this chapter study on the emission of the whole QD ensemble is summarized. The main photoluminescence quenching mechanisms are identified and the polarization-resolved PL is utilized to probe the anisotropy of the exciton probability density distribution as well as the underlying confining potential. In the following part the character of emission on the SQD level is analysed and the issues of the biexciton binding energy, fine structure splitting of exciton states and the exciton decoherence mechanisms are addressed. The comparison between the results obtained on the whole ensemble of QDs and on single QDs can help determine which effects have random character and average out when optical response of many objects is considered and to what extent they can differ from one dot to another.

3.1. Electronic structure

To interpret PL quenching measurements properly and to identify the main carrier loss mechanism for QDs under investigation, the electronic structure of the whole system, not only QDs ground state, needs to be determined. To achieve this goal photoreflectance spectroscopy (PR) has previously been employed [Pol06]. This is a very useful absorption-like experimental technique which enables to determine the energy of the higher energy states. The undoubted advantage of this technique is the possibility of performing the measurements at room temperature without losing much of the details of the optical response or the signal to noise ratio. The PR measurements were previously used to extract the properties of the WL accompanying InGaAs/GaAs QDs fabricated in the Stranski-Krastanow growth mode [Pol06]. Two resonances were clearly distinguished in these absorption-like spectra and identified as the light and heavy hole related transitions. The experimental values of the transition energies compared with the calculations of energy levels in a square-like potential well model, in the effective mass approximation using envelope function approach, confirmed this interpretation and enabled to determine the width of the WL in each structure, which is summarized in Table 3-1 after [Pol06].

Table 3-1. WL thickness determined from PR spectra for InGaAs/GaAs QD structures with various In contents expressed in nanometers and monolayers (ML) [Pol06]

In content (%)	WL thickness (nm)	WL thickness (ML)
27	3.0	10.0
30	2.7	9.0
33	2.3	7.7
36	2.2	7.3

As expected, with increasing In content the critical thickness for the three dimensional QD formation is decreased and so the WL quantum well becomes narrower. This is a strain-induced process as the lattice mismatch between the substrate and the InGaAs layer is larger for smaller In content. Further calculations revealed that the fundamental transitions of heavy and like hole character are the only ones possible in such a thin QW. The emission energy of the WL in structures with different indium content is a result of the trade-off between changes in a band gap energy (driven by both the composition and the strain) and ground state confined level energy (driven by the QW thickness and strain). The band gap energy is getting lower with the increasing In content, whereas the ground state energy of the level in the well, on the other hand, increases with decreasing QW thickness (decreasing critical thickness) for larger In contents. These two effects compensate each other partly, making the total shifts of the transition energies with the change of the compound compositon rather small. The respective energies of light and heavy hole related transitions determined from PR measurements are summed up in
Table 3-2 after [Pol06].

Table 3-2. Energy of heavy and light hole transitions in WL determined from PR spectra of InGaAs/GaAs QD structures for various In content [Pol06].

In content (%)	heavy hole transition energy (eV)	light hole transition energy (eV)
27	1.352	1.430
30	1.350	1.425
33	1.350	1.425
36	1.325	1.400

For 30 % indium content the transition energy is redshifted, which means that it is mainly governed by the band gap energy change. The light hole transition is much less altered due to lower sensitivity of the weakly localized levels to the changes of the confining potential band edge. In the case of 33 % the transition energies are almost identical, suggesting that both effects compensate each other. Further increase in the In content results in the lower transition energy, proving a dominant role of the band gap energy. The influence of QW thickness is smaller, even though for such a thin QW the exact energy level positions should be rather sensitive to the exact size in the growth direction.

This affects strongly the QDs whose growth follows the WL formation, as the total amount of InAs material used in each growth process is the same. As a result, when the WL becomes thinner, the amount of material available for QDs formation (i.e. not spent for the growth of the WL) is increasing and finally both QD size and the nanostructures surface density is altered. The general tendency is apparent from the SEM images of the reference quantum dot layer on the sample surface (Figure 3-1). The density of the dots is increasing with the In content and also the QDs are getting slightly bigger, without much alteration of their in-plane geometry. The indium content in the QDs also differs and these changes do not have to follow the relation between the nominal compositions exactly.

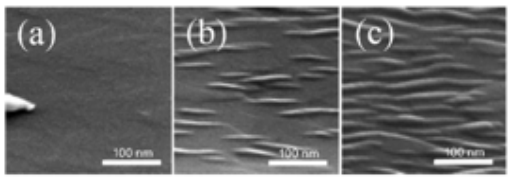

Figure 3-1. Surface SEM images of uncapped InGaAs/GaAs structures for various In content equal (a) 27%, (b) 30% and (c) 33% [Pol06].

The correlation between these observations and the optical response of the QD ensemble is the topic of the next section.

3.1.1. Emission from quantum dot ensemble

To complete the preliminary characterization of the InGaAs/GaAs structures high excitation photoluminescence experiment was performed. PL spectra normalized to the maximal emission intensity are presented in Figure 3-2.

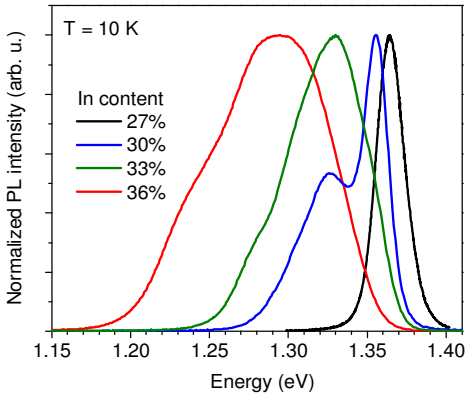

Figure 3-2. High excitation PL spectra of InGaAs/GaAs QD structures with various In content measured at 10 K.

For the lowest indium content SEM image indicates that the critical thickness for the QD formation has not been exceeded and as a result the active region is constituted by a thin InGaAs QW. At 5 K the ground state emission wavelength equals 1.364 eV (909 nm) and based on the previous PR study [Pol06] can be attributed to the fundamental heavy hole-like transition. No other spectral features can be resolved due to high density of the 2D continuum of states in the WL, which prevents the emission from any higher energy states. The width of the PL peak is approx. 21 meV, typical for InGaAs QWs. Increase in the In concentration by only 3% is sufficient for the formation of 3D islands. This is evidenced in the emission spectra by the appearance of the lower energy emission band centred at 1.327 eV (935 nm) of a much larger width of about 44 meV. The supremacy of the WL emission intensity over the QD ensemble signal is an argument for the low density of QD states. All of them should be filled to observe the emission from higher energy parts of the structure. This effect is too strong to be simply a result of the lower system dimensionality. Most probably it is due to the low surface density of quantum objects in agreement with the SEM image-based estimation of 5×10^9 QDs per cm^2. Another reason that cannot be excluded in the case of the investigated nanostructures is the low number of higher energy states confined in the dots as a consequence of the low localization energy. The PL spectrum supports this possibility showing a small energy difference between WL and QD ensemble emission maxima of approx. 30 meV, which corresponds to the total confinement energy of electron and hole in

the QD. Despite the relatively large QD volume, the number of confined states within the investigated structures is expected to be very limited. No clear signature of the p-shell in the optical spectra of 30 % indium content InGaAs QDs was observed. Energy splitting between the ground and first excited state in similar QDs in the range of 25 - 30 meV were reported [Rei09], which is very close in energy to the wetting layer 2D continuum of states and so cannot be undoubtedly resolved and identified.

For the QD structure with 33 % indium the optical response seems to be a little bit more complex. The dominating emission almost coincides spectrally with the QD-related signal in the previous structure with 30 % indium. On the lower energy side another emission band centred around 1.285 eV (965 nm) is visible. It can be identified as a ground state of the QD ensemble. The domination of emission from higher energy states is a result of high excitation regime. This scenario is supported by the fact that an increase in QD size favours more confined energy states within the QD. It is also in agreement with the low surface density of the nanostructures. On the high-energy side a slight change in the emission band slope can be noted. This can be attributed to the WL emission.

The structure with 36 % indium content also reveals two emission bands. No WL-related signal was recorded. The dominating one coincides with the second (low-energy) emission for the previous case and the second maximum exists at around 1.24 eV (1 μm). That proves that indeed the QD size is strongly enlarged. The $In_xGa_{1-x}As$ energy gap change is much smaller for x in the range between 30 % and 33 % and cannot solely account for the observed redshift. To explain the origin of the multiple emission bands in the higher indium content structures the PL at different excitation conditions at low temperature (5 K) was measured. The respective spectra are shown in (Figure 3-3, Figure 3-4) in logarithmic scale due to large difference in the signal level for extreme excitation powers.

For the 33 % indium structure the power dependence of the shape of the emission band supports the scenario of two different QD sub-ensembles because both emission maxima are present in the spectra at the lowest excitation powers already (Figure 3-3). With the increasing excitation power the spectra evolve towards higher energy side due to the state filling effects.

The situation is completely different in the case of 36 % In sample. At low excitation regime only a single emission maximum is visible and with increasing excitation power the second high-energy peak becomes apparent (Figure 3-4), in agreement with the higher energy state origin of the emission.

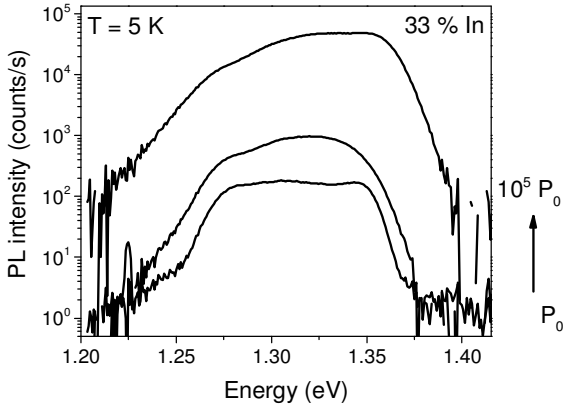

Figure 3-3. Low-temperature PL spectra of 33% In QD structure for various excitation power densities.

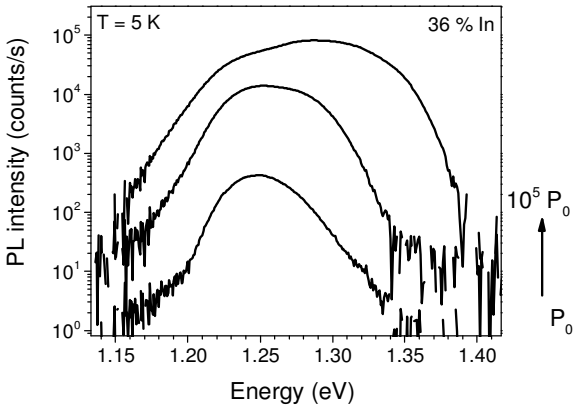

Figure 3-4. Low-temperature PL spectra of 36% In QD structure for various excitation power densities.

For both structures with higher indium concentration the WL emission cannot be resolved. This is a signature of increased total density of states related to the QD ensemble. On the contrary, for the 30 % indium structure the density of QDs is rather low and the number of confined states is very limited due to the shallow confining potential, and as a result the WL emission dominates the optical response of the system.

3.1.2. Thermal quenching of emission from quantum dot ensemble

To get more insight into the electronic and optical properties of the investigated QD structures the temperature dependence of the emission was examined. Based on the thermal PL decay the localization energy for different In content samples was compared. It is very

important in view of applications to identify the main mechanism of carrier losses which limit the performance of the respective photonic devices.

In Figure 3-5 a series of spectra for quantum dot structure with 30 % indium measured at different temperatures in the range from 5 K up to room temperature at high excitation conditions (200 W/cm^2) is presented in the logarithmic scale.

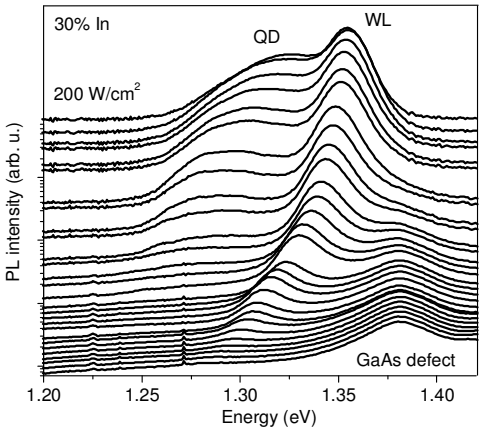

Figure 3-5. PL spectra of 30 % In QD structure for various temperatures (5 K - 300 K) at high excitation conditions (200 W/cm^2).

At low temperatures the emission of both WL and QD ensemble can be clearly resolved. The WL emission preserves up to room temperature. The emission energy follows the InGaAs energy gap changes with temperature. The emission of the QD ensemble cannot be observed for temperatures above 200 K due to too low carrier localization energy. This confirms the relatively shallow confining potential. It is one of the exceptional characteristic of this physical system worth more detailed analysis. At the lowest temperatures the emission intensity integrated over the whole QD ensemble is not strongly altered, due to the carrier redistribution within the ensemble. The carriers from the dots with shallower confining potential are not lost but can be recaptured by the ones having deeper confinement, and hence can further contribute to the emission. At intermediate temperatures another emission band on the high-energy side of the spectrum appears. Its spectral position and intensity does not change with temperature. It cannot be observed at lower temperatures because it overlaps with much stronger emission from the WL. Most probably it is related to some defect state in the GaAs substrate. The origin of this emission was confirmed by the examination of the edge emission under the direct excitation of the substrate.

To analyse the obtained data more quantitatively the natural logarithm of the PL intensity versus the inversed temperature was plotted, i.e. the Arrhenius plot, and fitted with Equation

(2.3), described in Section 2.1.1, assuming a single emission quenching mechanism (Figure 3-6). The activation energy determined from the best fit to the experimental data equals 35 meV, which corresponds well with the energy difference between the WL emission and the maximum of the optical response from the QD ensemble. One has to keep in mind that it is a kind of average value of the activation energy as the size and/or indium content distribution within the QD ensemble translates into the localization energy distribution. This characteristic energy scale points out at the carrier escape to the WL as being responsible for the quenching of the QD emission as it is much lower than the energy distance to the substrate/buffer energy gap.

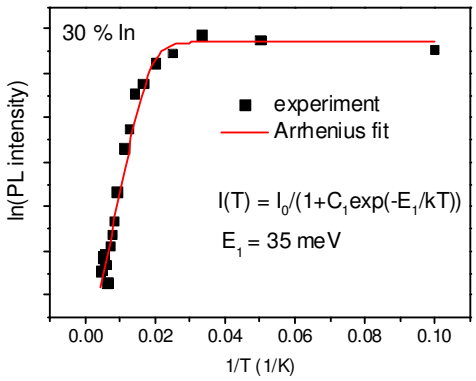

Figure 3-6. PL intensity dependence on temperature in a form of Arrhenius plot for 30 % In QD structure; symbols - experimental data (integrated intensity), solid line - fit according to Equation 2.3 with one activation energy E_1.

On the other hand without proper modelling of the electronic structure it is not straightforward to deduce the escape of which type of carriers is responsible for the exciton dissociation. Unfortunately, there are few reasons limiting the reliability of the modelling. First of all, the localization energy for each carrier type is strongly band offset-dependent with the latter being altered by contributions from both the strain and piezoelectric potential which are not easily predictable without a very reliable calculations. Additionally, QD confining potential is rather shallow, which causes its high sensitivity to the changes in the exact burried QD geometry. Also the indium segregation can lead to complex In profile whose impact on the electronic structure is non negligible. Lack of relevant structural data prevents deeper analysis of the obtained results. However, independently of that the main conclusion that the dominant PL quenching mechanism is the carrier escape to the WL, remains valid.

Interestingly, the PL quenching of emission looks much different at lower excitation conditions. In Figure 3-7 the temperature dependence of emission for low temperatures up to

60 K and excitation power by 2 orders of magnitude lower (on the order of 2 W/cm^2) than in the previously studied case is presented. To emphasize the relative changes in the WL and QD ensemble emission intensity the PL spectra at each temperature are normalized to the maximum peak intensity, no matter the emission of which origin domiantes.

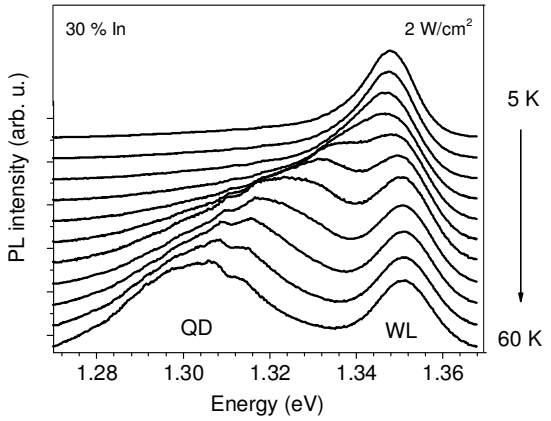

Figure 3-7. PL spectra of 30 % In QD structure for various temperatures in the range of (5 - 60) K for low excitation power (2 W/cm^2).

At low excitation conditions and low temperature the QD-related emission band cannot be clearly resolved any more. It has a form of a low-energy sideband accompanying the much stronger emission from the adjacent WL quantum well. This is in contrast to the state filling behaviour in the case of a standard WL-QD system which should favour the lower-energy QD states at low excitation and enable the emission of higher energy states with increasing number of carriers in the system. This observation suggests the existence of low-energy states related to the WL which are occupied in the first place. The thermally activated character of this process can be a fingerprint of the localized character of WL-related states dominating the emission at low temperatures and low excitation conditions. The localization energy is rather low as the excitation transfer to the QD states is already significant at 20 K but it is higher than the thermal energy at 5 K. When the temperature is increased, the emission intensity ratio between the WL and the QDs is reversed with simultaneous redshift of the maximum of the QD emission. This redshift is much faster than in the case of the QW, which proves that we are dealing with the carrier redistribution within the QD ensemble. The experimental observations can be explained as follows: at low temperature, due to finite capture time of carriers by the localized centres in the WL, carriers cannot minimize their energy and relax to the QD states, but they are rather captured by one of the spatially closest trapping centres. These trapping centres can be the local potential fluctuations due to the composition and/or

WL width variations. It is very important to notice that for a very thin QW even very small imperfections become important, as the relative variation of properties is significant. These kind of states are well-known and are referred to as natural QDs [And99, Bab08, Bay01]. The low surface density of the actual QDs in comparison to the natural QDs is the reason for the supremacy of the WL emission at low temperatures and low excitation conditions. As soon as the carrier distribution within the system is changed either by the temperature and/or excitation power, the possibility of the occupation of the lowest possible states (QDs) is increased. This is caused by the increase in the effective migration length of the carriers. They can be captured/released from different trapping centres many times before they recombine. This suggests that the capture/release times are significantly shorter than the exciton radiative lifetime. The details of the dynamics of this system were examined in time-resolved PL measurements [Syp10] and also using Monte Carlo simulations to confirm the presented scenario [Syp13-1]. These studies revealed a strong decrease of the rise time of QD emission from 50 ps at 5 K down to approx. 10 ps at 35 K. This rise time is much shorter than the exciton lifetime of 350 ps [Rei09].

To confirm the localized character of the lowest energy states in the WL an additional high resolution PL experiment was performed on both the reference InGaAs QW (structure with 27 % In) and the actual WL accompanying the QDs in the 30 % indium structure. At 5 K and for low excitation power the WL localized states should dominate the emission and single sharp emission lines corresponding to single confined exciton radiative recombination should appear on the background of the 2D continuum emission. The respective microPL spectra for the reference QW and the actual WL are presented in Figure 3-8. At both spectra the single emission lines are clearly visible in the spectral range of both WL and QDs emission. The density of WL and QD states can partially overlap spectrally and so the distinction between them is not clear. This brings us to the conclusion that we are actually dealing with a very inhomogeneous QD ensemble containing two QD families: one of intentionally grown low-energy QDs and the higher-energy natural ones formed as a result of WL quantum well imperfections. In this language, the observed thermally-induced excitation transfer is equivalent to the carrier redistribution within the very inhomogeneous QD ensemble (or rather two sub-ensembles) mediated by the 2D continuum of WL states.

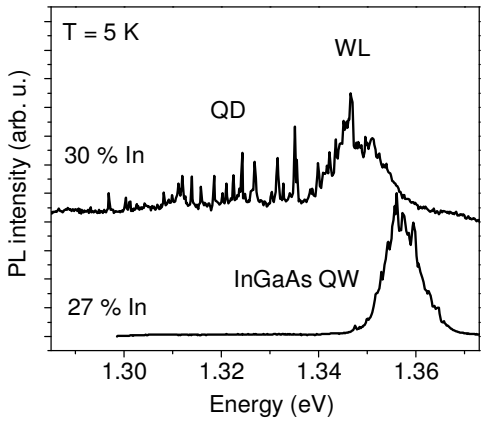

Figure 3-8. Low-temperature µPL spectra of 30 % In QD structure and 27 % In reference InGaAs QW.

To probe the depth of localization potential of the natural QDs on the SQD level the carrier occupation distribution was altered in two ways, i.e. by increasing either the excitation power density (Figure 3-9, Figure 3-10) or the temperature (Figure 3-11, Figure 3-12). These experiments were performed for both the reference InGaAs QW (Figure 3-9, Figure 3-11) and full QD-QW structure (Figure 3-10, Figure 3-12).

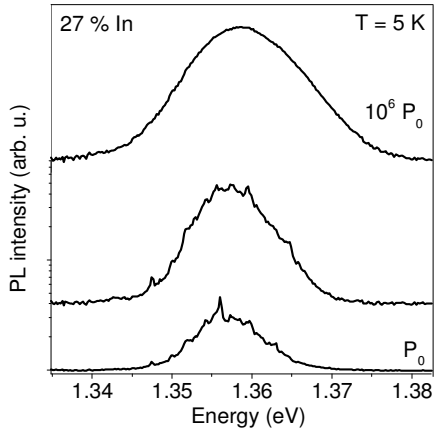

Figure 3-9. The microPL spectra of 27 % In reference InGaAs QW for various excitation power densities.

The behaviour of the PL signal for both samples is similar. At the spectral range of the WL/QW emission a few single emission lines can be resolved at low temperatures and low excitation conditions. With increasing excitation power the emission from 2D continuum of states contributes stronger to the overall emission and the single lines are less and less visible on its background.

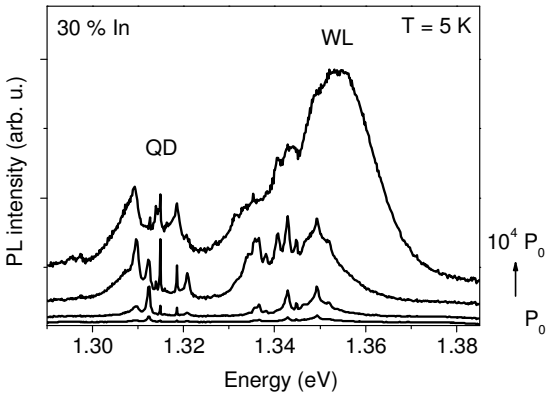

Figure 3-10. The microPL spectra of 30 % In QD structure for various excitation power densities.

Further increase in the excitation power results in two effects: the redshift of the emission maximum due to the increased occupation of higher energy states and the disappearance of the single emission lines. The reason that the emission from localized centres can no longer be resolved in the spectra is the state filling effect and a much shorter exciton lifetime in the case of 2D states in comparison to fully confined states (typically at least one order of magnitude shorter).

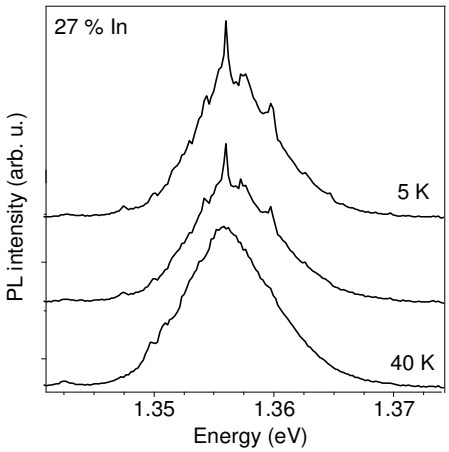

Figure 3-11. The microPL spectra of 27 % In reference InGaAs QW for various temperatures in the range of (5 - 40) K.

The emission from the trapping centres can be clearly distinguished up to 40 K (Figure 3-11, Figure 3-12) which is in good agreement with the previous results that revealed the thermally-induced excitation transfer between WL states and QDs above approx. 30 K. The comparison with the QD-related emission shows that the localization energy is much lower in the case of the trapping centres within the WL than for the actual QD structures. The emission of the

InGaAs QDs is well resolved for 40 K and can be observed even up to 80 - 90 K, preserving its strictly zero-dimensional character (more detailed analysis can be found in Section 3.2.2).

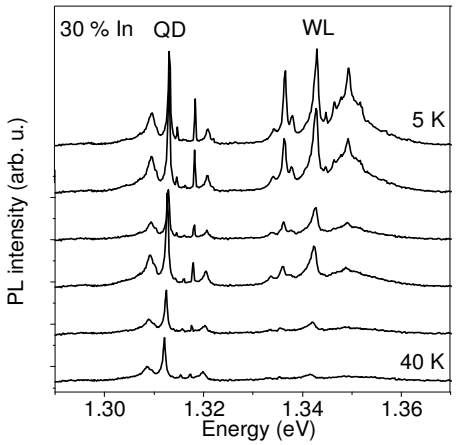

Figure 3-12. The microPL spectra of 30 % In QD structure for various temperatures in the range of (5 - 40) K.

The process of thermal quenching of the PL was studied also for the two remaining samples in the series with 33 % and 36 % indium concentration (Figure 3-13, Figure 3-15, Figure 3-16).

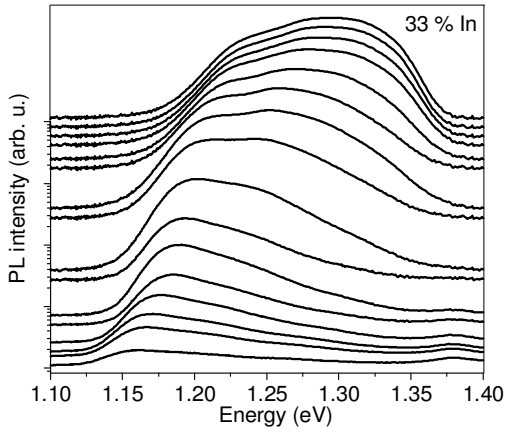

Figure 3-13. PL spectra of 33 % QD structure for various temperatures in the range of (5 - 300) K.

The PL quenching here shows a typical QD-like behaviour. At low temperatures (below 100 K) the WL-mediated carrier redistribution within the QD ensemble determines the emission dependence on temperature. At higher temperatures the energy of the PL maximum follows the band gap energy changes. In the case of 33 % indium sample the higher-energy emission maximum quenching is faster and cannot be resolved at higher temperatures. For the low-energy band the emission is significant even at room temperature. Both observations

confirm previous assignment of those two emission bands to two different QD sub-ensembles. If both the emission maxima are related to the same QD family, occupation of higher energy states is favoured at higher temperatures due to thermally-induced changes in carrier distribution. That is in contrary to the presented data. In the case of two separate QD groups differing in size and so the localization energy, the higher emission energy corresponds to weaker localized structures and as a result a lower thermal energy is enough to enable carrier escape from the QD potential. This scenario is in agreement with presented data as the lower energy emission is preserved up to room temperature, proving a deeper confining potential. The behaviour of the low-energy peak is similar to the 30 % In sample suggesting that indeed one of those two QD families is alike nanostructures in the 30 % In sample. Arrhenius analysis of the emission intensity as a function of the temperature (Figure 3-14) suggests that in this case there are actually two different processes responsible for the PL quenching.

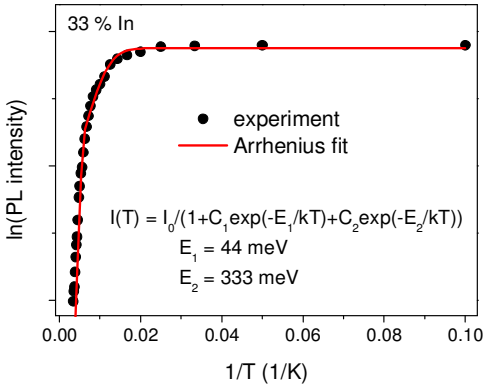

Figure 3-14. PL intensity dependence on temperature in a form of Arrhenius plot for 33 % In QD structure; symbols - experimental data (integrated intensity), solid line - fit according to Equation 2.3 with two activation energies E_1 and E_2.

The PL intensity is integrated over all the QD states to separate the thermal quenching from the effect of the carrier redistribution within the QD ensemble. The two characteristic energies determined by the fitting procedure are 44 meV and 333 meV. The first value is close to the activation energy for carrier escape to the WL obtained for the 30 % indium sample. This is an additional argument for similarity of those two groups of nanostructures. It also proves the importance of the WL as a channel for carrier escape. A higher value of the localization energy with respect to the WL can be a result of averaging over two QD families for which this parameter differs. It is not recommended to increase further the number of parameters in the fitting procedure by inclusion of additional processes, as it reduces strongly the reliability of the results. The determined average value of this activation energy is sufficient for a proper

assignment of the quenching mechanism. The higher energy exceeding 300 meV can be associated with the energy distance to the GaAs substrate bandgap as it is definitely too high to be related to the WL. It concerns only the second QD family (it is absent for the 30 % indium QD structure). In that case the carrier escape to the substrate is more important than to the WL, which can be argued based on the comparison of C_1 and C_2 parameters corresponding to the efficiency of the respective processes (

Table 3-3). The escape of the carriers to the WL is not very efficient due to the high probability of the carriers being recaptured by the QD states. In view of this, the described process does not lead to the irrevocable carrier loss and so the quenching of the PL signal, but is rather a part of the WL-mediated carrier redistribution within the QD ensemble.

In the case of the 36 % indium QD structure the order for quenching emission bands of different energy is reversed, i.e. lower energy emission is visible in a narrower temperature range and so as the temperature is raised the emission of higher energy states dominates in agreement with previous assignment of the higher energy emission band to the higher energy state in the QDs (Figure 3-15, Figure 3-16). At higher temperatures the substrate-related emission occurs in the high-energy part of the spectrum just like in the previous cases.

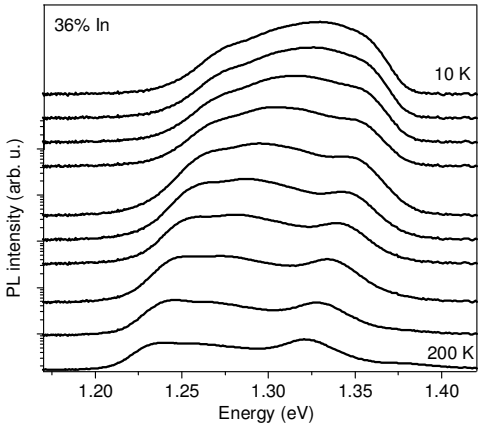

Figure 3-15. PL spectra of 36 % QD structure for various temperatures in the range of (5 - 200) K.

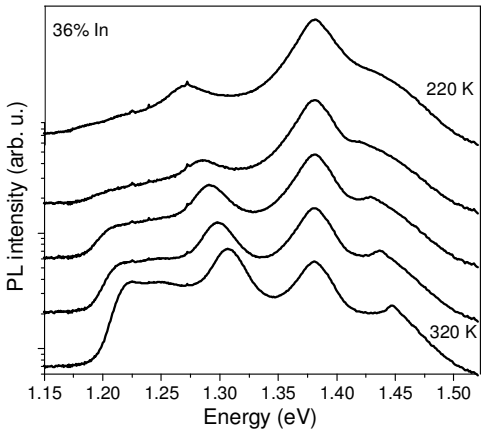

Figure 3-16. PL spectra of 36 % QD structure for various temperatures in the range of (220 - 320) K.

The Arrhenius analysis (performed again for the intensity integrated over the whole QD emission spectrum) reveals two characteristic energies of PL quenching (Figure 3-17).

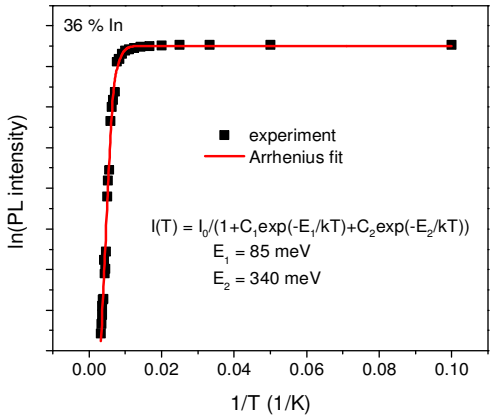

Figure 3-17. PL intensity dependence on temperature in a form of Arrhenius plot for 36 % In QD structure; symbols - experimental data (integrated intensity), solid line - fit according to Equation 2.3 with two activation energies E_1 and E_2.

The first one equals 85 meV and can be interpreted as a carrier localization energy with respect to the WL, which is much higher than in the previous samples, as the QDs are bigger and so the energy levels are confined deeper. This is actually the process of lower importance as its efficiency estimated from the fitting procedure is approximately three orders of magnitude lower in comparison to the second mechanism. Low efficiency of the carrier escape to the WL on the QD ensemble can be traced back to the high probability of the carrier recapture from the WL back to the QDs and so those carriers contribute to the emission anyway, as discussed previously. This probability is increasing with QD surface density so

the efficiency of the carrier loss due to the escape to the WL is decreasing in agreement with the trend observed for the investigated samples (
Table 3-3). The second PL quenching mechanism can be identified as a direct escape of carriers to the GaAs layers and this seems to be the dominating mechanism of PL quenching in the case of those structures. On the contrary to the WL case, the carrier escape to the barriers is irreversible and this is the reason for its much higher efficiency in depleting the occupation of QD states.

The energies determined based on the Arrhenius analysis are summarized in
Table 3-3. For the 30 % indium QDs the confinement potential is rather shallow, with the localization energy of approx. 30 - 40 meV with respect to the WL being the main carrier escape channel. As the In concentration is increased the confinement gets deeper, which is reflected in the increase in the localization energy in agreement with the expected rise of the QD size. Simultaneously the dominating PL quenching mechanism changes towards carrier escape to the substrate with characteristic energy of around 340 meV. This shows the importance of the WL existence for QDs exhibiting shallow confining potential and the diminution of its role the higher the QD surface density. The results presented in this chapter are in a good agreement with trends expected from the growth conditions and previous interpretations of the observed emission bands.

Table 3-3. Activation energies $E_{1,2}$ and parameters $C_{1,2}$ determined based on the Arrhenius fit with Equation 2.3 to experimental data for QD structures with various In content.

In concentration	E_1 (meV)	C_1	E_2 (meV)	C_2
30 %	35	1520	-	-
33 %	44	440	333	8.8E10
36 %	85	4160	340	9.7E11

3.1.3. Polarization of emission

To probe the confining potential anisotropy of investigated structures the polarization-resolved PL measurements were performed. At first the orientation of the main optical axis was determined. The direction of the strongest linear polarization component coincides with the [1-10] crystallographic direction and so the elongation direction of the QDs. Low

temperature (5K) polarization-resolved measurements revealed surprisingly low, taking into account the shape asymmetry, linear polarization degree at the maximum of QD ensemble emission – on the order of 0.06 (Figure 3-18).

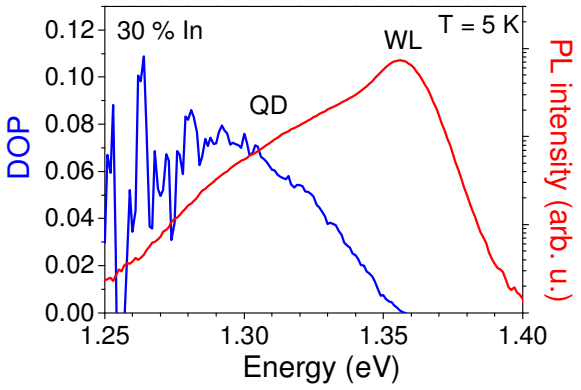

Figure 3-18. Low-temperature spectral dependence of the DOP (blue solid line) together with the PL spectra of 30 % In QD structure (red solid line).

The largest value of the DOP coincides with the QD emission peak at 1.3 eV and decreases towards the sidebands. For higher energies the reason for the DOP decrease can be a stronger contribution of the excited states [Kac11], but also partial spectral overlap of the QD ensemble and the WL states. The DOP drops down to zero in the range of the WL due to circular polarization of the surface emission from the QW. This effect masks the DOP dependence on the emission energy and thus the relation between size and shape of the QD cannot be determined. If the larger dots are simultaneously more asymmetric than the DOP should increase at the low energy side of the ensemble emission. That would be the case if the increased amount of accumulated material results in the stronger elongation, i.e. more available material brings out the asymmetry between different crystallographic directions, which is the most probable scenario. The picture is less straightforward if the changes in the indium content and distribution are taken into account and can result in nontrivial dependence of the ground state energy vs. QD size. This is expected due to In tendency to segregate. A low-energy part of the spectrum reveals significantly decreased signal to noise ratio as the QDs emission is getting weaker and again approaching the DOP equal to zero for the unpolarized background emission.

The first imposing explanation of the low DOP value is an almost symmetric in-plane shape. This can be ruled out by the analysis of the structural data. It is contradictory to the typical geometry of low In content InGaAs QDs on GaAs substrate reported in the literature [Löf06].

Another possible explanation related to rather large QD size is an additional carrier trapping within the individual nanostructure due to potential fluctuations. The origin of these fluctuations can be, e.g., the cross-sectional size variations. This two stage character of the confining potential leads to the existence in the energy ladder of two types of states differing significantly in the electronic and optical properties, i.e., strongly confined almost symmetric low-energy trapped ones limiting the wave function extension and anisotropic higher-energy states extended over the whole QD volume of much weaker confinement. Such potential fluctuations have been previously observed in 1D systems [Güç09, Gui03]. Their influence on the DOP of emitted radiation has been examined in details for QDashes - see further discussion in Section 4.2.2 and [Mus12]. This possibility can also be excluded based on previous experimental results on large and low In content InGaAs QDs. First of all, they indicate increased values of the oscillator strength of the exciton [Rei04, Rei09, Syp10, Sęk10] which suggests enlarged wave function extension. Also the effective exciton radius (15 nm) determined from the magnetooptical study [Rei09] suggests weakened quantum confinement. To check it more in details the thermal dependence of the emission was measured once again separately for two perpendicular polarizations and the DOP dependence on temperature was extracted (Figure 3-19). The DOP should differ significantly depending on whether the emission from the trapped or extended state dominates and increase with the temperature as the emission changes its character from strongly localized to confined within the entire QD.

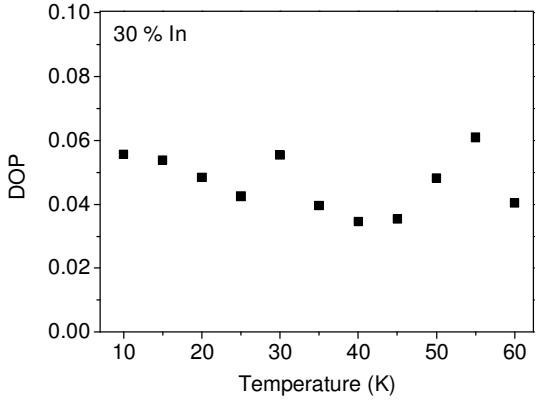

Figure 3-19. The DOP dependence on temperature for 30 % In QD structure.

The polarization properties of the emission do not change with temperature and vary only slightly in the +/- 2% range comparable to the experimental uncertainty. Furthermore, the DOP values for higher temperatures are equal or smaller than the low-temperature ones,

suggesting no change in the character of the emission with possible increase in higher energy states contribution [Kac11] of the same type and characteristic for uniform nanostructures without potential fluctuations [Mus12]. Also, the spectral dependence of the DOP does not differ much from the low-temperature one (Figure 3-20), with only a slight redshift of the DOP maximum.

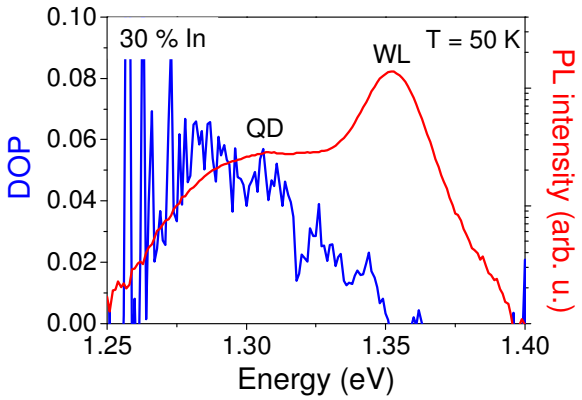

Figure 3-20. Spectral dependence of the DOP (blue solid line) together with the PL spectra of 30 % In QD structure (red solid line) measured at 50 K.

Another explanation of the low DOP value needs to be found. A possibility that should be considered in the case of large nanostructures is the relative strength of the quantum confinement and Coulomb effects due to larger nanostructure physical volume in comparison to the exciton coherence volume determined by the bulk exciton Bohr radius (on the order of 19 nm for 30 % In content). In the strong confinement regime the wave function is extended over the entire QD volume and follows the size and symmetry of the confining potential quite rigorously. As the confining potential is getting weaker the Coulomb interactions become more important and tend to symmetrize the wave function and it should be described rather in the language of centre-of-mass wave function quantization [And99]. This is further confirmed by the influence of the magnetic confinement on the QD wave function extension at relatively low fields (up to 5 T) [Rei09] being a signature of comparable confinement and magnetic energy scales and as a result, a stronger influence of the Coulomb effects in comparison to quantum confinement. The Coulomb effects combined with significant penetration of the wave function into the barrier can explain the observed polarization properties of emission from the QD ensemble and are in agreement with all the previous experimental results. Other abovementioned possibilities have been ruled out. Though one more factor which can make the wave function more symmetric, in spite of the shape asymmetry, is the indium distribution profile [Liu00, Wal01]. Indium tendency to segregation can also lead to more symmetric

confining potential than if it is governed by the shape anisotropy solely. In that case further elongation of the nanostructure will not have dominant impact on the optical properties of the investigated structures. Another possibility is the effect of the shallow confining potential which enhances the wave function in-plane leakage, mainly into the WL area, making it much more symmetric than expected based on the confining potential symmetry. The nanostructure dimension in the growth direction has also an impact on the wave function which is strongly confined in this direction, and which results in the wave function penetration into the barriers, what increases its effective symmetry. In this case the wave function sensitivity to the details of the QD shape is greatly reduced and as a consequence the optical properties would not be determined by the details (most importantly symmetry) of the nanostructure confining potential. However, in the case of the investigated structures the increased in-plane wave function extension cannot be the primary cause of the diminished DOP because the wave function extension determined from the magnetooptical study (15 nm) [Rei09] does not exceed the in-plane dimensions of the QDs (at least 20 - 30 nm width). All these phenomena can result in polarization properties similar to those of more symmetric nanostructures and for the investigated QDs cannot be simply treated as a probe of the shape anisotropy, because the anisotropy degree of the exciton probability density distribution does not follow it. The interpretation of DOP measurements is much more complex and there are more factors that need to be taken into account.

To examine the influence of the exact QD shape on the degree of linear polarization of emission the DOP dependence on the in-plane aspect ratio for investigated structures was calculated by Janusz Andrzejewski (Institute of Physics, WRUT) within the 8 band **k•p** model, for real QD geometry after SEM measurements, i.e. with lens-shaped 30 x 4.3 nm^2 cross section, and 2.7 nm thick WL, including the strain and piezoelectric effects up to the second order in a single particle picture [And10, And13]. The output of this modelling is presented in Figure 3-21 with the symbols being a result of numerical calculations. The black solid line is fit with phenomenological expression of a type

$$y = A - \frac{B}{x^2} \qquad (3.1)$$

whose origin is discussed in Section 4.2.1.

The obtained results indicate that for the assumed cross-sectional geometry (determining the confinement strength) DOP equals 12% is reached for LAR as high as 3.5, rather exceeding the values typical for the investigated structures. The presented DOP dependence on the

confining potential anisotropy has an universal character and was already observed for different kinds of nanostructures [Hu_01, Mus12], with the saturation value of the DOP determined by the details of the confining potential.

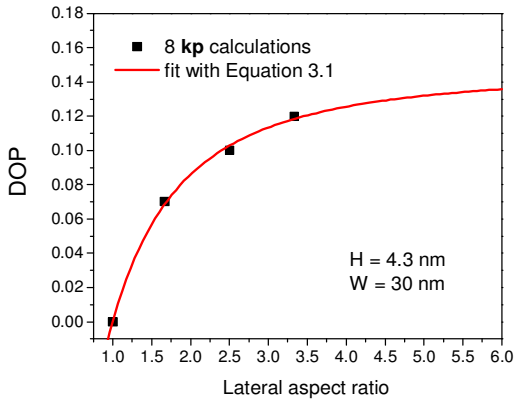

Figure 3-21. Calculated DOP (squared symbols) versus the lateral aspect ratio of a QD of size 4.3 × 30 nm in the lens-shaped cross-section (length changed from 30 to 100 nm). The solid line is a fit according to Equation 3.1.

Polarization-resolved measurements on QD ensemble suggest LAR of the investigated structures in the range of 1.5 - 2 (QD length on the order of 45-60 nm), which is the lower limit of values determined by structural study but the strong variation of dominant polarization contribution from dot to dot can account for the lower value of DOP obtained from QD ensemble emission study. It can also be an effect of assuming a too large QD size in the growth direction, which strongly enhances the valence subband mixing degree and hence the polarization anisotropy (see Section 4.2.1).

Analogical study on the 33 % and 36 % In structures does not provide any additional information about the system. Polarization-resolved measurements confirmed low DOP of radiation emitted parallel to the growth direction in the range of a single percent difference between the samples. The spectral dependence of the emission energy is constant within the experimental uncertainty, being again an argument for the importance of Coulomb effects causing low sensitivity of optical properties to the details of confining potential and so the variations of the QD size and geometry within the QD ensemble.

Polarization-resolved measurements were performed also on the SQD level. Obtained DOP was in the single percentage range and no clear optical axis can be identified. This can be understood as a result of almost symmetric in-plane wave function extension as argued previously, but also due to local strain inhomogeneity on the scale of inter-dot distance (approx 100 nm in the case of investigated low-density structures). It can differ strongly from

dot to dot (variation of optical axis as strong as 20 degree was reported [Ohn11]) and undergoes averaging and does not influence the polarization properties of emission in the case of QD ensemble. This observation is also in agreement with the dominance of Coulomb interactions over the quantum confinement effects and as a result wave function extension not following strictly the direction of QD shape elongation and the in-plane wave function being almost symmetric and thus sensitive to local QD environment.

3.2. Excitonic complexes

In this chapter SQD spectroscopy results on the elongated InGaAs/GaAs nanostructures are presented and discussed. Excitonic and biexcitonic emission has been identified based on the dependence of emission intensity on excitation power density. Relations derived for the stationary rate equation model are further utilized to confirm the origin of both the emissions from the same individual QD. This enables to determine the biexciton binding energy and, indirectly, the relative lifetimes ratio for the exciton and biexciton. In the next step the exciton FSS is determined and analysed. Eventually, the temperature dependence of emission is described, with emphasis on the carrier losses and decoherence mechanisms.

Because of the lowest surface QD density in the order of 5 x 10^9/cm^2 the 30 % In sample was selected for this study as the most promising for the individual QD investigation. The low-temperature experiments were repeated also for the 33 % In sample but the spectrum was neither clear, nor sparse enough to perform further temperature-dependent measurements. No single dot spectroscopy measurements could in fact be realized on the 36 % In sample due to too high QD surface density. On the other hand, the optical properties of these QDs should be similar to the low-energy QD family present also in the 33 % In structure.

The first and very important step in SQD investigation is the optimization of the experimental conditions to find a compromise between the resolution and the signal strength, which in the case of single nanoobject emission is crucial. The optimization process involves not only the equipment parameters (monochromator slit size, grating, numerical aperture of optical elements, etc.) but also, in the case of patterned samples, the optimal mesa size. The smaller the mesa, the smaller the number of QDs excited simultaneously and so the probability of exciting two dots coinciding in ground state energy is lower. This results in optical spectra composed of smaller number of lines and thus better separated and easier for

analysis and further interpretation, as it is easier to identify different excitonic complexes and also to assign lines coming from the same QD. Exemplary spectra for different squared mesas of sizes in the range from 1 µm down to 280 nm at similar excitation conditions are presented in Figure 3-22, illustrating well the described tendency.

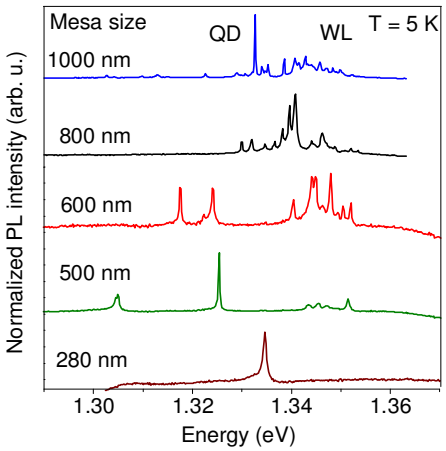

Figure 3-22. Low-temperature microPL spectra of 30 % In QD structure for various squared mesa sizes in similar excitation conditions.

It is important to notice that the small mesas do not contain statistically representative number of dots, so the distribution of the dot parameters and thus the emission energies is not the same as for the QD ensemble. In that scale the local distribution and local surface density of nanostructures determine the spectral position and the number of lines. This is the reason for apparent differences in the spectra for mesas of the same size and so careful inspection of large number of mesas is very useful for finding the optimal mesa size for further optical study. For large mesas it is difficult to resolve single emission lines as a few lines can overlap spectrally and then no further analysis is possible (Figure 3-22). For small mesas in the range of 200 - 300 nm the optical spectra of QDs are composed of truly single emission lines. Unfortunately, the reduction of the mesa size has a limit and in many cases cannot be continued down to the ultimate case of isolating the emission from one QD only. The main limitation is the influence of the mesa sidewalls due to surface defects and the carrier trapping. Radiation-driven fluctuations of their occupation and hence built-in electric field changes in the time scale much shorter than the time of the emission integration. These finally effect in the spectral diffusion. This dynamical broadening is stronger for dots positioned closer with respect to the edge of the mesa, i.e. will in average be enhanced with the decreasing mesa size. This causes significant emission lines broadening and, as a result,

masks the inherent QD properties. The issue of the sample surface patterning as a possible source of additional exciton decoherence is discussed in details in Section 3.2.2. For the QD density given here the mesa sizes in the range of 250 - 300 nm appeared to be optimal for good quality optical spectra. Well-separated emission lines are indispensable for excitonic complexes identification and further study of the decoherence mechanisms. The power and temperature dependence of single emission lines characteristics in a wide range of both the external parameters are required.

3.2.1. Biexciton - exciton cascade

As indicated previously, the 30 % In structure was chosen as the most advantageous for SQD spectroscopy measurements. At first, polarization-resolved PL was measured in order to detect the FSS of neutral exciton. In all the examined cases no FSS was observed within the experimental accuracy (practical spectral resolution of the PL setup is in the range of 50 μeV). Additional difficulty to resolve it was the significant inhomogeneous broadening of the single emission lines in the range of hundreds of μeV (discussed in details in Section 3.2.2), caused by spectral diffusion effects, masking the splitting between the bright excitonic states. Such unresolved splitting can be related to increased symmetry of the wave function in spite of the physical shape anisotropy of the nanoobject itself (as discussed in Section 3.1.3) and its low sensitivity to the exact shape of the confining potential in the weak confinement regime. The low FSS value is in agreement with low DOP of the QD ensemble emission discussed before. Both of them prove that the wave function is much more symmetric and does not follow the shape anisotropy, although the DOP is determined by the single particle phenomenon of the valence band mixing and the FSS is a purely excitonic effect. The small FSS makes the investigated structures promising as an active region for entangled and/or indistinguishable photon sources.

To evaluate the strength of Coulomb correlation effects the biexciton-exciton cascade was examined. To distinguish between the excitonic and biexcitonic emission, the excitation power dependence microPL study was performed (Figure 3-23). Only spectra corresponding to high-excitation conditions (enabling the biexciton formation) are presented, which is the reason of significant background on which the SQD lines appear. The evolution of the emission spectra with increasing excitation power is as expected, i.e. new lines appear in the spectra, the intensity of emission peaks either increases or is already saturated, the

background-related signal increases and finally, the WL continuum (2D states) emission occurs.

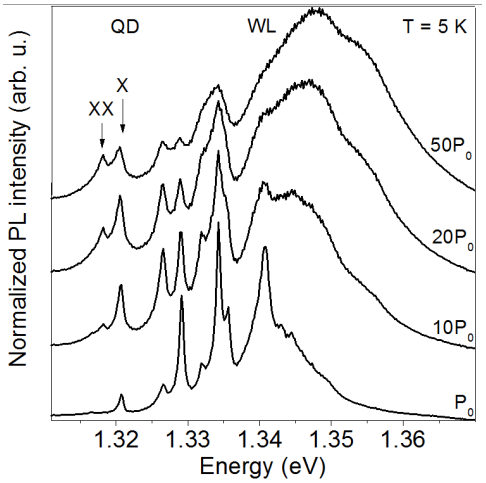

Figure 3-23. Low-temperature microPL spectra of 30 % In QD structure for various excitation power densities.

Candidates for exciton and biexciton can be pointed out from the spectra as their relative emission intensity changes in a very characteristic way: the exciton emission appears at lower excitation power and its intensity increases linearly and finally saturates. On the other hand, the biexcitonic emission should occur at higher excitation and its initial quadratic increase is followed by a slower linear rise and finally surpasses the excitonic emission. Based on the described qualitative behaviour, two lines at the low-energy part of the spectra denoted as X for exciton and XX for biexciton in Figure 3-23 are very promising candidates for biexciton-exciton cascade. Additional advantage of those lines is their spectral position with respect to the QD ensemble emission maximum, decreasing the probability of higher energy states/excitonic complexes origin of those lines and limiting the influence of the background emission, thus increasing the reliability of emission intensity determination. All the observed lines from the spectrum in Figure 3-23 were analysed and the peak intensity of each of them as a function of the excitation power was determined. In Figure 3-24 exemplary analysis for X and XX lines from Figure 3-23 (green and blue symbols, respectively), together with the rate equation model fit to the experimental data (solid lines), is presented. The relative changes in the intensity of those two lines prove their origin from the same QD. Once this relation is established, the biexciton binding energy E_{XX} can be determined. In the presented case it is equal to 2.52 meV, i.e. rather typical for InGaAs/GaAs quantum dots emitting in this spectral range [Mas11].

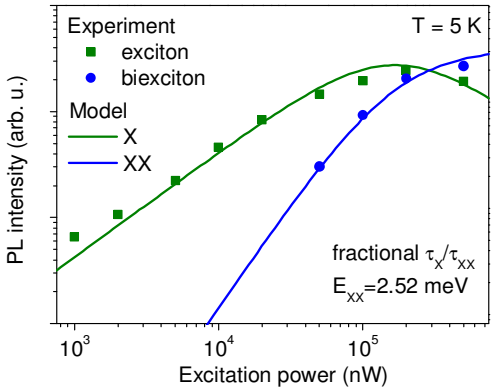

Figure 3-24. PL intensity vs. excitation power analysis (double logarithmic scale) for two emission lines indentified as X (green) and XX (blue), symbols - experimental data, solid lines - fit with three-level rate equation model.

The good fit quality was obtained already for a minimal number of the included levels in the rate equation model (ground state, exciton and biexciton), which agrees well with the shallowness of the confining potential unable to confine many higher energy states. The only adjustable parameter in the fitting procedure for a given number of included levels is the $\frac{\tau_X}{\tau_{XX}}$ lifetime ratio. In the presented case it is less than 1. To make sure that indeed the biexciton lifetime is longer than the exciton one, as suggested by the fit to the experimental data, more detailed study on the character of the emission intensity vs. excitation power density dependence for various model parameters were performed.

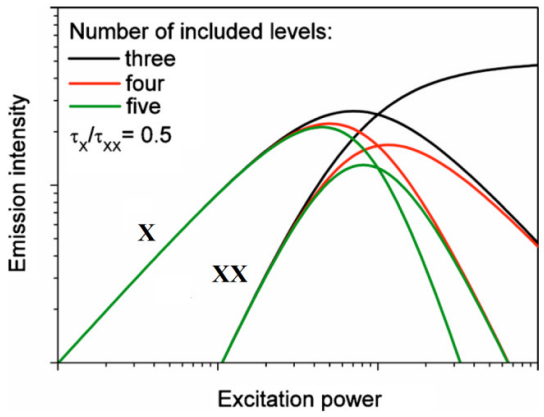

Figure 3-25. Calculated generation rate (excitation power density) dependence of the QD excitonic and biexcitonic emission intensities for their constant lifetimes ratio equal to 0.5 and different number of energy levels considered in the system.

The changes in the theoretical curves simulated for different number of levels included in the model for $\frac{\tau_X}{\tau_{XX}}$ equals 0.5 are presented in Figure 3-25. The main difference between curves is the intersection of the dependence for exciton and biexciton and the high-excitation part. The increased number of included levels result in much faster saturation of the biexcitonic emission, followed by its decrease. This is a result of higher order complex formation being more probable than the biexciton recombination. In this situation mainly the emission from higher energy states is observed, blocking the excitonic and biexcitonic emission.

For the three-level model the only fitting parameter is the exciton to biexciton lifetime ratio. The proportionality coefficients between the generation rate and excitation power density, and also between the emission intensity and recombination rate just shift both curves in a double logarithmic scale, without affecting their shape. To explore how this parameter influences the emission intensity vs. excitation power density dependences for exciton and biexciton, the lifetimes ratio ranging from 0.25 up to 4, were used to calculate respective curves within the three-level model (Figure 3-26).

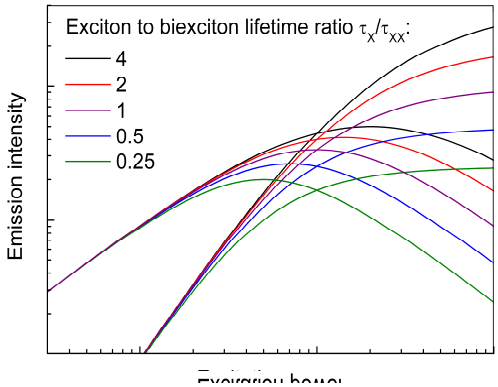

Figure 3-26. Calculated excitation power density dependence on the QD excitonic and biexcitonic emission intensities for various exciton to biexciton lifetime ratios in the three level model.

With increasing $\frac{\tau_X}{\tau_{XX}}$ the intersection point of the excitonic and biexcitonic branches is strongly influenced and shifts towards higher excitation powers, for which the excitonic emission is already saturated, as for the example analysed in Figure 3-24 . In contrary to the effect of including higher levels, the high-energy part of the excitonic curves declines much slower with decreasing lifetime ratio. These analysis confirmed that experimental result

cannot be reproduced by simply including additional energy levels, but the $\frac{\tau_X}{\tau_{XX}}$ decrease down to values close to, or even smaller than one is necessery. This is a signature of a weakened confinement regime [Wim06, Nar06] indeed expected for these relatively large nanostructures. The small value of $\frac{\tau_X}{\tau_{XX}}$ indicates that the exciton lifetime is similar or shorter than the biexciton one. This is possible in significantly weakened confining potential, as the oscillator strength (and hence the radiative recombination lifetime) increases with the coherence volume which is approximately proportional to the physical volume over which the wave function is extended [And99]. The effective coherence volume for each of the electron-hole pairs constituting the biexciton is smaller than for an individual exciton itself, which can lead to the inversed $\frac{\tau_X}{\tau_{XX}}$ ratio (biexciton lifetimes longer than the exciton ones). In Figure 3-27 the possible values of the discussed lifetime ratio are schematically summed up. Identifying them properly can provide an insight into the carrier kinetics of the investigated system, which can give further information about the confinement regime and the internal kinetics of the bright and dark exciton states [Nar06].

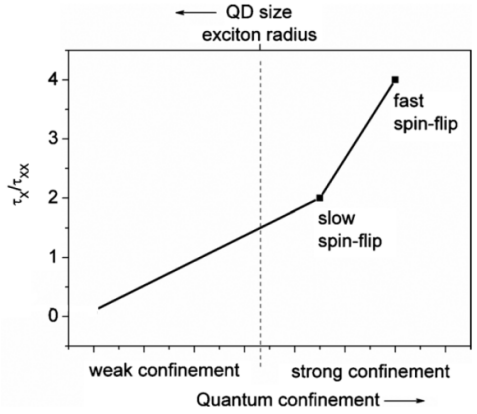

Figure 3-27. The sketch of the exciton to biexciton lifetime ratio dependence on the quantum confinement regime (QD size) [Wim06, Nar06].

To further confirm the fractional value of $\frac{\tau_X}{\tau_{XX}}$ and prove its representativeness, more examples of exciton-biexciton pairs were analysed. The cases for which the high-energy intensities can be reliably extracted are the most interesting ones, because the differences introduced by varying this parameter are most striking in this regime. An example is

presented in Figure 3-28 with the inset showing the evolution of the PL spectra with the increasing excitation power density.

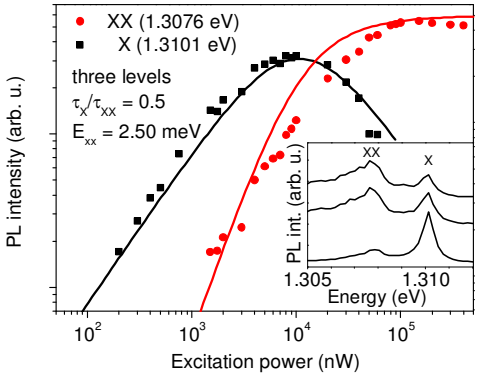

Figure 3-28. PL intensity vs. excitation power density analysis (double logarithmic scale) for two emission lines indentified as exciton (X) and biexciton (XX), symbols - experimental data, solid lines - fit with three-level rate equation model, inset - microPL spectra for various excitation power densities.

The fit to the measured data follows well the experimental tendency when including only three levels in the model and $\frac{\tau_X}{\tau_{XX}}$ equaling 0.5, in agreement with the previously discussed case confirming a lack or at least negligible influence of higher energy states confined within the QD and the rather weak confinement regime. The biexciton binding energy for this case is also very similar - 2.50 meV. The intensity dependence on the excitation power density for high excitation conditions (above the intersection point for the excitonic and biexcitonic curves) decreases much too slow to be an effect of the higher energy states occupation but is not as fast as in the case of $\frac{\tau_X}{\tau_{XX}}$ equal 2, proving that indeed in the described case the kinetics of the biexciton - exciton cascade is governed mainly by the coherence volume due to the weakened confining potential.

To gain more insight into the character of the confining potential and Coulomb correlations in the investigated structures the biexciton binding energy was examined for many exciton - biexciton pairs to obtain its dependence on the exciton emission energy which in most cases reflects simply the QD size. The obtained dependence is depicted in Figure 3-29, together with the PL spectrum from the QD ensemble to define the exciton emission energy with respect to the ensemble emission maximum. The idea behind this summary is to find out what is the trend of the biexciton binding energy dependence on the exciton emission

energy in order to see to which confinement regime the investigated structures can be classified, as the biexciton binding energy vs. QD size dependence is expected to have a maximum [Nar05] distinguishing strong and weak confinement regimes.

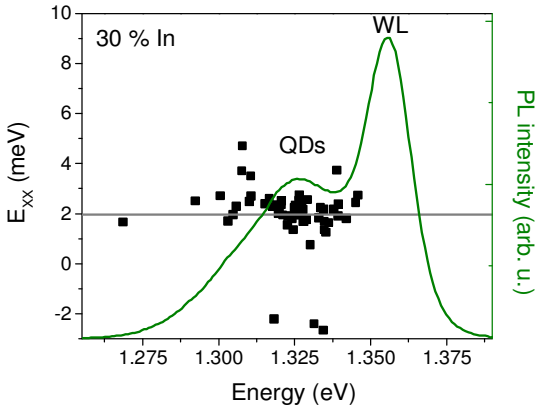

Figure 3-29. Biexciton binding energy dependence on the exciton emission energy (symbols) with the low-temperature PL spectra of 30 % In QD structure (green solid line) and the mean value of the positive biexciton binding energies (grey horizontal solid line).

For the 30 % In structure no clear dependence between the biexciton binding energy and the exciton emission energy can be observed. It seems to be constant, however, the scattering in determined biexciton binding energy values from dot to dot is rather large and might not be intrinsic to QDs, but caused by the variation of QD local environment, e.g., due to patterned sample surface. Most of the cases exhibit the biexciton binding energy in the range of 1 - 3 meV in agreement with results previously reported for InGaAs/GaAs QDs [Mas02, Mic03, Mas11], with a few cases of antibinding biexciton states. As the cases of the negative biexciton binding energy do not appear on the border of the QD distribution but at random exciton emission energies, the most probable explanation is the stronger localization of carriers due to potential fluctuations within an individual QD. If it will be simply related to the random much smaller dots they should all appear at high-energy side of the ensemble emission which is not the case here. The effect of the additional carrier trapping has negligible contribution in the case of the overall emission of the QD ensemble but single cases of carrier trapping phenomena can occur if the emission is examined on the SQD level and on a lot of QDs. (Further discussion and spectral features of the carrier trapping are presented in Section 3.2.2, in which the temperature dependence of the emission is described.) This is the reason for not including the negative biexciton energy cases in the calculation of the mean value of the biexciton binding energy - they are certainly not representative for investigated strustures.

The mean value of all observed positive cases is approximately 2 meV (grey horizontal solid line in Figure 3-29). The lack of a clear dependence on the exciton emission energy has two possible reasons. First of all, the changes in QD parameters within the ensemble can be too small to influence the biexciton binding energy significantly as it was shown that in the strong confinement regime the Coulomb correlations are unaffected as long as the number of states confined within the QD is not significantly altered [Sch09, Moo13]. The strongest impact on the QD electronic structure will have the QD size in the direction of the strongest quantization (QD height), which is not expected to vary much and the lateral dimensions are already quite large, so their variation are not that important any more. To probe the wider range of exciton emission energies analogical experiments were performed on the 33 % In structure, which broadens the covered spectral range up to 80 meV, but no significant change in the biexciton binding energies was observed for the QD family specific for this sample (QD1 in Figure 3-30). The biexciton binding energy varies in the range of 1 - 3 meV with the mean value for the positive cases equal approx. 2 meV (grey horizontal line in Figure 3-30) and again no clear dependence on exciton emission energy can be observed. Also single cases of negative values corresponding to antibinding biexciton states were recorded.

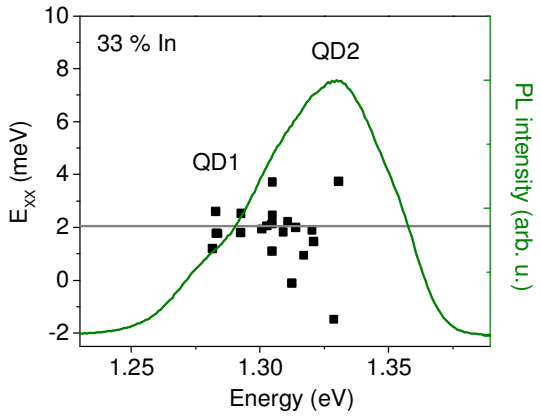

Figure 3-30. Biexciton binding energy dependence on the exciton emission energy (symbols) with the low-temperature PL spectra of 33 % In QD structure (green solid line) and the mean value of the positive biexciton binding energies (grey horizontal solid line).

These results suggest that the exciton emission energy cannot be treated simply as a measure of QD size, but it is strongly influenced also by other QD parameters, changing simultaneously. That seems to be the case for investigated structures due to mutual dependence of QD size (geometry) and In content. The previous magnetooptical study on SQD level also suggests that the emission energy is a trade-off between In content and QD

size [Pet11]. This conclusion is based on the experimental observation that larger diamagnetic coefficients coincide with higher emission energy, which is opposite compared to expectations in the case of the emission energy governed by the QD size only. That result can be explained by the higher In content of smaller dots, which lowers the emission energy and even overcomes the size effect. This suggests that the exciton emission energy is mainly driven by the In content distribution within the QD ensemble (so by the band gap energy variation actually). The fact that the In-rich QDs are smaller can be understood by the increased strain due to higher In content.

3.2.2. Effect of temperature on single quantum dot emission, exciton decoherence

To describe the main decoherence mechanisms, the temperature dependence of SQD emission was examined. The exemplary result of microPL spectra for different temperatures in the range of 5 - 60 K is presented in Figure 3-31.

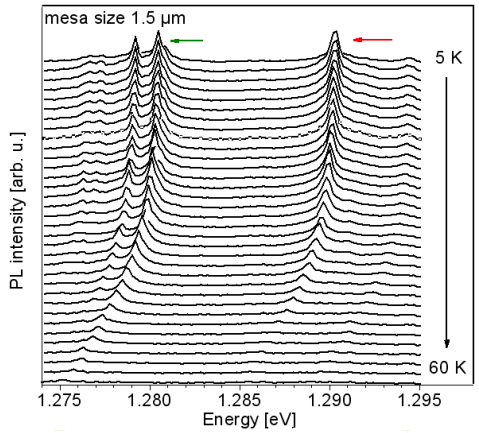

Figure 3-31. The microPL spectra of 30 % In QD structure from 1.5 µm mesa for various temperatures in the range of (5 - 60) K.

The Arrhenius analysis reveals one activation energy, differing from dot to dot in the range of 15 - 35 meV (typical examples are shown in Figure 3-32 - red and green symbols) which can be assigned to the localization energy with respect to the WL, in agreement with the results on the QD ensemble (black symbols in Figure 3-32). This is an evidence that releasing carriers to the WL is the main carrier loss mechanism. Smaller values of the determined activation energy correlate with lower emission energy, reflecting the quantum dot ground state energy distribution.

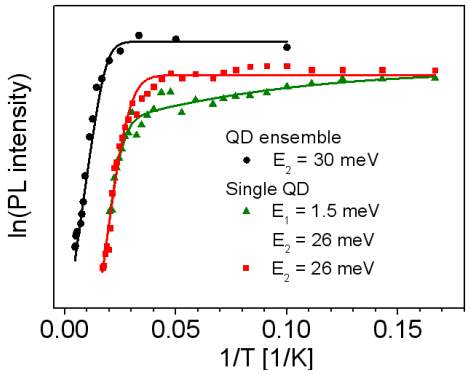

Figure 3-32. PL intensity dependence on temperature in a form of Arrhenius plot for 30 % In QD structure; symbols - experimental data for QD ensemble (black dots) and SQDs (red squares and green triangles), solid lines - fit according to Equation 2.3 with either one or two activation energies E_1 and E_2.

This trend is depicted in Figure 3-33, with a green line being only a guide to the eye. The included error bars are rather large as a result of high sensitivity of emission intensity to any instabilities in the experimental setup and the necessity of objective focus correction at each temperature, due to the thermal expansion of the sample holder together with small depth of focus of the large numerical aperture optics. For most of the single emission lines this is the only activation energy observed just like in the case of red symbols in Figure 3-32. Very few examples of different behaviour were found (green symbols in Figure 3-32). In those cases the second rather small activation energy in the range of 0.5 - 3 meV occurred (most of them within the experimental accuracy estimated to be on the level of 1 meV). This could be a fingerprint of the carrier trapping on potential fluctuations within an individual QD. This second activation energy cannot be observed on the QD ensemble level due to the redistribution of carriers.

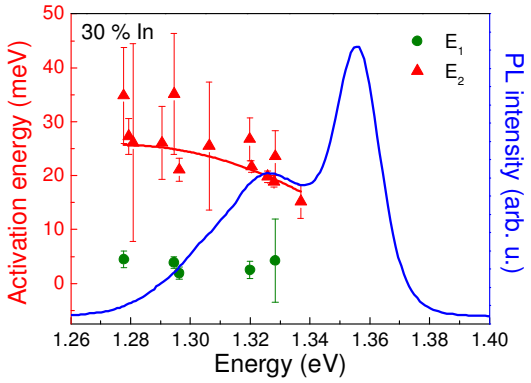

Figure 3-33. Activation energies (green circles — E_1, red triangles — E_2) dependence on QD emission energy obtained from SQD experiments (red solid line is the guide to the eye) shown against the PL spectra of the 30 % In QD ensemble (blue solid line).

The occurrence of the second activation energy in a very limited number of cases suggests that the QDs are generally uniform (which is also evidenced by SEM images of sample surface [Löf06, Pol06]) and the range of values for this energy shows that in the case of existence of the trapping potential its localization energy is extremely low and can be usually neglected for the emission even at low temperatures. Additionally, the fitting procedure revealed that the efficiency of this second quenching mechanism is by three orders of magnitude lower than that of the main carrier loss mechanism. This implies that the exciton is usually extended over the whole QD volume, which corresponds well with previous observations indicating increased oscillator strength in these structures [Rei04]. The 2nd smaller energy is basically independent of the emission energy, which further confirms its origin, because potential fluctuations are randomly distributed within the QD ensemble and the depth of those fluctuations is also random and because of that no activation energy dispersion is expected. Limited number of QDs revealing the possibility of additional carrier trapping is in a agreement with observationd of only a few exciton-biexciton pairs with exhibiting negative binding energy.

In the second step the emission linewidth defined as the full width at half maximum was analysed. Low-temperature linewidths differ strongly from dot to dot in the wide range from 100 μeV to 2 meV (with single exceptions of higher values), but for most of the dots it is in the range of 200 - 600 μeV (Figure 3-34). Smaller values of FWHM were not observed and this is definitely above the spectral resolution of the experimental setup (approx. 50 μeV). This is already much more than the homogeneous lifetime-limited linewidth, which for 350 ps radiative lifetime should be about 5 μeV. This shows that even though the exciton lifetime is strongly decreased in comparison to QDs with stronger quantum confinement, it is not the limiting factor for the exciton coherence at low temperatures. The Gaussian-like line shape points out at spectral diffusion effects to be the dominating exciton decoherence mechanisms.

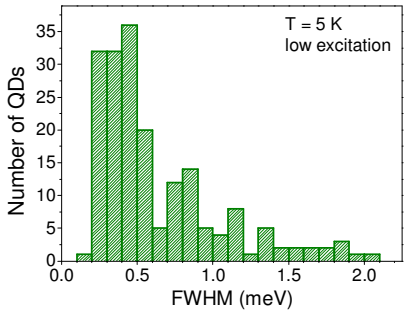

Figure 3-34. The histogram of the low-temperature FWHM of single emission lines for 30 % In QD structure.

The distribution of the FWHM values within the QD ensemble is presented in Figure 3-35 (black squares), together with the QD ensemble emission spectrum (green solid line). It is hard to find a clear trend but it seems that there are less low FWHM cases for higher energy dots (red line in Figure 3-35 is a guide to the eye). This effect cannot be related to the lifetime distribution within the QD ensemble due to its minor contribution to the overall linewidth but it is rather a result of higher sensitivity of smaller dots to spectral diffusion effects. The huge variation of the FWHM values independent of QD emission energy is an effect of changes in the environment rather than something specific for the QDs themselves, which supports the interpretation of the dominant role of the spectral diffusion effects.

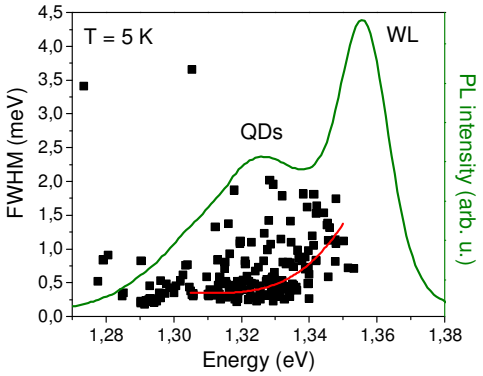

Figure 3-35. Low-temperature spectral dependence of single emission lines FWHM (symbols) with red solid line being guide to the eye and PL spectra of 30 % In QD structure (green solid line).

The origin of the spectral diffusion in the case of the investigated structures is twofold. First of all, it may be caused by the interaction with the WL localized long-living excitons [Dus12, Sęk10] that changes the emission energy of the QD (bi)excitons and so manifests as an effective line broadening in the time-integrated spectra.

Another source of the spectral diffusion is related to mesa sidewalls and carrier trapping centres related to them. The number and proximity of trapped carriers with respect to a given QD fluctuates in time and so again causes its effective broadening, when time-integrated spectra are measured. This effect should be stronger for smaller mesas, as in that case the probability of finding a QD near the mesa sidewalls is larger for them. To investigate it more in detail the FWHM dependence on temperature for QDs in mesas of various sizes was extracted from microPL measurements. In Figure 3-36 representative data for 240 nm, 260 nm, 600 nm and 2 μm mesa sizes are presented in different colours. For each mesa size a few QDs were examined. The differences between them result from different spatial position

of the QD with respect to the mesa sidewalls. The general tendency is as expected, i.e. at low-temperature the FWHM is larger for smaller mesas and can be as large as 2 meV. One has to keep in mind that for a small mesa, the probability that a QD is located closer to the mesa edges is higher, but still there is a possibility to find a QD which is located more in the centre of the mesa and so not that strongly influenced. As always in the case of SQDs, the local environment is very important and the properties are not averaged out like in the case of the ensemble emission. This is the reason for some exceptions of the tendency described above. Another experimental observation is that the increase in the FWHM is much faster for stronger spectral diffusion, which can be an effect of further enhancement of the carrier trapping as the occupation distribution changes with temperature in favour of higher energy states and the time scale of the fluctuations is altered. This can be better seen in Figure 3-37 where the dependences for different mesa sizes can be compared easier, as the initial (low-temperature) value of the FWHM was subtracted for clarity.

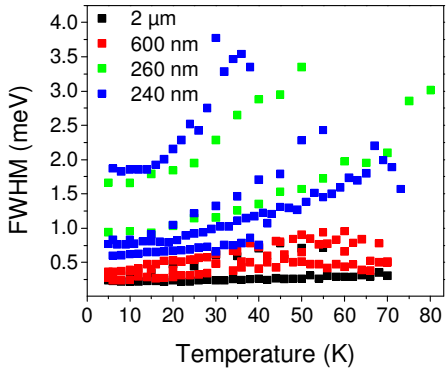

Figure 3-36. The FWHM of single emission lines dependence on temperature for various mesa sizes (different colours) for 30 % In QD structure.

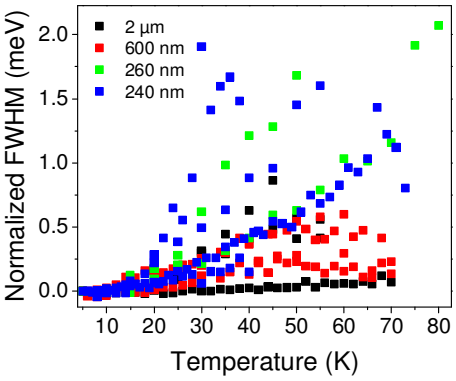

Figure 3-37. The FWHM of single emission lines dependence on temperature for various mesa sizes (different colours) for 30 % In QD structure. The low-temperature initial FWHM values were subtracted to simplify the comparison.

This behaviour can be actually explained even in the case of temperature independent spectral diffusion, which is shown in Figure 3-38. The presented result is in in agreement with an outcome of simplified theoretical modelling assuming quantum-box-like potential and including the interaction with acoustic phonons as a source of temperature increased decoherence. These calculations were performed by Paweł Machnikowski (Institute of Physics, WRUT). The spectral diffusion effects are mimicked by the Gaussian profile with the FWHM (indicated by the captions in Figure 3-38) varying from 0.1 up to 0.5 meV. The overall emission line is a convolution of a Lorentzian ZPL, acoustic phonon sidebands and Gaussian-like spectral diffusion contribution. The reason for faster increase is also related to the choice of figure of merit, i.e. the FWHM. The ZPL contribution is not separated from the phonon sidebands and as a result the FWHM is the linewidth of the convolution of those two (the overall emission).

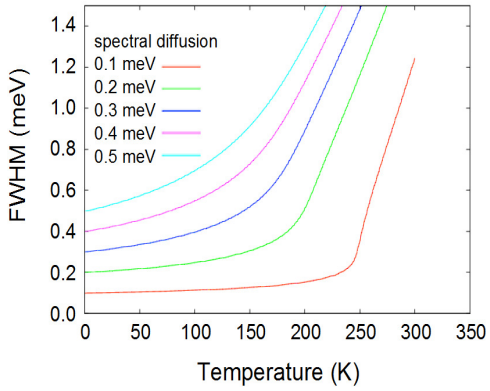

Figure 3-38. Calculated FWHM dependence on temperature for various spectral diffusion contributions (differrent colours).

At some point the FWHM increases abruptly and the main reason is the increased sidebands contribution which is so large that their intensity exceeds the half maximum point and the experimentally determined FWHM becomes rather a measure of phonon sidebands spread (Figure 3-39).

To describe the phonon-induced decoherence and minimize the spectral diffusion contribution many single lines with relatively low initial linewidths were analysed. The microPL spectrum of a large mesa is rather dense and so the well-separated emission lines in the low-energy tail of QDs ground state distribution were chosen (e.g., like those marked with red rectangular frame at low-temperature spectra of 2 μm mesa in Figure 3-40).

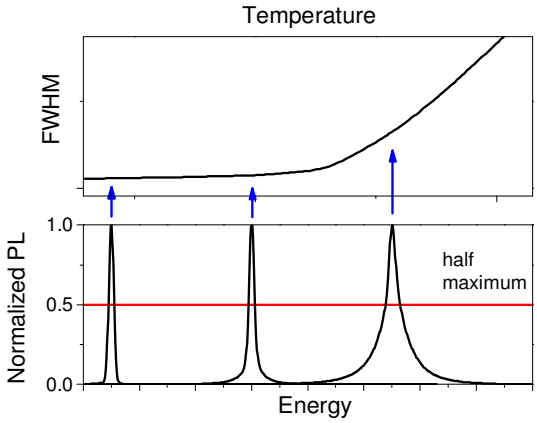

Figure 3-39. The typical FWHM dependence on temperature shown schematically (upper panel) together with normalized emission spectra (lower panel) at selected temperatures (marked by blue arrows). Red horizontal line shows the half maximum of the emission peak.

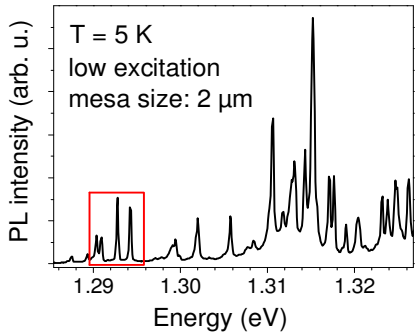

Figure 3-40. The low-temperature microPL spectra of 30 % In QD structure taken from squared 2 µm mesa size. Emission lines further investigated in details are marked with red rectangle.

In the magnification of the part of the spectra of interest in Figure 3-41 no phonon-induced spectral features can be resolved in agreement with the decreased visibility of acoustic phonon sidebands in nanostructures exhibiting weaker confining potential. This is due to the decreased exciton-phonon coupling constant and the number of phonon modes which can be effectively coupled to excitons confined in QDs (reduced cut-off energy discussed in Section 1.2.4).

As the temperature is increased, the lines become broader and redshifted due to the thermal reduction of the band gap energy. The background emission is also enhanced and the adjacent lines start to overlap spectrally due to increased linewidth bases, which makes the FWHM determination less accurate (Figure 3-42).

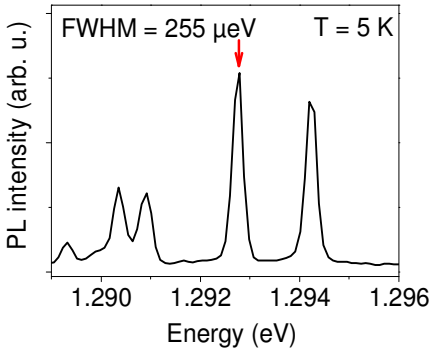

Figure 3-41. The low-energy part of microPL spectra (marked with red rectangle in Figure 3-40) from 2 µm mesa on 30 % In QD structure (5 K). The red arrow marks the emission line for which the temperature dependence is further analysed.

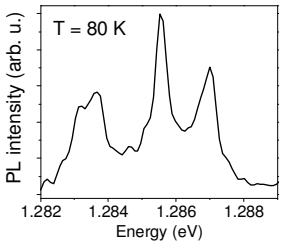

Figure 3-42. The low-energy part of microPL spectra from 2 µm mesa on 30 % In QD structure (80 K).

The FWHM dependence on temperature in the whole range in which the single line emission can be observed is presented in

Figure 3-43. The initial value of the FWHM is relatively low, equal to 255 µeV, and is not setup resolution-limited. It also proves low spectral diffusion contribution in comparison to the other emission lines (Figure 3-34). In the low temperature range the FWHM increases slightly due to increasing contribution of the phonon-assisted emission to the Gaussian broadened and spectral diffusion dominated peak. For temperatures around 60 - 70 K the FWHM starts to increase abruptly and the reason for that behaviour can be the increased acoustic phonon sidebands contribution to the overall emission and the fact that mainly the phonon sidebands width is probed at higher temperature, as discussed previously. The temperature in which the slope of the increase changes is related to the exciton-phonon coupling strength which controls the contribution of phonon sidebands to the overall emission in the case of low cut-off energy for exciton - phonon interaction. The lowered cut-off energy is a reason for no changes in phonon modes occupation with temperature. This is caused by the fact that all phonon modes that can effectively couple to the QD excitons are already

occupied at low temperature. In that sense this temperature is characteristic for the investigated structures but it can be strongly affected by the spectral diffusion effects.

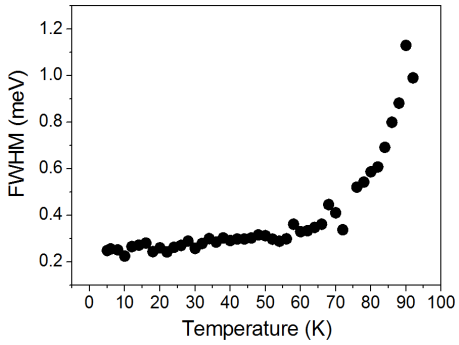

Figure 3-43. The temperature dependence of FWHM for emission line marked with red arrow in Figure 3-41.

Phonon-induced changes in the FWHM were simulated again in the model not taking into account the details of confining potential and including interaction with acoustic phonons via the deformation potential mechanism[1]. The obtained results (
Figure 3-44) show that indeed the decoherence processes due to phonons are diminished for more elongated structures, which is a very interesting result in view of applications.

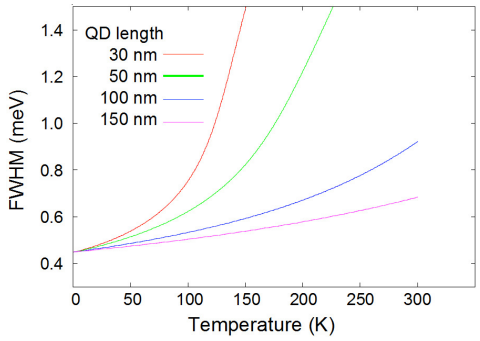

Figure 3-44. Calculated FWHM of single emission line dependence on temperature for various QD lengths.

[1] Calculations performed by Paweł Machnikowski (Institute of Physics, WRUT).

4. Optical properties of InAs/InP quantum dashes

The following chapter is devoted to the structures with QDashes differing mainly in the nanostructure cross-sectional size controlled by the amount of deposited QDash material, varying in the range of 0.7 up to 1.3 nm. The length of all of those QDashes is large exceeding 100 nm, resulting in a large QDash volume together with a strong in-plane shape anisotropy. The interest in these structures was originally provoked by the optoelectronic applications in the telecommunication [Rei07] due to emission in the near infrared range: 1.3 - 1.55 μm and several other properties making them favourable for some of the laser applications (see Section 1.3). The aim of this study is to investigate the influence of the strong in-plane shape asymmetry on optical properties of such nanostructures and also to evaluate their application relevance in future SQD-based devices, with emphasis on the polarization properties of the emission and decoherence mechanisms. The chapter is organized as follows: at first the influence of the amount of deposited InAs on the ground state energy of QDashes is examined. Then, the main PL quenching mechanisms are identified and the factors determining the polarization properties of emission in the case of strongly elongated nanostructures are described. The influence of the overall QD geometry and the main driving factors of the DOP in the case of the surface emission are discussed. The obtained results show that for proper quantitative interpretation of polarization-resolved measurements the overall QD geometry has to be taken into account as the exact size in the growth direction has a pronounced influence on the absolute value of the surface emission polarization degree. As a result of polarization-resolved study the existence of additional carrier trapping centres, i.e. potential fluctuations within the individual QDash (due to its large size in the elongation direction) was revealed and so the usefulness of polarization properties of emission as a probe of additional localization effects in the case of strongly elongated nanostructures was proven. The second part of this chapter contains results of SQD spectroscopy, and in particular, the excitonic and biexcitonic emission, exciton FSS and decoherence mechanisms.

4.1. Electronic structure

The electronic structure of QDashes differs from the one for standard strongly confined QDs, i.e. the inter-level spacing is much smaller due to the large size in the

elongation direction, but the ground state energy is mainly determined by the QD height and further elongation does not alter it much [Kac12, Syp13, Mar13]. At first, the PL from the QDash ensemble was examined to determine the ground state emission energy and the homogeneity of the QDash ensemble. Then, the electronic structure was probed by photoreflectance to identify the higher energy state transitions. The next step was to identify the main PL quenching mechanisms and the depth of the confining potential and how it varies between the samples within the series.

4.1.1. Emission from the quantum dash ensemble

The series of samples under investigation differs in the amount of deposited QDash material. The InAs layer thickness changes from 0.7 nm up to 1.3 nm, which influences mainly the cross-sectional size, but preserves the general QDash geometry [Sau05]. The increased amount of QDash material also enhances slightly the length (but this is already much larger than for typical QDs) and the nanostructures surface density. As a result the ground state energy of QDashes is altered. The emission from QDash ensemble at low temperature (10 K) is centred at 0.813 eV, 0.869 eV and 0.998 eV for InAs layer thickness equal to 1.3 nm, 1.05 nm and 0.7 nm, respectively (Figure 4-1). This corresponds to the approximate changes in cross-sectional dimensions from 12 x 2.5 nm^2 to 20 x 3.5 nm^2 (with QDash height being the direction of the strongest confinement). These dimensions are estimated based on the trends observed for calibration samples grown in similar conditions, for which cross-sectional Transmission Electron Microscopy (TEM) images were taken [Sau05]. The correspondence of those two groups of structures, as far as QDashes are considered, can be argued due to the same emission energy of the 1.03 nm InAs sample in the calibration series and the 1.05 nm sample in the investigated one [Sau05]. This proves that the growth conditions are close enough that the formation of the nanostructures and their morphology is not strongly altered.

The inhomogeneous broadening of the QDash ensemble emission is the largest for the structure with the lowest InAs layer thickness and equals 48 meV and slightly lower for the two longer wavelength structures - in the range of 39 meV. Larger inhomogeneous broadening for the smallest QDashes can be a result of the in-plane dimensions distribution (which in that case can still slightly influence the emission energy) or the variations in size in

the cross-sectional directions, as in the case of cross-section as small as 12 x 2.5 nm^2 even small fluctuations can have substantial impact on the energy of the ground state.

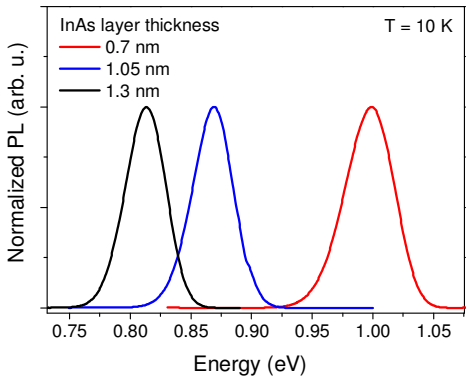

Figure 4-1. The PL spectra of InAs/InGaAlAs/InP QDash structures for various InAs layer thickness.

For all investigated QDash structures the inhomogeneous broadening is larger than for more symmetric nanostructures in the same material system [Gil10]. This is advantageous in applications were a broad gain function is required but less relevant for maximizing the gain at a given wavelength. In spite of this, InAs/InP QDashes were proven to be a beneficial active region for both types of devices, as the large inhomogeneous broadening is compensated by the high nanostructures surface density [Rei07]. Taking into account the energy gap thermal coefficients for InAs material, the long wavelength structures are promising to obtain emission at the third telecommunication window of 1.55 µm at room temperature. The temperature dependence of the emission from the QD ensemble is examined in details in the next chapter.

To probe higher-energy electronic levels, important for understanding the carrier relaxation and emission quenching mechanisms, the photoreflectance absorption-like technique was utilized. The positions of PR resonances (blue line in Figure 4-2, Figure 4-3, Figure 4-4), corresponding to the QDash ground state, are in agreement with previous PL measurements (Figure 4-1). The obtained results further confirm that the total density of available QDash states increases with increasing nominal InAs layer thickness. For similar excitation conditions, the emission from higher energy states within the structure (WL) can be observed only for structure with 0.7 nm InAs (Figure 4-2). In that case the density of states is low enough (due to lowest QDash density and smallest number of confined states) that the

WL emission at 1.140 eV can be observed. For the other samples only the QDash ground state is sufficiently occupied (Figure 4-3, Figure 4-4).

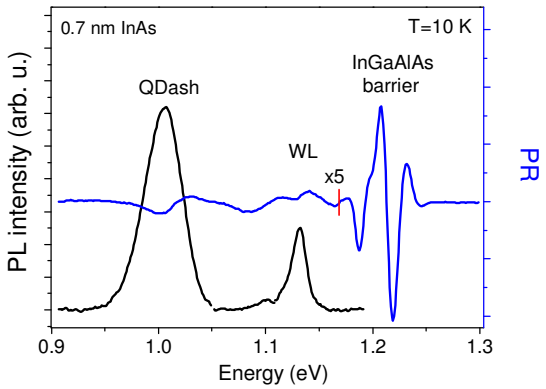

Figure 4-2. Low-temperature photoluminescence (black) and photoreflectance (blue) spectra for 0.7 nm InAs structure.

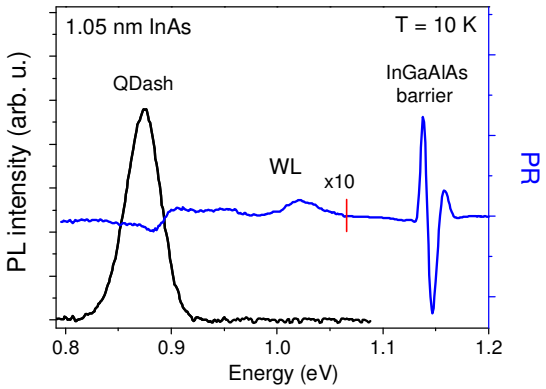

Figure 4-3. Low-temperature photoluminescence (black) and photoreflectance (blue) spectra for 1.05 nm InAs structure.

For the 1.3 nm InAs structure (Figure 4-4) the second QDash-like PR line can be resolved at 0.93 eV, superimposed with the WL related transition at 0.97 eV (both marked by black arrows). This shows that for the highest QDashes, the localization energy becomes high enough to confine more states, absorption of whose is strong enough to be observed. For the samples with smaller QDashes, the higher energy QDash states could not be clearly resolved. To identify the origin of this transition, approximate 1D **k·p** calculations for nominal QDash geometry were performed. Full 8 band **k·p** calculations will be too time-consuming due to large QDash volume and as a result extremely large number of confined levels. Also there are a lot of assumptions to be made due to lack of full structural characterization (e.g. exact barrier/WL composition or its possible gradients) which decreases the accuracy of the results.

Calculations in the 1D **k·p** model are sufficient to relate the higher energy resonance to the transition between the lowest electron and light hole level (green bars in Figure 4-4). The height of the bars is proportional to the electron and hole wave function overlap which is smaller for light hole-related transition in agreement with the amplitude of the PR resonance.

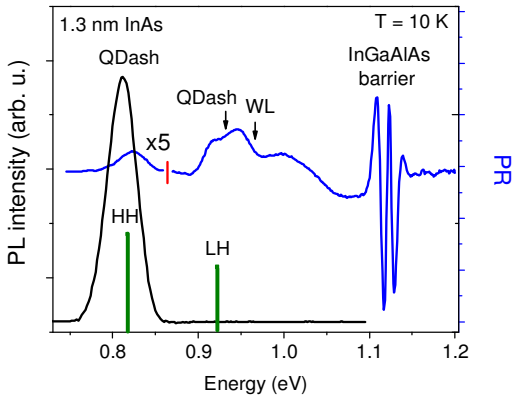

Figure 4-4. Low-temperature photoluminescence (black) and photoreflectance (blue) spectra for 1.3 nm InAs structure. Green bars denote calculated transition energies for heavy and light hole lowest states in 1D kp model.

Considering the other parts of the structure, the WL and the barrier related response can be observed for all the samples. The energies of respective resonances are summed up in the first part of Table 4-1.

Table 4-1. Determined experimentally energies of the QDash ground state, the WL and the barrier for various nominal InAs layer thickness, together with calculated energies of the QDash ground state (full 8 band k·p calculations) and the WL (1D model of a QW), with the energy of the barrier taken after PR measurements.

T = 10 K	Barrier (exp.)	WL (exp.)	QDash (exp.)	0.9 nm WL (1D calc.)	Ga/Al Intermixing	QDash (3D calc.)
0.70 nm InAs	1.214 eV	1.132 eV	0.998 eV	1.122 eV	12.0%	0.998 eV
1.05 nm InAs	1.150 eV	1.007 eV	0.869 eV	1.045 eV	8.5%	0.880 eV
1.30 nm InAs	1.120 eV	0.967 eV	0.813 eV	1.010 eV	7.0%	0.817 eV

The spectral position of both absorption bands shifts towards lower energy with increasing amount of deposited InAs material. In the case of the InGaAlAs barrier it is caused by unintentional barrier composition discrepancy decreasing the barrier energy gap, which for the nominal content ($In_{0.528}Ga_{0.234}Al_{0.238}As$), assuring lattice matched material, equals 1.088 eV at low temperature. Because of the combination of the compounds with large differences of energy gaps, the barrier band edge is very sensitive to even slight changes in

particular component content. The barrier-related resonance can additionally have a complex character, probably due to a slight difference between the top and the bottom barrier (Figure 4-2). The changes in the barrier band gap energy naturally influence the WL energy levels. This is one of the reasons for the observed WL resonance redshift. However, it cannot account for the whole change in the absorption energy, because the barrier energy gap changes by 94 meV between the extreme samples, whereas the WL energy shift is as large as 170 meV. To see how important is the shift of the barrier band edge on the WL ground state energy, 1D calculations within the 8 band **k·p** formalism, including strain and piezoelectric effects [And10, And13] were performed[2]. To imitate the WL, pure InAs QWs of 0.9 and 0.6 nm widths (values typical for WL in InAs/InP material system) were assumed. The ground state energy was calculated for the two extreme values of the barrier band gaps taken from the presented PR spectra (Table 4-2).

Table 4-2. Calculated (1D k p model) ground state energy of 0.9 and 0.6 nm thick InAs QW (columns) for various InGaAlAs barrier energy gap (rows) taken after PR results.

	InAs WL energy (1D 8 band **kp** calc.)	
barrier energy (exp.)	0.9 nm WL width	0.6 nm WL width
1.214 eV	1.043 eV	1.120 eV
1.120 eV	0.984 eV	1.045 eV

Calculated WL energy shifts equal 59 and 85 meV for the 0.9 and 0.6 nm QW, respectively, due to stronger sensitivity of a thinner QW to the barrier height. Other effects that can cause the WL shift are the intermixing degree or the QW width (critical thickness for the 3D island formation). The latter can be altered as a result of either the composition changes in the barrier which influence the strain, and/or the composition of the WL itself. This effect is rather negligible in the range of relevant WL compositions even for stronger strained In(Ga)As/GaAs material system [Leo94, Faf99, Sęk01, Pol06]. The intermixing (diffusion of Ga and Al atoms through the InAs/InGaAlAs interface) causes the deviation from the pure InAs and blueshifts the energy of the WL. As this effect does not have to be the same in all the structures, it can differentiate the WL energy. The experimentally observed tendency among different structures suggests stronger intermixing for the 0.7 nm InAs structure. To support the presented interpretation of PR measurements results, there were performed the 8

[2]Calculations provided by Dr. Janusz Andrzejewski (Institute of Physics, WRUT).

band **k·p** calculations in 3D [And10, And13] for the full structure (QDashes on WL)[1]. The QDash geometry was taken as nominal in the cross-section, with 100 nm in the elongation direction [1-10] for all structures, the WL thickness was assumed to be 0.9 nm and the barrier band edge was taken after PR measurements. However, the strain distribution changes caused by the altered composition of the InGaAlAs barrier were neglected (mainly because many different combinations of element content can lead to the same band edge energy and it cannot be modelled properly without additional structural data). Then the intermixing degree of the WL was chosen so to reproduce the experimentally observed QDash ground state energy, neglecting the possible different intermixing degree for QDashes due to the limited diffusion length of intermixing atoms. Under such assumptions the intermixing degree changes from 12 % down to 7 % for 0.7 nm to 1.3 nm InAs structures, respectively. For such an intermixing the ground state of the QW alone was again calculated in the 1D **k·p** model (Table 4-1) and it reproduces the experimentally observed tendency, but overestimates the WL energy compared to the experimentally observed values. This can be explained by the influence of the QDashes on the energy states in the WL. The energy levels calculated in the 3D approach applied to the full structure are generally redshifted. Furthermore, the barrier content changes decrease the lattice mismatch between the WL and the barrier, and so enable the formation of a thicker WL. The presented analysis shows that the barrier differs in composition within the sample series, which influences strongly the WL (its localization energy, thickness, as well as composition due to intermixing effects) but it seems not to have a large impact on the QDash structures themselves.

4.1.2. Thermal quenching of emission from quantum dash ensemble

In this chapter the temperature dependence of emission from the QDash ensemble is described. The goal is to identify the main PL quenching mechanism and see if it depends on the QDash size.

For the structure with the smallest QDashes and so the highest ground state energy, the emission cannot be observed up to room temperature due to the smallest localization energy with respect to the WL/barrier. The emission can be detected up to about 200 K (Figure 4-5). The analysis of the emission intensity changes with increasing temperature revealed two characteristic activation energies: 52 and 160 meV (Figure 4-6). The first one is determined with rather large uncertainty of 50 % (this is only the uncertainty of the fitting procedure and

the experimental accuracy is not included here) and the efficiency of the related process is 5 orders of magnitude lower than the higher energy one (Table 4-3).

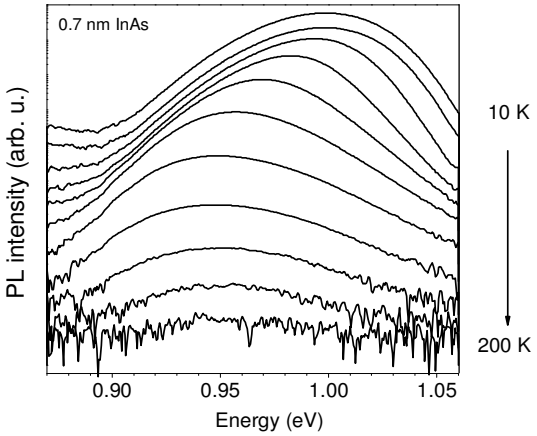

Figure 4-5. PL spectra of 0.7 nm InAs QDash structure for various temperatures in the range of (10 - 200) K.

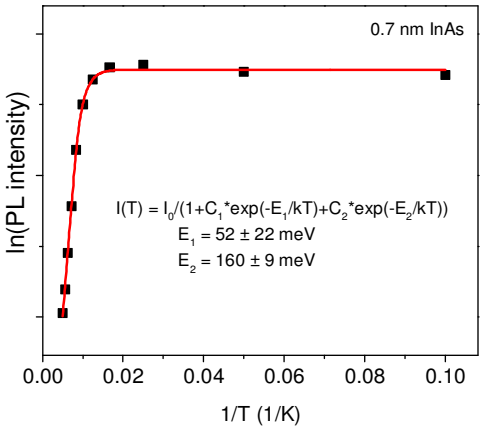

Figure 4-6. PL intensity dependence on temperature in a form of Arrhenius plot for 0.7 nm InAs QDash structure; symbols - experimental data (integrated intensity), solid line - fit according to Equation 2.3 with two activation energies E_1 and E_2.

Analogical study was conducted for the structures with lower emission energy. Emission from both low-energy structures is visible up to room temperature (Figure 4-7, Figure 4-8) and indeed covers the third telecommunication window at 1.55 μm (Figure 4-9).

The Arrhenius analysis (Figure 4-10, Figure 4-11) revealed two activation energies for each structure: 44 and 168 meV for the higher energy one and 37 and 157 meV for the lower energy one, respectively.

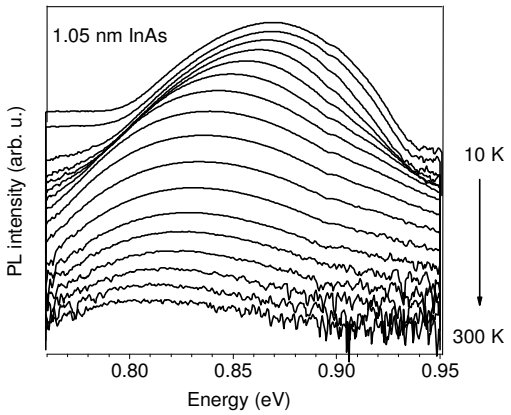

Figure 4-7. PL spectra of 1.05 nm InAs QDash structure for various temperatures in the range of (10 - 300) K.

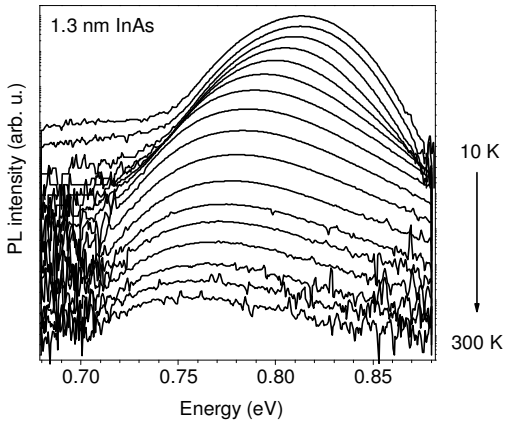

Figure 4-8. PL spectra of 1.3 nm InAs QDash structure for various temperatures in the range of (10 - 300) K.

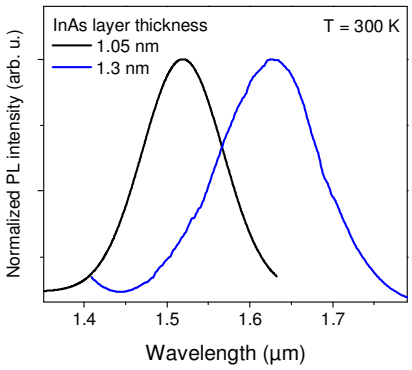

Figure 4-9. Room temperature PL spectra of 1.05 nm (red line) and 1.3 nm (black line) InAs QDash structure.

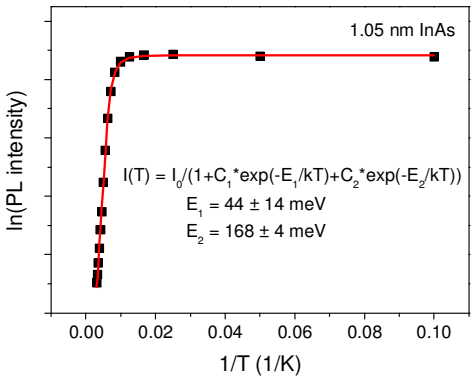

Figure 4-10. PL intensity dependence on temperature in a form of Arrhenius plot for 1.05 nm InAs QDash structure; symbols - experimental data (integrated intensity), solid line - fit according to Equation 2.3 with two activation energies E_1 and E_2.

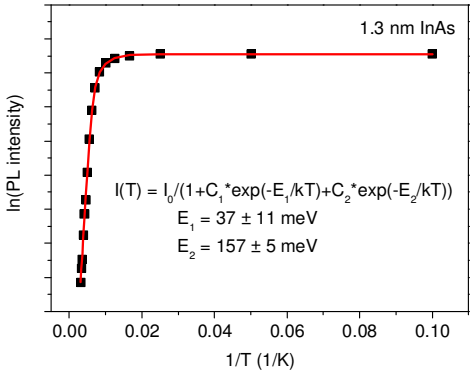

Figure 4-11. PL intensity dependence on temperature in a form of Arrhenius plot for 1.3 nm InAs QDash structure; symbols - experimental data (integrated intensity), solid line - fit according to Equation 2.3 with two activation energies E_1 and E_2.

Activation energies for all the investigated structures presented in Table 4-3 are almost identical within the fitting procedure accuracy (again the experimental accuracy is not included) and in all the cases the relative efficiency ratios of two quenching mechanisms equal 4 - 5 orders of magnitude.

To identify the quenching mechanisms related to obtained activation energies, the energy differences between the previously calculated (Section 4.1.1) first electron and heavy hole levels confined in QDashes and the WL-related levels as well as barrier band edge energy were determined (Table 4-4).

Table 4-3. Activation energies $E_{1,2}$ and parameters $C_{1,2}$ determined based on the Arrhenius fit with Equation 2.3 to experimental data for QDash structures with various InAs layer thickness.

InAs (nm)	E_1 (meV)	C_1	E_2 (meV)	C_2 (x 10^4)
0.7	52 ± 23	670 ± 1900	160 ± 9	6186 ± 3532
1.05	44 ± 14	42 ± 56	168 ± 4	120 ± 21
1.3	37 ± 11	22 ± 21	157 ± 5	23 ± 5

Schematic representation of respective energy scales for the QDashes of intermediate size (structure with 1.05 nm InAs layer thickness) is depicted in Figure 4-12 where the InAs band gap energy was neglected for clarity, because it is much bigger than any other energy in the system.

Table 4-4. Calculated (8 band kp model) electron and hole localization energies with respect to the WL and the barrier for structures with various InAs layer thickness together with activation energies determined from Arrhenius analysis.

	WL (calc.)		barrier (calc.)		activation energy (exp)	
InAs thickness	$E_{el,loc}$ (meV)	$E_{hh,loc}$ (meV)	$E_{el,loc}$ (meV)	$E_{hh,loc}$ (meV)	E_1 (meV)	E_2 (meV)
0.7 nm	94	36	153	85	52	160
1.05 nm	118	54	172	129	44	168
1.3 nm	137	64	170	151	37	157

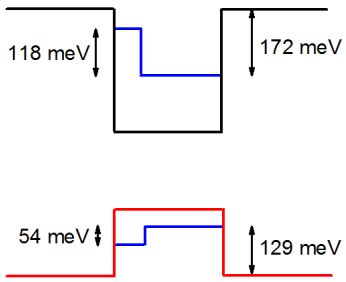

Figure 4-12. The scheme of the lowest energy levels position in the QDashes and the WL (blue solid line) with respect to the barrier based on the results of the 8 band kp calculations for 1.05 nm InAs QDash structure. Localization energies for both carrier types with respect to the WL and the barrier are marked by arrows. The InAs band gap energy was neglected for clarity.

The comparison between the experimentally obtained activation energies and the calculated ones points out at the holes escape to the WL and the electron escape directly to the barrier as the main PL quenching mechanisms. The first one, related to lower activation energy, is expected to be rather inefficient, in agreement with experimental results, because the carrier released to the WL can be easily re-captured and contribute to the emission of the QDash ensemble. In that sense the carrier is not really lost and does not lead to the decrease in emission intensity, but takes part in the WL-mediated carrier redistribution process. Very high surface density of investigated structures increases the probability of the re-capture process and so decreases the efficiency of the holes escape to the WL as a PL quenching mechanism. The tendency of activation energy changes within the structure series is not reproduced in the results of the calculations. This might be due to the fact that the WL states were calculated in 1D model for a QW without QDashes, but with relevant thickness and intermixing degree. Also the strain variation resulting from the changes in the barrier composition were not taken into account. Both can influence the energy levels position in the WL. The exact modelling of investigated structures is not possible due to limited structural data (e.g. barrier composition and exact WL thickness and intermixing degree). The goal of presented calculations is not to reproduce the experimental results exactly, but rather to show some tendencies and characteristic (relative) energy scales to support interpretation of PL measurements.

The second PL quenching process, i.e. electron escape directly to the barrier, has much higher efficiency, because once the carrier escapes to the barrier it is very unlikely that it will be re-captured. The activation energies observed in experiment for two low energy structures are

approx. 20 meV lower than the calculated ones. This might be a result of comparable localization energies of holes and electrons with respect to the barrier and suggest that both processes, hole and electron escape to the barrier, are important and contribute to the PL quenching. As has already been argued in Section 3.1.2, including additional activation energies in the Arrhenius analysis is not really reliable, especially if they are relatively close to each other, like in the case of electrons localization with respect to the WL and holes - to the barrier. Because of that, the second energy should be treated rather as an effective one for the carriers escape to the barrier. The non-monotonic character of the second activation energy changes among the structure series follows that of the electron localization energy with respect to the barrier, which implies that this process is the most efficient one mainly responsible for the PL quenching.

4.2. Spatial character of carrier confinement

In the following chapter the details of the confining potential are described. The crucial objective is to answer the question whether/to what extent the confining potential (and so the wave function extension) anisotropy follows the shape anisotropy. Also the issue of the homogeneity of the potential (especially in the elongation direction) is addressed. The interesting point is to conclude, if the investigated structures are in the strong or weak confinement regime. This enables to evaluate the relative importance of the quantum confinement effects and the Coulomb interactions. The polarization-resolved PL was used to probe the nanostructures shape asymmetry. To what extent it can be applied in the case of structures exhibiting high shape anisotropy is further discussed.

4.2.1. Quantum dot geometry impact on polarization

To get a deeper insight into the polarization properties of emission, at first some results of general theoretical considerations and next the modelling of the optical response of investigated structures, are presented. The influence of the in-plane and cross-sectional anisotropy is discussed separately, to enable proper interpretation of experimental data.

Below there is presented a theoretical approach proposed by Piotr Kaczmarkiewicz and Paweł Machnikowski, to account for the polarization degree in the case of elongated

nanostructures [Kac10]. The derivation of the qualitative formula describing the influence of in-plane dimensions and higher energy states occupation on the polarization is outlined. This result is further utilized to explain the high polarization degree of surface emission in the case of investigated QDashes, together with its spectral dependence.

It was shown [Kac10] that the crucial effect to account for the selective polarization properties of emission is the valence band mixing, enhanced by the shape anisotropy. It is enough to include the light hole admixture to the mainly heavy hole-like valence band ground state to construct the **k·p** method-based minimal model describing qualitatively the influence of the in-plane geometry on the polarization properties of emission. At first, the general description of the polarization degree is considered. The separation of the dipole moment operator into the bulk part and the envelope function overlap is performed. For a given initial electron spin only two non-vanishing in-plane components of the dipole moment contribute to the emission (one heavy hole and second light hole-like) and so only two bulk matrix element of the dipole moment operator need to be considered. Depending on the physical orientation of the nanostructures with respect to the crystallographic axes, the components of the interband dipole moment should be rewritten in a suitable coordinate frame. Taking into account that the emission intensity is proportional to the square of the interband dipole moment component, the anisotropy of the emission polarization was shown to be governed by the valence band mixing and dependent on the relative phase of the light- and heavy-hole contributions. Further assumptions need to be made to obtain semi-qualitative results, i.e. simplified confining potential (quantum box model) and mainly heavy hole character of the valence band ground state. Also the influence of the out-of plane dimension is neglected, i.e. only the lowest confined energy level in the structure growth direction is taken into account. It is well justified, because it is the direction of the strongest confinement and so the energy levels separation in this direction is much larger than in the other two. However, it has some indirect impact as it determines the light hole-heavy hole splitting influencing their mixing degree. The dominant contribution of the heavy hole to the valence band ground state can also be easily argued in the case of self-assembled compressively-strained nanostructures, in which the separation between the light and heavy hole levels is additionally increased by the shear strain component and the interband coupling elements are relatively small. Under these assumptions the light hole admixture to the valence band ground state can be treated perturbatively and can be expressed via the light hole-heavy hole energy separation and the respective element of Kane Hamiltonian coupling the light and heavy hole states under

considerations. For a given electron spin, admixture of only one type of the light hole states needs to be taken into account because only transitions yielding non-vanishing in-plane components are relevant. In the last step the details of single particle wave functions and confining potential are neglected, i.e. infinite potential barriers in 3D are assumed (quantum box model). Leading contribution to the emission of the transitions between electron and hole states with the same quantum numbers and the overlap integral between them equal to 1 is further assumed. All these allow deriving the analytical formula describing the in-plane geometry influence on the degree of linear polarization of the surface emission [Kac10]:

$$DOP = \frac{\hbar^2 \pi^2 \gamma_3}{m_0 \Delta E_{hh-lh}} \left(\frac{n_t^2}{W^2} - \frac{n_l^2}{L^2} \right) \qquad (4.1),$$

where the γ_3 is the Luttinger parameter, ΔE_{hh-lh} is a kind of effective light hole - heavy hole energy level separation (when interpreted in the single band language), W and L stand for width and length, respectively and $n_{t,l}$ numbers the states in the transversal and longitudinal directions, respectively. This simplified formula contains a lot of qualitative information. First of all, a sort of trivial one, i.e. the smaller the energy separation between the hole levels, the larger the valence subband mixing and, as a result, also higher DOP. Further, as far as the ground state emission is concerned, for structures with full in-plane rotational symmetry ($W = L$) the DOP equals zero and increases with increasing nanostructure length – structure anisotropy (expressed by lateral aspect ratio L/W). If the excited states contribution is included, the polarization degree should at first decrease as a result of increased occupation of higher energy states in the longitudinal direction (n_l larger than 1 in Equation (4.1)). These are occupied first as being less separated due to the weakest confinement in this direction. Then the higher energy states corresponding to the transversal direction of confinement are being occupied, which again increases the polarization degree (n_t in Equation (4.1.) increases). This shows that in the case of the polarization properties of emission not only the confining potential anisotropy, but also the occupation distribution matters.

To check the contribution of different states and their polarization to the emission of the QDash ensemble, the PL spectra for perpendicular linear polarization contributions coinciding with the QDash elongation and perpendicular in-plane directions were measured and the degree of polarization was resolved spectrally for the sample with 1.05 nm InAs (Figure 4-13). The directions of optical axes were carefully checked and their coincidence with the crystallographic directions was proven.

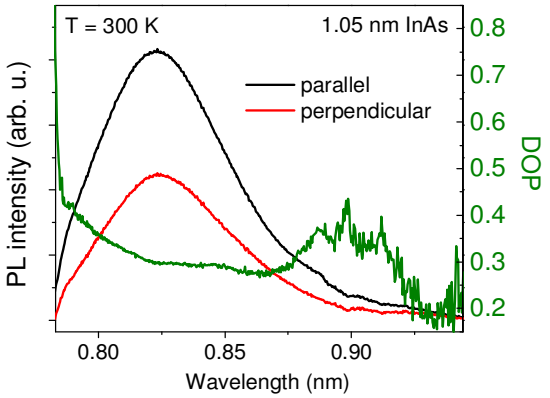

Figure 4-13. Room temperature PL spectra of 1.05 nm InAs QDash structure at two orthogonal linear polarizations (black solid line: parallel to the structure elongation, red solid line: perpendicular to the structure elongation) and the corresponding DOP (green solid line). The DOP fluctuations at 0.9 eV are related to the water vapour absorption in the area of weak PL signal.

The emission spectra polarized parallel to the elongation direction (red line) and perpendicular one (black line) show the supremacy of the polarization component corresponding to the QDash elongation direction. The DOP value for the emission band maximum is about 0.3, in agreement with the expected increased DOP for structures with strong anisotropy. It also correlates well with the measurements on SQDashes in which DOP in the range of 0.2 up to 0.4 were obtained. The large variations in the observed DOP values can be accounted for by the local strain-induced valence band mixing effects, which are averaged out in the case of the effective response of the large number of nanostructures. Back to the spectral polarization degree dependence determined from the ensemble emission, the increase in the DOP towards lower energies is caused by the drop of the sensitivity of the InGaAs multichannel detector. In the case of high-energy tail of the emission, the subsequent occupation of higher energy states according to Equation (4.1) can account for the observed DOP changes. At first, the higher energy states in the longitudinal direction are contributing to the emission due to the smaller inter-level separation (because of a larger size in the elongation direction). This leads to the decrease of the polarization degree. For even higher energies, also the states in the transversal direction become occupied. The emission from these states increases the polarization degree, which results in a characteristic maximum in spectral dependence of the DOP at a high-energy part of the emission band.

To model quantitatively the polarization degree in the case of investigated structures the full 8-band **k·p** calculations were performed by Janusz Andrzejewski (Institute of Physics,

WRUT). The model includes three-dimensional strain distribution and piezoelectric effects up to the second order [And10, And13]. The calculations of polarization degree were performed for realistic QDash geometry, with cross-sectional size typical for a structure emitting at 1.55 µm (3.5 x 20 nm^2) as a function of QDash length (LAR) - black squares in Figure 4-14. The polarization degree increases abruptly if the in-plane rotational shape symmetry is broken (lateral aspect ratio in the range of 1 - 2), but further increase in the nanostructure length does not change it much and the dependence finally saturates on the level of about 0.3 for lateral aspect ratio higher than 4. This corresponds to the quantum dash length on the order of 80 nm, which is smaller than the typical values for the investigated structures and therefore the DOP of about 0.3 is expected for the dashes under study. The red line in Figure 4-14 is the fit with Equation (3.1), which has the same mathematical character as Equation (4.1). This shows that they both correspond qualitatively to the same mathematical function, which allows extending further the use of the simplified model in the first approximation considerations.

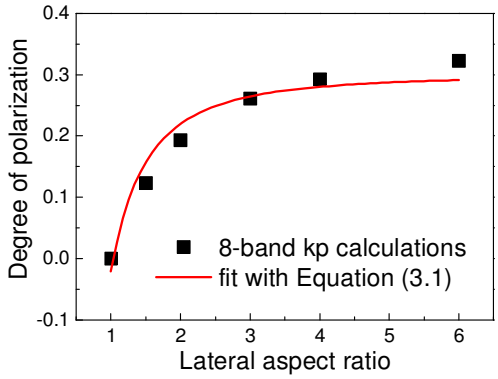

Figure 4-14. Calculated DOP of surface emission (squared symbols) vs. the lateral aspect ratio of a QDash of size 3.5 × 20 nm with the triangular cross-section (length changed from 20 up to 120 nm). The solid line is a fit according to Equation (3.1).

So far, the out-of plane dimension has been neglected in the considerations, but as this is expected to have also a significant influence on the polarization properties of the emission I have extended the model described above [Kac10] into the influence of the QDash height on the DOP [Mus12]. This should change the valence band mixing because this is affecting the confinement strongly and hence the energy separation between the valence band sublevels (the light hole - heavy hole energy separation). In the simplest approximation this separation can be modelled by an inversed parabolic function which reflects the dependence of energy level position on the size of the rectangular infinite potential well. However, this simplification is insufficient, because it leads to a quadratic increase of the polarization degree

with nanostructure height, whereas the DOP, according to its definition (Equation (1.11)), cannot exceed 1. For the finite potential well this relation has approximately a parabolic character, which results in the following dependence of the DOP on the nanostructure height H:

$$DOP \sim \frac{1}{aH^2 - bH + c}\left(\frac{1}{W^2} - \frac{1}{L^2}\right) \qquad (4.2),$$

where a, b, c parameters do not have any direct physical meaning but they just describe the energy level separation dependence on the potential well width (in fact they describe the shape of the confining potential). It has to be noted that Equation (4.1) was derived with the assumption that the out-of plane confinement is strong. This might not be relevant for significantly increased QD size in the growth direction, so it is not straightforward that it can be utilized to examine the DOP as a function of the QD height. To evaluate the usefulness of this formula additional polarization-resolved experimental studies were performed. There were realized on two sets of reference samples which are appropriate for this test as they cover the wide range of nanoobject heights from 2 nm up to 16 nm. Both sets are based on InP substrate and strongly elongated. However, they differ slightly in the nanostructure material and the details of the cross-sectional geometry (and so confining potential). The first series is a set of flat (nanostructure height in the range of 2 - 4 nm) InAs QDashes with triangular cross-section [Sau05]. The second one are formed of InGaAs and exhibit rectangular cross-section and strongly enhanced nanostructure height (up to 16 nm) and because of that are referred to as columnar QDashes. These structures are used here only for reference and are not the subject of presented thesis. The DOP of the surface emission determined for these structures is plotted as a function of QDash height in Figure 4-15 (blue symbols). The polarization-resolved PL was measured at excitation conditions corresponding to the occupation of the system limited to the QDash ground state.

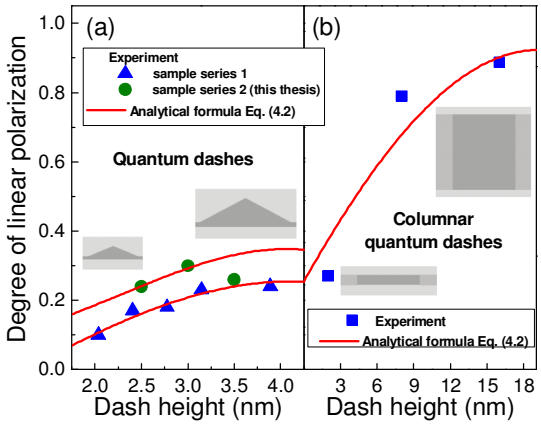

Figure 4-15. DOP (experiment) for (a) standard QDashes (green circles - series investigated in presented thesis, blue triangles - reference series) and (b) columnar QDashes versus their height (blue squares); the solid lines show a theoretical dependence according to Equation (4.2). The respective shapes of the dashes in the cross-section deduced from previous structural studies on similar structures [Sau05, Rud06-1, Rei07, Hei08, Pod08] are schematically shown for reference.

The red line in Figure 4-15 is the fit to experimental data with Equation (4.2) assuming anisotropic in-plane geometry with constant lateral aspect ratio. Different sets of fitting parameters (a, b, c) were used for the two groups of nanostructures due to differences in the details of confining potential. The experimentally obtained tendency is well reproduced by the simplified analytical formula. The important conclusions from the presented study are that the increased nanostructure height enhances the valence band mixing and so the DOP of the surface emission. Moreover, the high LAR is not sufficient to reach the full linear polarization of the surface emission, but the engineering of the nanostructure size in the growth direction is indispensable. In the case of very high QDashes (so called columnar QDashes), a record value of the DOP for any epitaxial nanostructure, equal to 0.9, was observed.

The results obtained on the reference samples enable to evaluate proposed approach and these structures will not be further investigated or discussed. The presented considerations bring an important insight into the expectations concerning the polarization properties of the emission in the case of the structures of interest. First of all, it seems that the LAR is already so high (exceeding 5) that the DOP is in the saturation limit. Differences between the samples within the series caused by the in-plane geometry can be neglected in the first approximation. Based on the **k·p** modelling, the DOP value should be in the range of 0.3. The driving factor that can differentiate the exact DOP values for the three investigated structures is actually the size in the growth direction. It should lead to the increasing DOP value with the increasing QDash height (increasing InAs layer thickness). However, the

differences are not expected to be large as all the structures are rather flat and the height changes in a narrow range of approximately 1 nm. Moreover, the polarization degree dependence on the QDash height also tends to saturate, so depending on the details of the confining potential the actual difference might not be well pronounced. Below those expectations are confronted with experimental results of polarization-resolved PL of the Qdash ensemble.

Low temperature polarization-resolved spectra at high excitation conditions for the whole structure series are presented in Figure 4-16. For all the samples the DOP at the emission maximum is high. Surprisingly, the trend among the series is not monotonic, and does not follow the expected increase in the polarization degree with the increasing QDash height (InAs layer thickness) - green circles in Figure 4-15 represent the outcome of the experiment and the red solid line is the fit with Equation (4.2). The quantitative differences between the DOP dependence on the QDash height for reference series (blue triangles in Figure 4-15) and the structures of interest point out that there are some changes in the details of the confining potential shape for these two sets of structures. The polarization degree is maximal (30 %) for the structure with intermediate height of QDashes (1.05 nm InAs) and slightly lower for the other structures (24 % and 26 % for 0.7 nm and 1.3 nm InAs structures, respectively). One of the possible explanations is related to the excitation power conditions, i.e. the same excitation power density translates differently into the occupation of states in individual QDashes, depending on the QDash surface density. For the structure with the lowest quantum dash surface density (0.7 nm InAs), the average occupation of a single nanostructure (average number of excitons per quantum dash) at a given excitation power density is the highest, and so the higher energy states contribute stronger to the emission compared to higher density structures.

Because of that, the changes of the DOP at the maximum of emission can rather reflect the varying higher energy states contribution and not the QDash height. Due to the opposed influence of higher energy states in longitudinal and transverse directions on the polarization degree of emission, the changes of the DOP among the structure series, differing in both quantum dash height and nanostructures surface density, are not so easy to predict. Therefore, in the next chapter the DOP dependence on excitation power is examined in details to verify if the different contribution of the higher energy states can account for the observed trend in the high excitation polarization degree for the different QDash structures. Results for the low

excitation should reflect the DOP of the ground state and give the information about the QDash height influence on the polarization properties of emission.

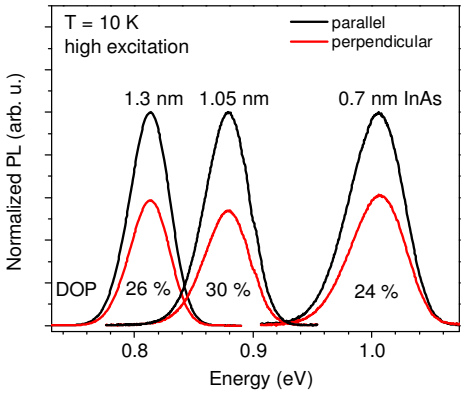

Figure 4-16. PL spectra from QDash structure with 1.3 nm, 1.05 nm, and 0.7 nm InAs measured for two perpendicular linear polarizations, along (black solid line) and perpendicular (red solid line) to the dash elongation axis.

4.2.2. Power and temperature-dependent polarization of emission - carrier trapping within the quantum dash structure

The polarization-resolved spectra at different excitation conditions at low temperature for all the structures in the series were measured (Figure 4-17). The tendency is similar for all the QDash samples, i.e. the lowest DOP corresponds to the lowest excitation conditions and increases with increasing excitation power from a few percent up to 24 - 30 % observed previously for high excitation. The amplitude of the DOP changes is rather large to be accounted for by the subsequent higher energy states occupation and does not match the values extracted from the spectral analysis of the DOP for the 1.05 nm InAs sample (Figure 4-13). Even more importantly, the low excitation DOP value is too low taking into account the strong in-plane anisotropy of the confining potential. The experimentally observed values of the DOP in the range of 0.04 - 0.14 correspond to the LAR varying from 1.1 to 1.4 (Figure 4-14) and so almost symmetric nanostructures. This is rather unrealistic in view of the structural data [Sau05].

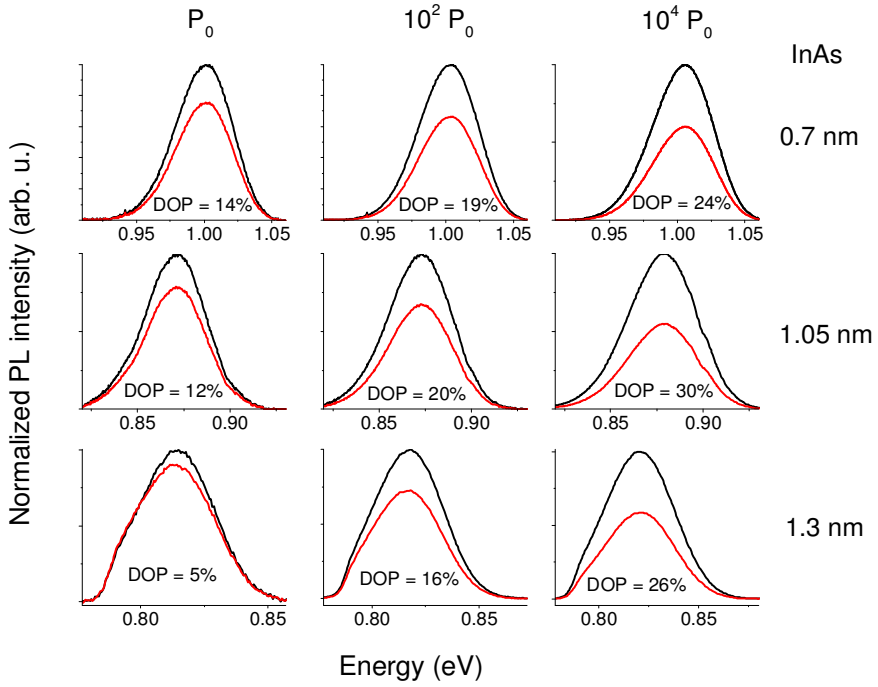

Figure 4-17.Polarization-resolved PL spectra (polarization along QDash elongation - black solid line, polarization perpendicular - red solid line) measured for QDash structures with various InAs thickness layer (rows) at various excitation conditions (columns).

The complete power-dependent series for all the investigated structures are presented in Figure 4-18. For the structure with 0.7 nm InAs nominal layer thickness the linear polarization degree at first increases with the excitation power, then reaches the maximal value of 0.24 and after that slightly decreases. This behaviour is qualitatively the same for all structures, but differs in the absolute values of the DOP. Also, the maximum value of the DOP occurs at higher excitation power for samples with the nominally thicker InAs layer, in agreement with the increasing nanostructure surface density.

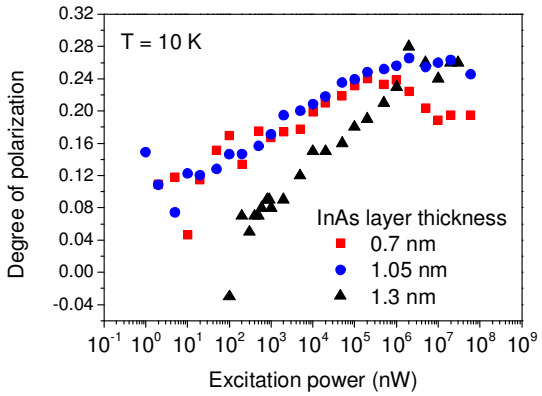

Figure 4-18. DOP dependence on excitation power density for QDash structures with various InAs layer thickness.

The effect that can account for the observed DOP behaviour is the existence of two types of states exhibiting substantially different symmetry, i.e. low-energy almost symmetric ones and more anisotropic of higher energy. Contribution of these two types of states to the overall emission changes with the occupation distribution. One possibility is that at each sample there are actually two families of nanostructures - one more QD-like, with almost full in-plane rotational symmetry and of deeper confinement potential and actual strongly elongated QDashes, emitting at higher energies. The co-existence of nanostructures with different geometries In the case of InAs/InP structures is possible, but seems rather unlikely here, taking into account the morphological study of the structures grown in analogical conditions [Sau05] and the previous optical study, i.e. no fingerprint of a second QD family in the absorption or emission [Rud06-1]. If the low DOP was related to shorter, more symmetric dashes, they would contribute to the ensemble emission at larger energies, which is not the case here.

Another explanation can be the existence of local confining potential fluctuations within the individual QDash, acting as trapping centres for the carriers (a sort of dot in a dash structure). The potential fluctuations are rather more symmetric than the dashes themselves. Furthermore, they are naturally the lowest energy states of the system but they can be easily filled due to a rather low density of states (mainly due to a low number of confined levels), enabling the emission from higher energy states, whose wave functions can potentially be extended over the entire QDash volume. In this scenario no spectral dependence of the DOP related to those states is expected, as they can exist in all the QDashes and so contribute to the emission at arbitrary energy. In that case the absolute DOP value will change with the

excitation power, but the spectral dependence within the QDash ensemble will be in agreement with experimental observations. This interpretation is also supported by the morphology of the sample surface that exhibits strong shape irregularities of individual nanostructures in a form of width fluctuations and occasionally also QDash bending, which together with the composition fluctuations (most probably due to the well-known indium tendency to segregate) can be the underlying reason of the confining potential fluctuations.

To confirm this scenario an alternative method of changing the occupation distribution within an individual QDash, i.e. temperature, was tested experimentally. Its influence on the DOP at different excitation conditions was examined in details (Figure 4-19, Figure 4-20, Figure 4-21, Figure 4-22). The advantage of this experiment is that it is easier to model it due to the Boltzmann carrier distribution that can be assumed in the first approximation. On the contrary, in the power-dependent PL the overall system occupation is much higher (it increases with the excitation power density) and because of that many body correlations have to be included in the model. The temperature-dependent results of the DOP at the low excitation conditions are in agreement with the previous power-dependent experiments, proving that the DOP change is a fingerprint of the delocalization process due to the changes in the occupation distribution in favour of the higher energy, less symmetric QDash-like states (Figure 4-19). At low temperature and low excitation conditions the emission from the trapped states dominates and as a result the observed DOP is rather low, in a few percent range. As for the power-dependent experiments, the minimum in the DOP is observed for slightly increased temperature which can be related to the carrier redistribution effects within the QD ensemble.

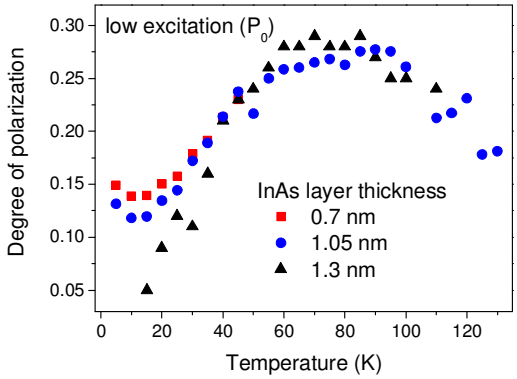

Figure 4-19. DOP dependence on temperature at low excitation conditions for QDash structures with various InAs layer thickness.

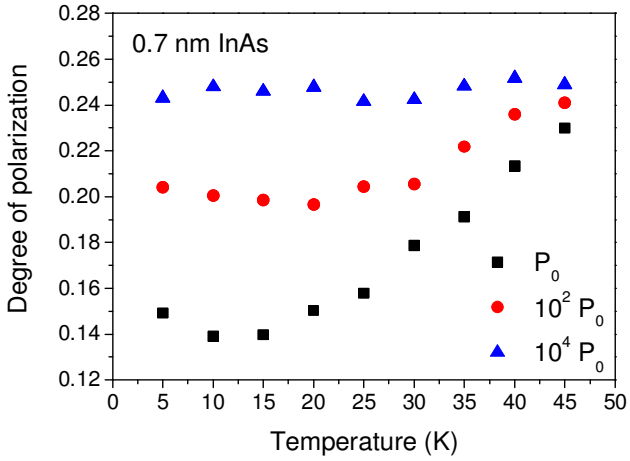

Figure 4-20. DOP dependence on temperature at different excitation conditions for QDash structure with 0.7 nm InAs.

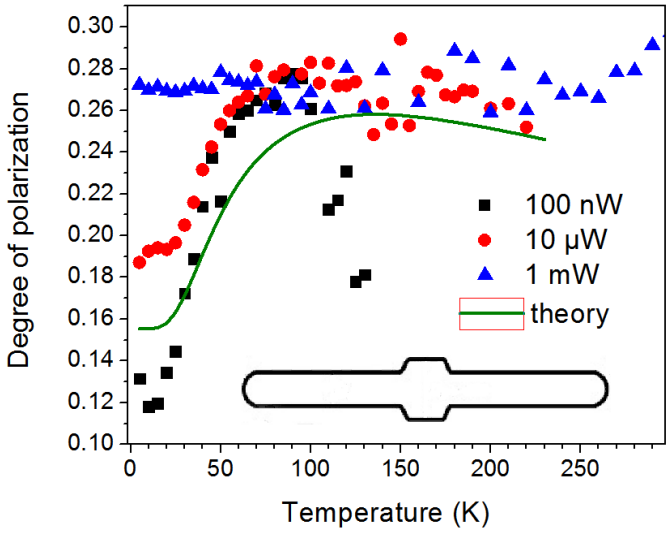

Figure 4-21. DOP dependence on temperature at different excitation conditions for QDash structure with 1.05 nm InAs together with the outcome of the calculations. The inset shows the schematic top view of the in-plane geometry of the QDash with the cross-sectional size fluctuation used in the modelling.

The trapping centres do not have to accompany each QDash, but are randomly distributed among the QDash ensemble. At the lowest temperature some of the carriers can be trapped in QDashes with rather homogeneous potential without significant fluctuations. This is caused by the limited carrier diffusion length which is greatly enhanced by the temperature. The maximum value of the DOP corresponds to the lowest QDash-like state emission and further decrease in the DOP reflects the higher energy states contribution, as described by Equation

(4.1). For the lowest excitation power this decrease is rather strong, but the experimental accuracy is in this case the lowest due to a low signal to noise ratio (see error bars in Figure 4-21).

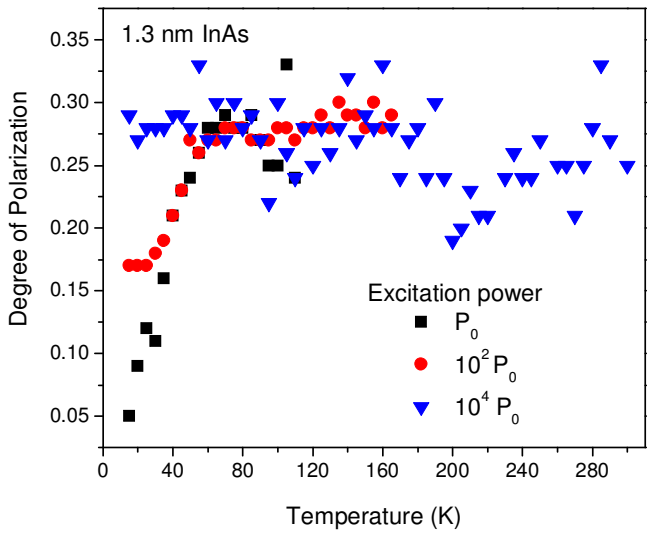

Figure 4-22. DOP dependence on temperature at different excitation conditions for QDash structure with 1.3 nm InAs.

This dependence was modelled theoretically within the **k·p** formalism[3], assuming a width fluctuation within the 20 x 4.5 x 150 nm^3 quantum dash [Mus12-1]. In the calculations, the excitonic effects were included by the configuration interaction method, but the actual 3D strain distribution was only partially accounted indirectly by the strained band offsets values. In the cross section directions the parabolic potential was assumed and in the elongation direction it was variationally calculated. This approach enables to reproduce all the experimental features (green line in Figure 4-21), supporting the presented interpretation of the experimental data and the existence of the additional carrier trapping centres within the individual nanostructures. For the higher excitation power the DOP also increases with temperature up to the value characteristic for the extended ground state, but the low-temperature DOP is significantly higher than in the previous case, reflecting a non negligible contribution of QDash-like states to the emission, enhanced by the excitation power due to the state filling effect. That is the signature of the low density of states of the localized centres which can have two primary reasons, i.e. the lower trapping centres density in comparison to

[3] Calculations performed by Piotr Kaczmarkiewicz and Paweł Machnikowski (Institute of Physics, WRUT)

the QDash surface density and a small number of states confined in the potential fluctuation minima. Concerning the latter, the temperature in which the maximum DOP is reached can be treated as a measure of the average depth of the fluctuations, because the release of carriers to the QDash volume is a thermally activated process. The estimation of this localization energy gives the upper limit of 9 meV. The depth of the trapping potential seems similar for all the QDash structures. However, the minimal polarization degree (observed at low temperatures and excitation conditions) differs by a few percent for the 1.3 nm InAs structure. The lowest value of the DOP for the highest QDashes can be related to the increased symmetry of the wave function. As a result, the contribution of more symmetric states into the overall emission from QDash ensemble at low excitation power is increased. The increased symmetry of the wave function localized on the potential fluctuation is also possible and can be caused by the differences in QDashes cross-sectional dimensions. Namely, the wave function extension in the nanostructure elongation direction is closer to the QDash width for higher QDash structures. The former can be the key to understanding the lower maximum value of the DOP for the 1.3 nm InAs structure in comparison to the 1.05 nm InAs one. Although the maximum DOP value corresponds to the emission from the QDash-like states the existence of carrier trapping centres influences the extension of the wave function of these higher energy states [Mus12-1, Kac12].

To emphasize the equivalence of the power- and temperature-dependent measurements, the DOP results for varying excitation power at 5 K and as a function of temperature for low excitation conditions, are compared for each of the structures (Figure 4-23, Figure 4-24, Figure 4-25). Both factors, i.e. temperature and excitation power change the occupation distribution in favour of higher energy states, but in a slightly different way. The temperature does not change the number of carriers within the system but rather their distribution, as far as the possibility of the thermal escape of the carriers from the quantum structure is neglected. At a given temperature the states occupation can be described by the Boltzmann distribution, whose dependence on temperature has an exponential character. In the case of the increased excitation power, higher energy states are occupied due to the state filling effect, as the overall number of carriers in the system is increased. This is the reason of different horizontal scales in Figure 4-23, Figure 4-24 and Figure 4-25 as the occupation of excited states scales with the excitation power according to the power law, while the dependence on the temperature is exponential. With these restrictions the DOP dependence on

both factors is similar, with the same characteristic maximal value and the amplitude of the DOP changes.

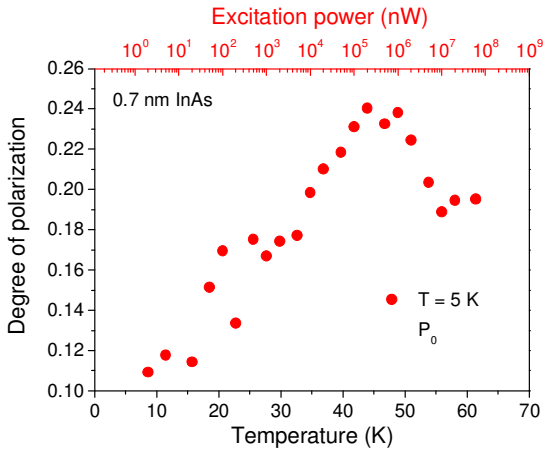

Figure 4-23. The comparison between the temperature (bottom horizontal axis, black squares) and excitation-power (top horizontal axis - logarithmic scale, red circles,) dependence of emission DOP for 0.7 nm InAs QDash structure.

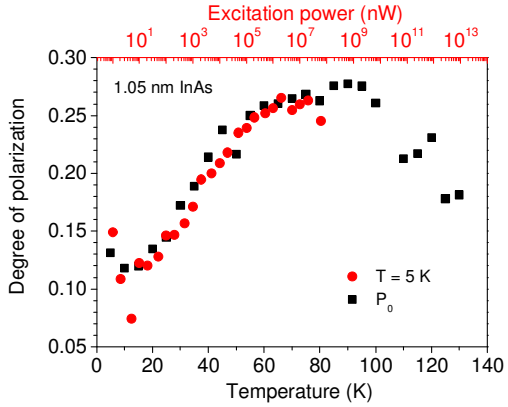

Figure 4-24. The comparison between the temperature (bottom horizontal axis, black squares) and excitation-power (top horizontal axis - logarithmic, red circles) dependence of emission DOP for 1.05 nm InAs QDash structure.

Polarization-resolved measurements enabled to interpret the non-monotonic dependence of the DOP for QDashes differing in the nanostructure height as caused by the existence of the trapping centres and changes in their characteristics among the structure series. This two stage character of confining potential needs to be taken into account at the design stage of single nanostructure-based devices. The localized character of the ground state of large volume elongated nanostructures influences the polarization properties of emission, and so the FSS, but also the relaxation processes and the oscillator strength of excitonic

transitions, thus having an impact on the strength of single exciton coupling to the cavity photons.

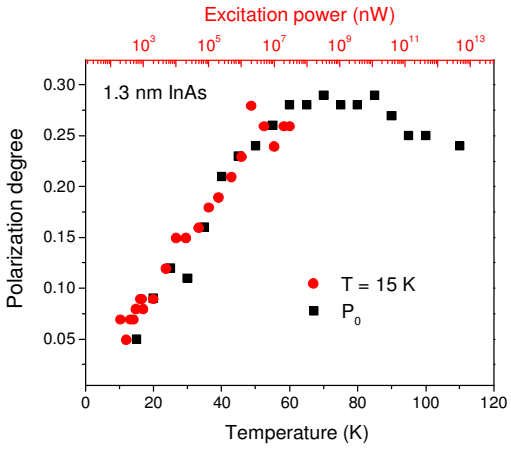

Figure 4-25. The comparison between the temperature (bottom horizontal axis, black squares) and excitation-power (top horizontal axis - logarithmic scale, red circles) dependence of emission DOP for 1.3 nm InAs QDash structure.

The performed experimental study on the polarization properties of the emission, supported by the theoretical modelling, proves that the measurements of polarization degree dependence on temperature and/or excitation power can be a good experimental method to verify the existence of potential fluctuations in the case of strongly elongated nanostructures. The necessary condition is the symmetry change between the localized ground state and the higher energy states. It is a relatively easy non-destructive method that can be applied in the case of embedded nanostructures and is valid also in the case when the dimensionality of the system does not change (like in the case of dot in a dash structure), in contrary to other methods, e.g., spatial mapping of emission, microscopy-based techniques or time-resolved measurements [Gui03].

4.3. Microphotoluminescence study

The single quantum object spectroscopy on InAs/InGaAlAs/InP QDashes is rather challenging due to their naturally high surface density reaching $10^{11}/cm^2$, which is beneficial for standard optoelectronic applications due to absorption enhancement, but needs to be significantly lowered to enable SQDash-based devices. Because of that the sample surface patterning is indispensable to resolve the SQDash emission. In the case of 2.2 μm x 1.1 μm

mesa, the emission has an ensemble-like character and single emission lines cannot be clearly resolved due to thousands of QDashes being excited simultaneously and tens of them coinciding at the ground states energy (Figure 4-26). For the smallest available mesa sizes of 650 nm x 325 nm the optical spectra already enable SQDash emission observation, but very often at the boarders of the QDash ensemble size distribution.

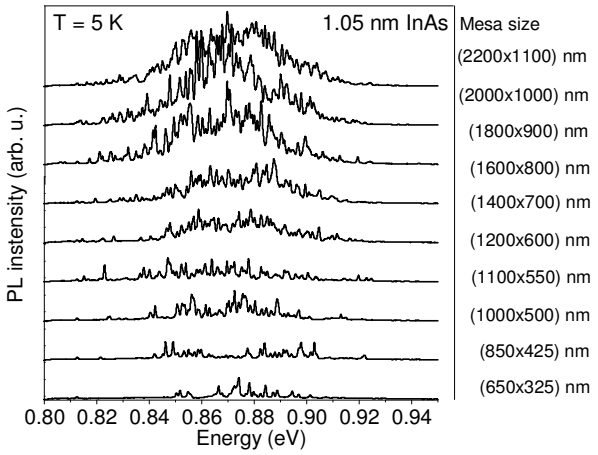

Figure 4-26. The low-temperature microPL spectra of 1.05 nm InAs QDash structure for various mesa sizes.

Further SQDash spectroscopy experiments were performed on those mesas, as the width of the single emission lines is not significantly altered by the decreased mesa size. In other words, the population of QDashes in the mesa is still high enough that most of them are not influenced significantly by the effects related to the mesa sidewalls. However, even for the smallest mesas, the optical spectra are rather dense and the results of microPL measurements need to be analysed very carefully for proper data interpretation.

4.3.1. Excitonic complexes

As the optical spectra with SQDash emission lines are rather dense, the identification of individual excitonic complexes, in particular confined in the same QDash, is not trivial without external fields and/or correlation measurements. Because of that the discussion of the excitonic complexes is limited to the neutral exciton and biexciton. At first the fine structure splitting of the exciton is discussed and then the analysis of the biexciton-exciton cascade is

performed. The origin of the single emission lines is confirmed utilizing the emission intensity dependence on the excitation power, derived from the rate equation model.

The polarization-resolved study in the SQDash regime were performed to determine the fine structure splitting of the neutral exciton. Determined FSS values do not differ much in between the investigated structures. Also no correlation between the emission energy of the exciton and its FSS was observed (Figure 4-27.). Lack of the interdependence of the exciton emission energy and the energy difference between the two bright excitonic states can be related to the existence of the localized centres within the QDash whose size distribution is rather random and not related to the internal characteristics of the QDashes.

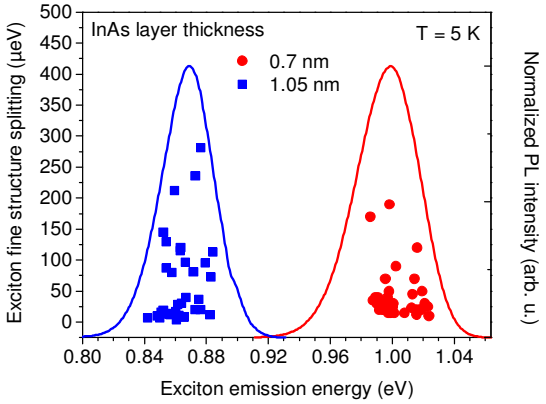

Figure 4-27. Spectral dependence of the exciton FSS (symbols) for InAs/InGaAlAs/InP QDash structures with respective low-temperature PL spectra (solid lines).

Considering the fine structure splitting values and their distribution, most of the cases exhibit rather low FSS value in the range of 0 - 50 μeV (within the experimental accuracy actually). Much larger values from 50 up to 150 μeV are less common and also some exceptionally large values between 200 - 300 μeV were observed. These large values of the FSS can be a manifestation of the importance of the piezoelectric effects which enhance the anisotropy of the exchange interaction and becomes dominant for large structures, being mostly related to the physical nanoobject volume. The influence of those effects is for most cases weakened due to the additional carrier trapping within the QDash, lowering both, the effective volume over which the wave function is extended, and its effective anisotropy, leading to rather small FSS values. On the contrary, large FSS values are probably related to the QDash structures with more homogeneous confining potential. This value, inherent to QDashes geometry, seems to be lower for the flattest and slightly less elongated structures, in agreement with the joint impact of the elongation and the size.

In Figure 4-28 a microPL spectrum of the structure with the largest QDashes (1.3 nm InAs) at relatively low excitation power is shown. Single emission lines at 1.55 μm (0.8 eV) are clearly visible, proving the relevance of the investigated structures for fibre-based data transmission and other nanophotonic telecommunication applications. The large number of single emission lines in the spectrum reflects the high QDash surface density. In that case the unambiguous identification of lines related to the emission from the same nanostructure is rather complicated. Due to the biexciton binding energies in the range of single 1 meV, the related lines might not be the neighbouring ones.

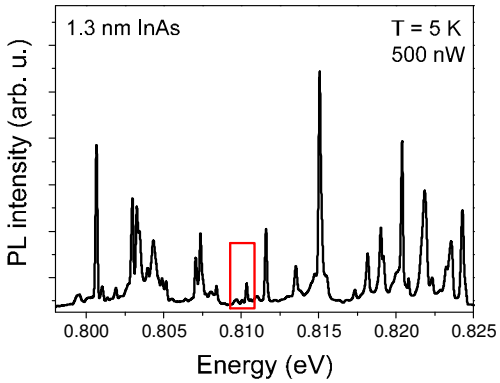

Figure 4-28. The low-temperature microPL spectrum of 1.3 nm InAs QDash structure at low excitation power (500 nW); emission lines analysed further marked with red frame.

In Figure 4-29 a very narrow range of the emission (red frame in Figure 4-28) is presented. MicroPL spectra for different excitation powers enable observation of the relative intensity changes of the emission lines within this part of the spectra. The lines whose intensity changes are qualitatively in agreement with the expectations for the excitonic and biexcitonic emission are marked on the spectra.

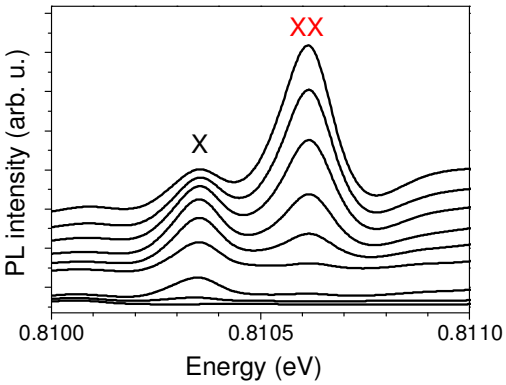

Figure 4-29. The low-temperature microPL spectra of 1.3 nm InAs QDash structure for various excitation power densities.

Detailed analysis of the particular emission lines intensity as a function of excitation power (symbols in Figure 4-30) confirms the origin of the observed emission, but cannot prove the assignment of the exciton and biexciton coming from the same cascade. To solve this problem the rate equation model was used and the experimental data were fitted with theoretical dependences (solid lines in Figure 4-30).

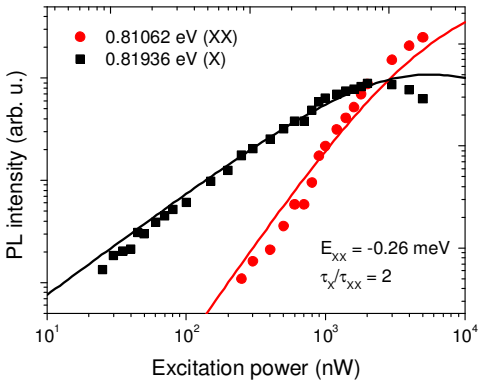

Figure 4-30. Emission intensity vs excitation power density analysis for 1.3 nm InAs QDash structure; symbols - experimental data and solid lines - fit with rate equation model solutions. The spectral lines are labelled with their peak energy.

The best fit to the experimental data was obtained for $\frac{\tau_X}{\tau_{XX}}$ value equal to 2, which is a fingerprint of the strong confinement regime and suggests slow internal exciton states dynamics [Nar06]. This shows that the confinement regime is determined by the cross-sectional dimensions together with a rather large exciton Bohr radius for bulk InAs equal to 34 nm. Taking that into consideration, this parameter should not differ much, either for the

exciton confined within the QDash, or trapped by the confining potential fluctuation minimum. Once the biexciton-exciton cascade elements are identified, the biexciton binding energy can be obtained. For the presented case it is negative, on the order of -0.26 meV. The biexciton binding energy can become negative for very small nanoobjects, if the quantum confinement dominates over the Coulomb interaction (which can be the case for the smallest QDashes or carriers trapped in potential fluctuation minima) or in the case of large nanostructures, if the piezoelectric effects dominate over the Coulomb attraction. The piezoelectric effect is stronger for larger QDs and as a result the Coulomb attraction and so the biexciton binding energy is reduced [Cha06, Cha06-1]. This is a much more likely scenario in the case of the investigated structures with large physical volume, but it will be clearer at the stage when the results from the whole sample series will be compared. For most of the cases the biexciton binding energy is in the range from -1 meV up to 1 meV (Figure 4-35).

Analogical study was performed for the two remaining QDash structures. All the analysed exciton-biexciton pairs among the series are summed up in Figure 4-35, together with the spectral dependence of the determined biexciton binding energy and the QDash ensemble emission spectra. An exemplary result for 1.05 nm InAs structure is presented in Figure 4-31. The determined biexciton binding energy equals 0.6 meV and is typical for QDashes emitting in this spectral range [Cha06, Cha06-1]. The exciton to biexciton lifetime ratio obtained from the fitting procedure equals 2, like for the previous QDash structure.

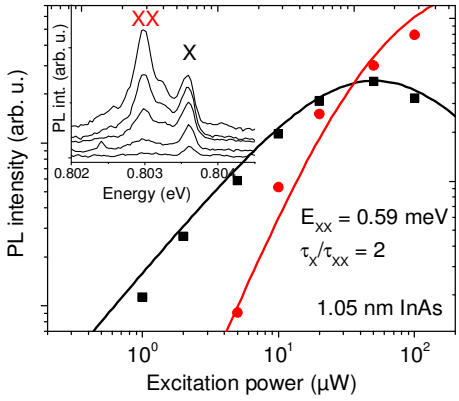

Figure 4-31. Emission intensity vs excitation power density analysis for 1.05 nm InAs QDash structure; symbols - experimental data and solid lines - fit with rate equation model solutions. The inset - microPL spectra for various excitation power densities.

For this structure the biexciton binding energies vary in the range of -0.5 up to 1.5 meV (Figure 4-35), with similar variation as in the case of previous sample, but with slightly higher

mean value in agreement with the explanation on the trade-off between the piezoelectric effects and the Coulomb attraction.

For the smallest QDashes the biexciton binding energy varies strongly and both relatively large biexciton binding energies up to 3.5 meV (Figure 4-33, Figure 4-35) as well as negative values (Figure 4-34) can be observed. For both the cases the high excitation part of the emission intensity dependence on the excitation power, i.e. strong decrease of the biexciton as well as exciton emission, is a fingerprint of the influence of higher energy states. This is not surprising in the case of QDashes due to the dense optical spectra with rather close inter-level spacing [Kac12, Mus12-1, Mar13]. For the case presented in Figure 4-34 the best fit to the experimental data was obtained for exciton and biexciton lifetime ratio equal to 4, which is in agreement with strong confinement regime argued previously, but suggests rather fast spin flip kinetics between the exciton fine structure sub-levels [Nar06].

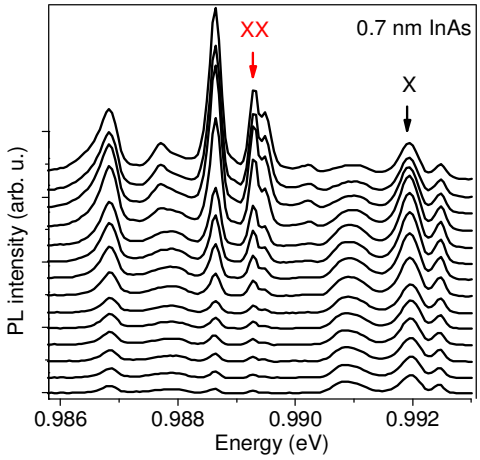

Figure 4-32. The low-temperature microPL spectra of 0.7 nm InAs QDash structure for various excitation power densities.

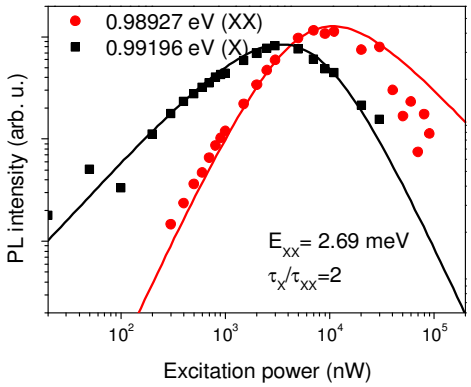

Figure 4-33. Emission intensity vs excitation power density analysis for 0.7 nm InAs QDash structure; symbols - experimental data and solid lines - fit with rate equation model solutions.

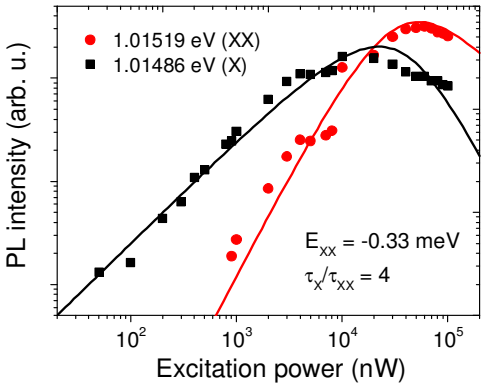

Figure 4-34. Emission intensity vs excitation power density analysis for 0.7 nm InAs QDash structure; symbols - experimental data and solid lines - fit with rate equation model solutions. The inset - microPL spectra for various excitation power densities.

The spectral dependence of the biexciton binding energy within the QDash ensemble (more inhomogeneous than the other samples) is a little bit more pronounced than for the previously described structures. For the smallest QDashes within the series the biexciton binding energy decreases with the emission energy, i.e. the lower the QDash height the smaller the biexciton binding energy. This behaviour can be interpreted as the strong confinement induced effect. The carriers are spatially confined and the repulsive Coulomb interaction results in antibinding biexciton state of higher energy than the single neutral exciton, for which only the attractive interactions are present. This is in agreement with the small nominal height of QDashes in this structure on the order of 2.5 nm and the additional in-plane localization which can be caused by the confining potential fluctuations.

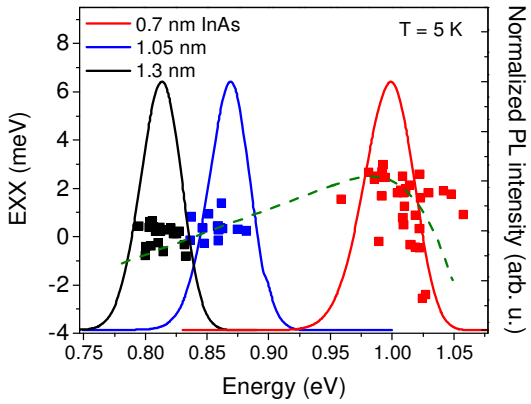

Figure 4-35. Biexciton binding energy dependence on exciton emission energy (symbols) for QDash structures with various InAs layer thickness together with PL spectra of respective QDash structures (solid lines); the green dashed line is the guide to the eye.

In the case of low-energy samples no clear trend of the biexciton binding energy as a function of exciton emission energy can be found for each sample individually. This is at least partially caused by the large scattering of determined values (due to large QDash ensemble inhomogeneity leading to overlap of density of states from different QDashes and influence of local environment) together with the fact that the exciton emission energy does not reflect the QDash size changes only. Considering both these samples, the trend is opposite to the previous case. Lower exciton emission energy is associated with lower biexciton binding energy, consistent with the piezoelectricity being the mechanism determining the strength of biexciton binding within the QDash. In the intermediate regime the biexciton binding energy dependence on the nanostructures size is expected to have a maximum [Nar05]. The exciton to biexciton lifetime ratio obtained from the fitting procedure of intensity vs. excitation power density dependence with curves from the rate equation model is in the range of 2 - 4, suggesting that all the investigated structures should be considered as rather strongly confined, despite their relatively large size. One of the criterions distinguishing weak from strong confinement regime is the relation between the free exciton coherence volume related to the exciton Bohr radius and the physical nanostructure volume. For the investigated structures the physical volume is at most 3.5 x 20 x 150 nm^3, which is still about 16 times smaller than the exciton coherence volume for bulk InAs (exciton Bohr radius r_X = 34 nm), in agreement with the strong quantum confinement regime suggested by the experimental results. The second requirement for the truly strong confinement is the exciton binding energy lower than the quantization energy, which is not fulfilled in the case of the investigated structures, as the inter-level spacing is typically in the range of 10 - 20 meV for electrons

[Syp13, Kac12, Mus12-1], in comparison to 15 - 33 meV exciton binding energy for InAs nanostructures [Mas02, Mic03]. This locates the QDashes somewhere in the intermediate quantum confinement regime. The obtained results show that in view of carrier dynamics they are still in rather strong confinement regime, but the quantization energy is low enough to make the correlation effects quite important. This is reflected in the presented biexciton binding energy dependence on the exciton emission energy, characteristic rather for the weakened confining potential. Those observations emphasize the importance of the height as the direction of the strongest confinement, even though the overall physical volume of the QDash is rather large, the confinement conditions still cannot be considered as weak due to the significant wave function squeezing in the transverse directions.

In the case of the investigated structures the cross-over between different confinement regimes was observed and different physical mechanisms driving the optical properties of emission were identified, i.e. quantum confinement effects in the case of QDash with 12 x 2 nm^2 cross-section and piezoelectric effects in the case of larger structures, with typical dimensions of 20 x 3.5 nm^2. The nanostructures dimensions enabling observation of different confinement regimes were obtained experimentally for InAs/InGaAlAs/InP material system. It was also shown that the kinetics of exciton and biexciton with respect to each other is determined by the confinement regime and so the QDash size in the direction of the strongest confinement, but the biexciton binding energy follows rather the nanostructure volume changes and it is governed by the piezoelectric effects.

4.3.2. Decoherence mechanisms

To study the decoherence mechanisms the width of individual emission lines and its temperature dependence was examined. There is expected a weaker decoherence in comparison to QDs in the same material system due to the elongation (increased volume). Available samples enable also to examine the impact of confinement (QDash height) on the exciton dephasing.

First of all, the observed low-temperature emission linewidths are strongly influenced by the spectral diffusion effects, as they are almost 2 orders of magnitude larger than the lifetime-limited homogeneous broadening corresponding to 1-2 ns exciton lifetime typical for InAs/InP quantum dashes (Figure 4-36.) [Syp13]. The line shape is a Gaussian, proving the supremacy of fluctuations in the environment over the inherent QDash characteristics. For the

low-energy structures most of the lines have the FWHM in the range of 50 - 300 μeV (Figure 4-36.), with the maximum of the distribution slightly lower for the highest QDashes. The higher-energy structures exhibit also slightly stronger variation in the FWHM from dash to dash - values up to 550 μeV are quite common, with the most typical broadening of 250 - 300 μeV.

The spectral dependence of the determined linewidths is rather uniform for each sample separately (Figure 4-37.), which can be again traced back to the confining potential inhomogeneity but a slight decreasing trend with the increasing QDash height was observed (grey dashed line being a guide to the eye in Figure 4-37.), in agreement with the localization-energy-induced trend.

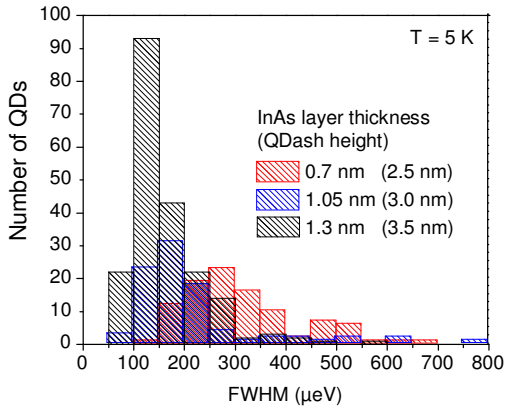

Figure 4-36. Histogram of low-temperature FWHM values for QDash structures with different InAs layer thickness (QDash height).

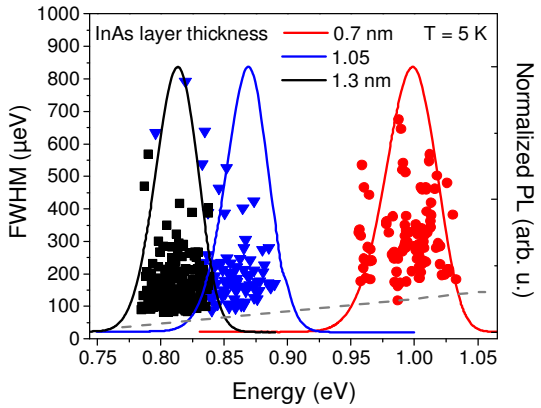

Figure 4-37. Spectral dependence of low-temperature FWHM values for QDash structures with different InAs layer thickness (QDash height) - symbols, together with respective PL spectra (solid lines) and dashed grey line being guide to the eye.

As the temperature is increased, another decoherence mechanisms, like interaction with phonons, can start to play a role. At low temperature no phonon-related spectral features were observed, in agreement with significantly lower visibility of emission sidebands related to the acoustic phonons. To study the influence of the acoustic phonons the linewidth of individual excitonic emission was examined as a function of temperature. To emphasize the thermal effects, the low-temperature FWHM determined by the spectral diffusion effects was subtracted from the temperature dependence. The behaviour is qualitatively the same for all structures under investigation (Figure 4-38), i.e. at first the FWHM increases slowly due to the increasing contribution of the phonon-assisted emission to the Gaussian broadened and spectral diffusion dominated peak. In the range of 30 - 60 K the increase becomes more abrupt and the FWHM starts corresponding mostly to the phonon sidebands width at the half peak maximum of the overall emission (see Section 3.2.2, Figure 3-39). The comparison of typical results for structures with different height (Figure 4-38) shows a decreasing impact of the phonon decoherence for higher QDashes, in agreement with a trend expected for the increased localization energy [Bor05].

The observed differences are not very well pronounced and the spread of the results within the sample, due to rather broad distribution of the QDash size and shape among the ensemble. Moreover, the cross-sectional size distribution is enhanced due to confining potential fluctuations, and it makes the nominal height difference between the samples less pronounced. Another thing is that the height difference among the series is not that big after all. To account for the impact of the height more quantitatively and see how big should be the differences for the experimentally addressed size range, calculations of the phonon-assisted recombination of the exciton confined within a QDash were performed[4]. For the sake of simplicity, a harmonic confining potential was assumed for the cross-sectional directions to obtain the single particle wave functions (identical for electron and holes) and the excitonic effects were included within the configuration-interaction approach. Two mechanisms of carrier-phonon coupling, i.e. the deformation potential and piezoelectric coupling were taken into consideration [Gro05].

[4] Calculations performed by Łukasz Dusanowski and Paweł Machnikowski (Institute of Physics, WRUT).

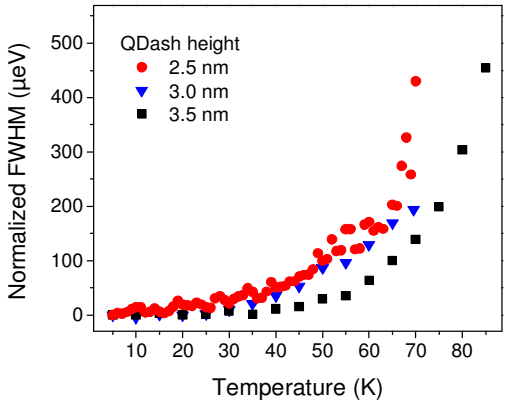

Figure 4-38. Temperature dependence of FWHM for QDash structures for various QDash height (InAs layer thickness). Low-temperature FWHM values were subtracted for clarity.

In Figure 4-39 the results of thermal broadening for different QDash heights are presented for the nanostructure length equal 100 nm, the width scaling proportionally to the size in the growth direction after [Sau05] and the spectral diffusion effects modelled as a convolution with a Gaussian peak of 0.1 meV width. Indeed, the enlarged QDash height decreases slightly the phonon-induced decoherence, but the differences are rather subtle for the height changing in the range from 2 nm up to 4.5 mn, in agreement with the experimental results presented above. What is not consistent with the experimental results is the rate of this increase in the temperature range up to 100 K, accessible in the measurements. Based on the calculations the thermally-induced broadening should be much slower. The possible explanation of this discrepancy are the stronger spectral diffusion effects, possibly increasing with temperature or the limited wave function extension in the elongation direction, not following strictly the nanostructure shape anisotropy. To differentiate between those two effects further calculations were performed within the previously described framework.

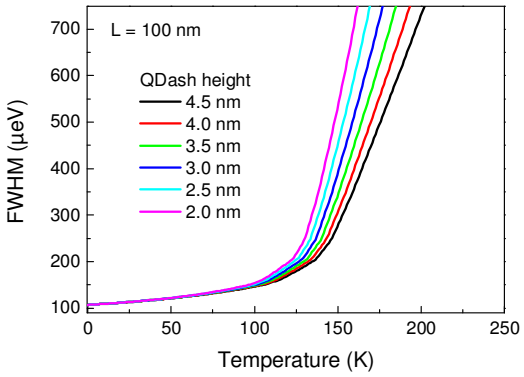

Figure 4-39. Calculated temperature dependence of FWHM for various QDash height (colours). The QDash length was assumed to be 100 nm and the width scaling proportionally to the height with the ratio equal to 5.5 after [Sau05]. The spectral diffusion effects are included by convolution of the QDash emission with Gaussian of 0.1 meV width.

In Figure 4-40 the influence of the increased spectral diffusion (different colours) is presented showing that the low-temperature FWHM should exceed 300 μeV to account for the experimentally observed increase in the FWHM, which is contrary to the typical line broadening at 5 K. It shows that the experimentally observed increase in the FWHM with temperature cannot be explained by the spectral diffusion effects. Additionally, what is apparent and intuitive, the variation between QDashes of different heights (solid and dashed line) is diminished if the spectral diffusion contribution is increased.

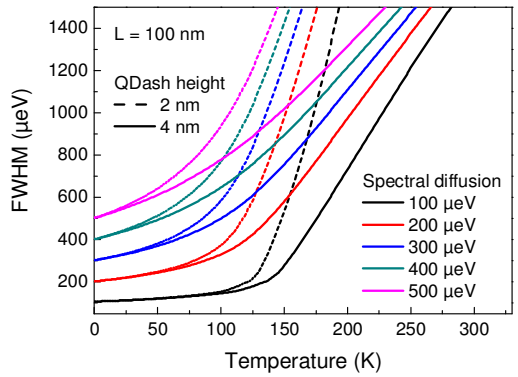

Figure 4-40. Calculated temperature dependence of FWHM for QDashes of 2 and 4 nm height and for various spectral diffusion strength (the width of the Gaussian). The QDash length is assumed to be 100 nm and the width scales proportionally to the height with the ratio equals 5.5 after [Sau05].

To test the hypothesis on a decreased wave function extension, analogical calculations for the cross-sectional size corresponding to the smallest QDashes and for the different QDash

length, were performed assuming 0.1 meV low-temperature spectral diffusion broadening (Figure 4-41).

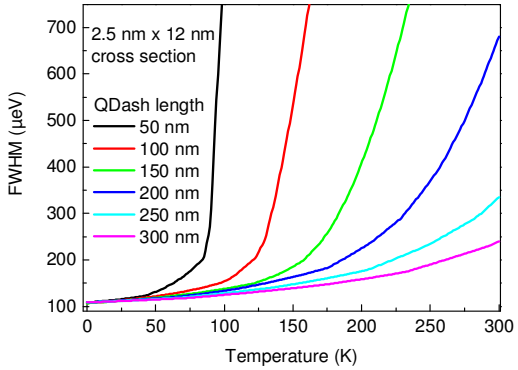

Figure 4-41. Calculated temperature dependence of FWHM for various QDash length. The QDash cross section is assumed to be 2.5 nm x 12 nm (similar to the smallest QDash structures examined experimentally, i.e. for 0.7 nm InAs) and the spectral diffusion effects are included by convolution of QDash emission with Gaussian with 0.1 meV broadening.

These theoretical results suggest that the wave function extension within the QDash should be much smaller than the nanostructure length (in the range of 50 nm) to account for the experimental observations. This can be a result of Coulomb attraction, which is definitely non negligible for QDashes, as argued previously, or the influence of carrier trapping centres within individual nanostructures, both limiting the wave function extension in the elongation direction. However, the single particle calculations within the 8 band **k·p** approach[5] [And10, And13] performed for realistic QDash geometries representing investigated structure series, i.e. 12 x 2.5 nm^2, 16 x 3.0 nm^2 and 20 x 3.5 nm^2 cross-sections and length equals 100 nm, show that it is inherent for these structures that the wave function extension does not follow strictly the nanostructure real space geometry, but the single particle probability densities are actually much more concentrated. The width of the electron/hole probability density distribution in the elongation direction is rather similar and equals approx. 30 nm. The comparison between the single particle picture and the calculations performed including the excitonic effects for similar QDash geometry of 25 x 4.5 x 100 nm^3 [Kac12] points out at the strain as an underlying origin of the shortening of the effective length of the QDash structure (in a sense of the wave function extension). For these calculations the strain effects were not fully accounted for and as a result the wave function extension reaches even 80 nm.

[5] Calculations performed by Janusz Andrzejewski (Institute of Physics, WRUT).

The comparison between the two groups of investigated nanostructures can provide an insight into the influence of geometry and confinement on the exciton decoherence. For both physical systems the low-temperature FWHM is rather high, in the range of hundreds μeV, and determined by spectral diffusion effects. However, determined values are typically lower for the InAs/InP QDashes which can be related to much deeper confining potential and additional spectral diffusion process for InGaAs/GaAs QDs related to the localized character of the states in the WL. In both cases the FWHM is larger for higher exciton emission energy. The differences in FWHM dependence on temperature between the investigated groups are not well pronounced as a result of similar exciton probability density distribution. It determines both the coupling strength and the number of phonons efficiently interacting with the exciton confined within the nanoobject which has been identified as the main decoherence mechanism. For InGaAs QDs the wave function extension is determined by excitonic effects due to weak confinement regime and in the case of InAs QDashes the strain prevents it to follow the shape elongation exactly with additional localization provided by the potential fluctuations. The advantages of the strongly elongated nanostructures have been argued theoretically but it cannot be directly observed in the time-integrated PL spectra due to strong spectral diffusion effects.

The microPL study on InAs/InP QDashes confirms the importance of the existence of the additional carrier trapping centres within the individual QDashes. They decrease the effective anisotropy of those strongly elongated nanostructures, in spite of the fact, that they do not contribute to the emission directly. This part of the work on optical properties of emission from individual QDashes shows that the symmetry breaking caused by the shape asymmetry is indispensable for optical properties anisotropy (e.g., polarization degree, fine structure splitting), and is further enhanced due the to piezoelectric effects enhanced for larger nanostructures, but it is not as strong as the QDash shape anisotropy itself.

Summary

The main objective of the conducted research was to determine experimentally and describe the unknown optical properties of epitaxial nanostructures with a broken in-plane rotational symmetry, and to identify the underlying physical reasons of the observed features. The study was performed on two groups of nanostructures differing in the lateral aspect ratio and the material system, i.e. InGaAs/GaAs elongated QDs and InAs/InGaAlAs/InP QDashes, both application relevant and interesting also in a view of the fundamental research as new physical systems. To probe the optical properties of the investigated structures, photoreflectance and (polarization-resolved) photoluminescence (also with high spatial and spectral resolution) experimental techniques were utilized. The choice of the investigated structures enabled to study the influence of the nanostructure elongation in different confinement regimes, which was proven to be significantly weakened in the case of the GaAs-based structures and rather strong or intermediate for the QDashes. Such data have not been reported till now for nanostructures of that large shape anisotropy, fabricated by means of epitaxial self-assembled growth.

In the main part of the thesis the issue of the selective polarization properties of the emission, which are expected to be much different in the case of the elongated nanostructures, is addressed. The performed experiments enabled to describe the influence of the in-plane geometry on the polarization degree of surface emission and also pointed out the importance of the out-of plane dimension, especially if fully polarized emission is demanded. The obtained results showed that all these effects, together with the confinement regime, need to be carefully examined and taken into account to properly interpret the results of the polarization-resolved measurements and to tailor the polarization properties of such emitters. Polarization-resolved photoluminescence was also proven to be a useful experimental technique to probe carrier trapping on potential fluctuations in the case of the strongly elongated nanostructures. The existence of such fluctuations in InAs/InP QDashes was experimentally evidenced for the first time, and confirmed by the electronic structure modelling based on the **k·p** theory. This is a crucial observation in view of single nanostructure-based applications, as it changes significantly the character of the nanoobject ground state and influences also the higher energy states, e.g. their kinetics and polarization properties. In view of the presented results, the homogeneity of individual QDashes needs to be improved to fully explore the advantages and capabilities resulting from their strong in-plane anisotropy. The intermediate confinement regime characteristic for those structures is

very interesting, as it gives the possibility of independent control of the carrier dynamics and the carrier correlation effects, as evidenced in this thesis. For the InGaAs/GaAs large QDs, the significantly weakened confinement regime is the reason for the optical properties not following directly the QD shape anisotropy. As a result, the spatial extension of the carrier probability distribution is much less asymmetric than the QD physical shape itself, but the enlarged volume enables to take advantage of the increased exciton coherence volume, beneficial for both the fundamental quantum electrodynamics study and high repetition rates of future devices.

In addition, the PL quenching mechanisms were identified and the weakened exciton decoherence being a result of the increased both in-plane elongation and height, was evidenced. The exciton fine structure splitting was shown to be rather negligible in the case of GaAs-based QDs, but can reach values as big as 300 μeV for the QDashes. Such large differences were shown to be caused by the confinement-dependent wave function sensitivity to the nanostructure anisotropy. These results are of significant importance in view of future applications of the investigated structures as active regions of novel photonic devices.

The direct comparison between investigated nanostructure groups cannot be easily done as the detailed study have revealed that they constitute significantly distinct physical systems despite their apparent similarities. The important differences are related to the quantum confinement, which is significantly weakened and shallow in InGaAs QDs and strong or intermediate and much deeper for InAs QDashes. It occured that the optical properties of both groups are not primaly determined by their geometry, but rather the localization effects. These are of completely different origin and character. For InGaAs QDs the localized states in the WL and the transfer between them and the 2D continuum of states and the dots play a crucial role, whereas additional carrier trapping on potential fluctuations within the individual QDash determines the properties of InAs/InP structures.

The obtained results are original and unique world-wide, constituting important summary of the optical properties of the two novel groups of quasi-zero-dimensional nanostructures with enhanced lateral aspect ratio, some of them being already published in internationally-recognized physical journals (*Journal of Applied Physics*, *Physical Review B*) or presented during international conferences and workshops (International Conference on Quantum Dots, International Conference on Optics of Excitons in Confined Systems, Conference on Physics of Light-Matter Coupling in Nanostructures, International Workshop on Optical Properties of Nanostructures, etc.).

Publications

- **directly on the topic of the thesis**

1. A. Maryński, G. Sęk, **A. Musiał**, J. Andrzejewski, J. Misiewicz, C. Gilfert, J. P. Reithmaier, A. Capua, O. Karni, D. Gready, G. Eisenstein, G. Atiya, W. D. Kaplan, S. Kölling, 'Electronic structure, morphology and emission polarization of enhanced symmetry InAs quantum-dot-like structures grown on InP substrates by molecular beam epitaxy', submitted to ***Journal of Applied Physics*** (2013)

2. **A. Musiał**, P. Podemski, G. Sęk, P. Kaczmarkiewicz, J. Andrzejewski, P. Machnikowski, J. Misiewicz, S. Hein, A. Somers, S. Höfling, J. P. Reithmaier, and A. Forchel, 'Height-driven linear polarization of the surface emission from quantum dashes', ***Semiconductor Science and Technology*** 27, 105022 (2012)

   Related invited articles published on-line:

   A. Musiał, P. Podemski, G. Sęk, P. Kaczmarkiewicz, J. Andrzejewski, P. Machnikowski, J. Misiewicz, S. Hein, A. Somers, S. Höfling, J. P. Reithmaier, and A. Forchel, 'Towards full control of polarization properties of emission from nanostructure', ***Labtalk*** 51389, October 2012

   A. Musiał, P. Podemski, G. Sęk, P. Kaczmarkiewicz, J. Andrzejewski, P Machnikowski, J. Misiewicz, S. Hein, A. Somers, S. Höfling, J. P. Reithmaier, and A. Forchel, 'Polarization of the surface emission from quantum dashes', ***Europhysics News*** 43 (6), 2012

3. Ł. Dusanowski, G. Sęk, **A. Musiał**, P. Podemski, M. Misiewicz, A. Löffler, S. Höfling, S. Reitzenstein, and A. Forchel, 'Multiexcitonic emission from single strongly elongated InGaAs/GaAs quantum dots', ***Journal of Applied Physics*** 111, 063522 (2012)

   Related invited article published on-line:

   Ł. Dusanowski, G. Sęk, **A. Musiał**, P. Podemski, M. Misiewicz, A. Löffler, S. Höfling, S. Reitzenstein, and A. Forchel, 'Elongated quantum dots emit via multiexcitons', ***nanotechweb.org***, July 2012

4. **A. Musiał**, P. Kaczmarkiewicz, G. Sęk, P. Podemski, P. Machnikowski, J. Misiewicz, S. Hein, S. Höfling, and A. Forchel, 'Carrier trapping and luminescence polarization in quantum dashes', ***Physical Review B*** 85, 035314 (2012)

5. G. Sęk, **A. Musiał**, P. Podemski, and J. Misiewicz, 'On the applicability of a few level rate equation model to the determination of exciton versus biexciton kinetics in quasi-zero-dimensional structures', ***Journal of Applied Physics*** 108, 033507 (2010)

6. **A. Musiał**, G. Sęk, A. Maryński, P. Podemski, J. Misiewicz, A. Löffler, S. Höfling, S. Reitzenstein, J. P. Reithmaier, and A. Forchel,'Temperature dependence of photoluminescence from epitaxial InGaAs/GaAs quantum dots with high lateral aspect ratio', ***Acta Physica Polonica A*** 120, 883 (2011)

7. P. Kaczmarkiewicz, **A. Musiał**, G. Sęk, P. Podemski, P. Machnikowski, and J. Misiewicz, 'Hole subband mixing and polarization of luminescence from quantum dashes: a simple model', ***Acta Physica Polonica A*** 119, 633 (2011)

8. **A. Musiał**, G. Sęk, P. Podemski, M. Syperek, J. Misiewicz, A. Löffler, S. Höfling, and A. Forchel, 'Excitonic complexes in InGaAs/GaAs quantum dash structures', ***Journal of Physics: Conference Series*** 245, 012054 (2010)

9. M. Syperek, **A. Musiał**, G. Sęk, P. Podemski, J. Misiewicz, A. Löffler, S. Höfling, L. Worschech, and A. Forchel, 'Impact of the localized wetting layer states in carriers relaxation processes and multiexcitonic effects in quantum dash structures', ***AIP Conference Proceedings*** 1399, 563 (2011)

- **others**

10. A. Mika, G. Sęk, K. Ryczko, M. Kozub, **A. Musiał**, A. Maryński, J. Misiewicz, F. Langer, S. Höfling, T. Appel, M. Kamp, and A. Forchel, 'Oscillator strength of optical transitions in InGaAsN/GaAsN/GaAs quantum wells', ***Optical Applicata*** 43, 53 (2013)

11. V. Zuerbig, N. Bugaew, J. P. Reithmaier, M. Kozub, **A. Musiał**, G. Sęk, and J. Misiewicz 'Growth temperature dependence of wetting layer formation in high density InGaAs/GaAs quantum dot structures grown by droplet epitaxy', ***Japanese Journal of Applied Physics*** 51, 085501 (2012)

12. G. Sęk , **A. Musiał**, P. Podemski, M. Syperek, J. Misiewicz, A. Löffler, S. Höfling, and A. Forchel 'Exciton kinetics and few particle effects in self-assembled GaAs-based quantum dashes', ***Journal of Applied Physics*** 107, 096106 (2010)

13. G. Sęk , P. Podemski, **A. Musiał**, J. Misiewicz, S. Hein, S. Höfling, and A. Forchel, 'Exciton and biexciton emission from single InAs/InP quantum dash', ***Journal of Applied Physics*** 105, 086104 (2009)

Selected to: ***Virtual Journal of Nanoscale Science & Technology*** 19, 19 (2009)

14. B. Kolad, **A. Musiał**, and P. Machnikowski, 'Calculation of anharmonic coupling constans between phonon modes in GaAs', ***Acta Physica Polonica A*** 114, 5 (2008)

Conference presentations

- **contributed talks**

1. **A. Musiał**, G. Sęk, A. Maryński, M. Kozub, J. Misiewicz, A. Löffler, S. Höfling, S. Reitzenstein, J. P. Reithmaier, M. Kamp, and A. Forchel, 'Exciton dephasing in large GaAs-based epitaxial nanostructures', ***International Workshop on the Optical Properties of Nanostructures***, Bayreuth 2013

2. **A. Musiał**, P. Kaczmarkiewicz, G. Sęk, P. Podemski, P. Machnikowski, J. Misiewicz, S. Hein, S. Höfling, and A. Forchel, 'Localization effects in polarization of emission from strongly anisotropic quantum-dot like structures', ***41st "Jaszowiec" International School and Conference on the Physics of Semiconductors***, Krynica-Zdrój 2012

3. **A Musiał**, G. Sęk, P. Podemski, M. Kozub, A. Maryński, J. Andrzejewski, P. Kaczmarkiewicz, P. Machnikowski, and J. Misiewicz, 'Wpływ geometrii na polaryzację emisji z kropek kwantowych' (invited lecture), ***II Plenerowa Konferencja Studencka NANOIN***, Bielice 2012

- **posters**

1. **A. Musiał**, Ł. Dusanowski, G. Sęk, A. Maryński, M. Kozub, P. Machnikowski, J. Misiewicz, S. Hein, S. Höfling, M. Kamp, and A. Forchel, 'Exciton dephasing in InAs/InP self-assembled quantum dashes', ***International Conference on Optics of Excitons in Confined Systems OECS13***, Rome 2013

2. **A. Musiał**, A. Maryński, P. Mrowiński, G. Sęk, J. Misiewicz, S. Hein, S. Höfling, M. Kamp, and A. Forchel, 'Diamagnetic coefficient and exciton g-factor of InAs/InP quantum dashes' ***42nd "Jaszowiec" International School and Conference on the Physics of Semiconductors***, Wisła 2013

3. **A. Musiał**, G. Sęk, A. Maryński, M. Kozub, J. Misiewicz, A. Löffler, S. Höfling, S. Reitzenstein, J. P. Reithmaier, M. Kamp, and A. Forchel, 'Temperature dependent emission linewidth and the exciton dephasing in large and asymmetric III-V semiconductor quantum nanostructures', ***16th International Conference on Modulated Semiconductor Structures (MSS-16)***, Wrocław 2013

4. **A. Musiał**, G. Sęk, P. Podemski, J. Andrzejewski, J. Misiewicz, P. Kaczmarkiewicz, P. Machnikowski, S. Hein, A. Somers, S. Höfling, and A. Forchel, 'Insight into electronic and optical properties of quantum dashes on InP', ***One Day Quantum Dot Meeting***, Nottingham 2013

5. **A. Musiał**, G. Sęk, P. Podemski, J. Misiewicz, P. Kaczmarkiewicz, P. Machnikowski, S. Hein, S. Höfling, and A. Forchel, 'Polarization properties of emission from InAs/InP quantum dashes', ***XII Seminarium Powierzchnia i Struktury Cienkowarstwowe SemPiSC***, Szklarska Poręba 2012

6. **A. Musiał**, G. Sęk, A. Maryński, P. Podemski, J. Andrzejewski, J. Misiewicz, P. Kaczmarkiewicz, P. Machnikowski, C. Gilfert, J. P. Reithmaier, A. Löffler, S. Hein, S. Reitzenstein, S. Höfling, and A. Forchel, 'Polarization-resolved photoluminescence as a method of quantum dot shape determination', ***2nd Polish-German Workshop on the Optical Properites of Nanostructures – PL-DE 2012***, Münster 2012

7. **A. Musiał**, G. Sęk, A. Maryński, P. Podemski, J. Andrzejewski, J. Misiewicz, A. Löffler, S. Höfling, S. Reitzenstein, J. P. Reithmaier, and A. Forchel, 'Temperature dependence of the emission from strongly elongated InGaAs/GaAs quantum dots', ***International Conference on Optics of Excitons in Confined Systems – OECS12***, Paris 2011

8. **A. Musiał**, G. Sęk, A. Maryński, P. Podemski, J. Andrzejewski, J. Misiewicz, A. Loffler, S. Hofling, S. Reitzenstein, J. P. Reithmaier, and A. Forchel, 'Thermal quenching of photoluminescence from epitaxial InGaAs/GaAs quantum dots with high lateral aspect ratio', ***40th "Jaszowiec" International School and Conference on the Physics of Semiconductors***, Krynica-Zdrój 2011

9. **A. Musiał**, G. Sęk, P. Podemski, J. Andrzejewski, P. Kaczmarkiewicz, P. Machnikowski, J. Misiewicz, A. Löffler, S. Hein, S. Hofling, J. P. Reithmaier, and A Forchel, 'Polarization properties of the emission from strongly in-plane asymmetric epitaxial nanostructures', ***11th International Conference on Physics of Light-Matter Coupling in Nanostructures - PLMCN 11***, Berlin 2011

10. **A. Musiał**, G. Sęk, P. Podemski, M. Syperek, J. Misiewicz, A. Löffler, S. Hein, S. Höfling, J. P. Reithmaier, and A. Forchel, 'Microphotoluminescence of nanostructures with high lateral aspect ratio', ***Polish-German Workshop on the Optical Properties of Nanostructures***, Wrocław 2010

11. **A. Musiał**, G. Sęk, P. Podemski, M. Syperek, J. Misiewicz, A. Löffler, S. Höfling, and A. Forchel, 'Emission properties of individual self-assembled InGaAs/GaAs quantum dashes', ***39th "Jaszowiec" International School and Conference on the Physics of Semiconductors***, Krynica Zdrój 2010

12. **A. Musiał**, G. Sęk, P. Podemski, M. Syperek, J. Misiewicz, A. Löffler, S. Höfling, and A. Forchel, 'Excitonic complexes in GaAs-based quantum dash structures', ***International Conference on Quantum Dots - QD 2010***, Nottingham 2010

13. **A. Musiał**, G. Sęk, P. Podemski, J. Misiewicz, A. Löffler, S. Höfling, and A. Forchel, 'Few particle effects in the photoluminescence of single self-assembled InGaAs/GaAs quantum dashes', ***38th "Jaszowiec" International School and Conference on the Physics of Semiconductors***, Krynica Zdrój 2009

14. **A. Musiał**, G. Sęk, P. Podemski, J. Misiewicz, A. Löffler, S. Höfling, and A. Forchel, 'Własności optyczne pojedynczych kresek kwantowych InGaAs/GaAs', ***XI Seminarium Powierzchnia i Struktury Cienkowarstwowe,*** Szklarska Poręba 2009

Appendix 1 - list of abbreviations

APT - Atomic Probe Tomography

DOP - the degree of linear polarization (of emission)

E_{XX} - biexciton binding energy

FSS - fine structure splitting for neutral exciton

FWHM - full width at half maximum

LA - longitudinal acoustic phonon modes

LAR - lateral aspect ratio

LO - longitudinal optical phonon modes

MBE - molecular beam epitaxy

ML - monolayer

microPL - microphotoluminescence

PL - photoluminescence

PR - photoreflectance

QD(s) - quantum dot(s)

QDash(es) - quantum dash(es)

QW(s) - quantum well(s)

QWire(s) - quantum wire(s)

SEM - scanning electron microscopy

SQD(s) - single quantum dot(s)

SQDash(es) - single quantum dash(es)

TEM - Transmission Electron Miscroscopy

X - neutral exciton

$X^{+/-}$ - positively/negatively charged exciton (trion)

XX - neutral biexciton

WL - wetting layer

WRUT - Wrocław University of Technology

ZPL - zero phonon line

Bibliography

[Ada04] S. Adachi (ed.), *Handbook on Physical Properties of Semiconductors (Volume 2: III-V Compound Semiconductors)*, Springer (2004)

[And99] L. C. Andreani, G. Panzarini, and J. M. Gerard, *Phys. Rev. B* **60**, 13276 (1999)

[And13] J. Andrzejewski, *J. Comp. Phys.*, in press

[And10] J. Andrzejewski, G. Sęk, E. O'Reilly, A. Fiore, and J. Misiewicz, *J. Appl. Phys* **107**, 073509 (2010)

[Ara82] Y. Arakawa, and H. Sakaki, *Appl. Phys. Lett.* **40**, 939 (1982)

[Bab08] A. Babiński, M. Potemski, S. Raymond, and Z. R. Wasilewski, *Physica E* **40,** 2078 (2008)

[Bar07] A. V. Barzykin, and M. Tachiya, *J. Phys.: Condens. Matter* **19**, 065105 (2007)

[Bay01] M. Bayer, T. L. Reinecke, F. Weidner, A. Larionov, A. McDonald, and A. Forchel, *Phys. Rev. Lett* **86**, 3168 (2001)

[Bay02] M. Bayer, G. Ortner, O. Stern, A. Kuther, A. A. Gorbunov, A. Forchel, P. Hawrylak, S. Fafard, K. Hinzer, T. L. Reinecke, S. N. Walck, J. P. Reithmaier, F. Klopf, and F. Schäfer, *Phys. Rev. B* **65**, 195315 (2002)

[Bay02-1] M. Bayer, and A. Forchel, *Phys. Rev. B* **65**, 041308 (2002)

[Bel98] J. Bellessa, V. Voliotis, R. Grousson, X. L. Wang, M. Ogura, and H. Matsuhata, *Phys. Rev. B* **58**, 9933 (1998)

[Bes03] G. Bester, S. Nair, and A. Zunger, *Phys. Rev. B* **67**, 161306 (2003)

[Bes05] G. Bester, and A. Zunger, *Phys. Rev. B* **71**, 045318 (2005)

[Bor00] P. Borri, W. Langbein, J. M. Hvam, F. Heinrichsdorff, M.-H. Mao, and D. Bimberg, *Appl. Phys. Lett.* 76, 1380 (2000)

[Bor01] P. Borri, S. Schneider, W. Langbein, U. Woggon, A. E. Zhukov, V. M. Ustinov, N. N. Ledentsov, Zh. I. Alferov, D. Ouyang, and D. Bimberg, *Appl. Phys. Lett.* **79**, 2633 (2001)

[Bor02] P. Borri, W. Langbein, S. Schneider, U. Woggon, R. L. Sellin, D. Ouyang, and D. Bimberg, *Phys. Rev. Lett.* **89**, 187401 (2002)

[Bor05] P. Borri, W. Langbein, U. Woggon, V. Stavarache, D. Reuter, and A. D. Wieck, *Phys. Rev. B* **71**, 115328 (2005)

[Bos12] R. Bose, D. Sridharan, H. Kim, G. S. Solomon, and E. Waks, *Phys. Rev. Lett.* **108**, 227402 (2012)

[Bra02] J. Brault, M. Gendry, G. Grenet, G. Hollinger, J. Olivares, B. Salem, T. Benyattou, and G. Bremond, *J. Appl. Phys.* **92**, 506 (2002)

[Bry88] G. W. Bryant, *Phys. Rev. B* **37**, 8763 (1988)

[Can00] A. Canning, L. W. Wang, A. Williamson, and A. Zunger, *J. Comp. Phys.* **160**, 29 (2000)

[Cha06] N. Chauvin, B. Salem, G. Bremond, G. Guillot, C. Bru-Chevallier, and M. Gendry, *J. Appl. Phys.* **100**, 073702 (2006)

[Cha06-1] N. Chauvin, G. Bremond, C. Bru-Chevalier, E. Dupuy, P. Regreny, and M. Gendry, *Phys. Status Solidi c* **3**, 3912 (2006)

[Cha09] N. Chauvin, P. Nedel, C. Seassal, B. Ben Bakir, X. Letartre, M. Gendry, A. Fiore, and P. Viktorovitch, *Phys. Rev. B* **80**, 045315 (2009)

[Cho98] Y.-H. Cho, G. H. Gainer, A. J. Fischer, J. J. Song, S. Keller, U. K. Mishra, and S. P. DenBaars, *Appl. Phys. Lett.* **73**, 1370 (1998)

[Cir97] J. I. Cirac, P. Zoller, H. J. Kimble, and H. Mabuchi, *Phys. Rev. Lett.* **78**, 3221 (1997)

[Cus96] M. A. Cusackm P. R. Briddon, and M. Jaros, *Phys. Rev. B* **54**, R2300 (1996)

[Dek00] E. Dekel, D. Gershoni, E. Ehrenfreund, J. M. Garcia, and P. M. Petroff, *Phys. Rev. B* **61**, 11009 (2000)

[Der04] H. Dery, E. Benisty, A. Epstein, R. Alizon, V. Mikhelashvili, G. Eisenstein, R. Schwertberger, D. Gold, J. P. Reithmaier, and A. Forchel, *J. Appl. Phys.* **95**, 6103 (2004)

[Dij08] H. S. Djie, Y. Wang, Y.-H. Ding, D.-N. Wang, J. C. M. Hwang, X.-M. Fang, Y. Wu, J. M. Fastenau, A. W. K. Liu, G. T. Dang, W. H. Chang, and B. S. Ooi, *IEEE J. Select. Topics Quantum Electron.* **14**, 1239 (2008)

[Dup08] E. Dupuy, G. Xu, P. Regreny, Y. Robach, M. Gendry, G. Patriarche, N. Chauvin, C. Bru-Chevallier, D. Morris, N. Pauc, V. Aimez, and D. Drouin, Conference on Indium Phosphide and Related Materials 2008 (unpublished)

[Dus12] Ł. Dusanowski, G. Sęk, A. Musiał, P. Podemski, J. Misiewicz, A. Löffler, S. Höfling, S. Reitzenstein, and A. Forchel, *J. Appl. Phys.* **111**, 063522 (2012)

[Eng12] D. Englund, A. Majumdar, M. Bajcsy, A. Faraon, P. Petroff, and J. Vučković, *Phys. Rev. Lett.* **108**, 093604 (2012)

[Faf96] S. Fafard, Z. Wasilewski, J. McCaffrey, S. Raymond, and Charbonneau, *Appl. Phys. Lett.* **68**, 991 (1996)

[Faf99] S. Fafard, Z. R. Wasilewski, and M. Spanner, *Appl. Phys. Lett.* **75**, 1866 (1999)

[Fav05] I. Favero, G. Cassabois, A. Jankovic, R. Ferreira, D. Darson, C. Voisin, C. Delalande, Ph. Roussignol, A. Badolato, P. M. Petroff, and J. M. Gerard, *Appl. Phys. Lett.* **86**, 041904 (2005)

[Fav07] I. Favero, A. A. Berthelot, G. Cassabois, C. Voisin, C. Delalande, Ph. Roussignol, R. Ferreira, and J. M. Gerard, *Phys. Rev. B* **75**, 073308 (2007)

[Fer09] R. Ferriera, A. Berthelot, T. Grange, E. Zibik, G. Cassabois, and L. Wilson, *J. Appl. Phys.* **105**, 122412 (2009)

[Fin02] J. J. Finley, D. J. Mowbray, M. S. Skolnick, A. D. Ashmore, C. Baker, A. F. G. Monte, and M. Hopkins, *Phys. Rev. B* 66, 153316 (2002)

[Fon98] L. R. C. Fonseca, J. L. Jimenez, J. P. Leburton, and R. M. Martin, *Phys. Rev. B* **57**, 4017 (1998)

[Gil10] C. Gilfert, E.-M. Pavalescu, and J. P. Reithmaier, *Appl. Phys. Lett.* **96**, 191903 (2010)

[Gon00] L. Gonzales, J. M. Garcia, R. Garcia, F. Briones, J. Martinez-Pastor, and C. Ballesteros, *Appl. Phys. Lett.* **76**, 1104 (2000)

[Gro05] A. Grodecka, L. Jacak, P. Machnikowski, K. Roszak, chapter in *Quantum Dots: Research Developments*, ed. by P. A. Ling, Nova Science Publishers, New York, p. 47 (2005)

[Gru95] M. Grundmann, O. Stier, and D. Bimberg, *Phys. Rev. B* **52**, 11969 (1995)

[Gru02] M. Grundmann (ed.), *Nano-Optoelectronics: Concepts, Physics and Devices*, Springer (2002)

[Güç09] A. D. Güçlü, C. J. Umrigar, H. Jiang, and H. U. Baranger, *Phys. Rev. B* **80**, 201302 (2009)

[Gui03] T. Guillet, R. Grousson, V. Voliotis, X. L. Wang, and M. Ogura, *Phys. Rev. B* **68**, 045319 (2003)

[Guo97] S. P. Guo, H. Ohno, A. Shen, F. Matsukura, and Y. Ohno, *Appl. Phys. Lett.* **70**, 2738 (1997)

[He_08] L. He, M. Gong, C.-F. Li, G.-C. Guo, and A. Zunger, *Phys. Rev. Lett.* **101**, 157405 (2008)

[Hec09] S. C. Heck, S. Osborne, S. B. Healy, and E. P. O'Reilly, *IEEE J. Quantum Electron.* **45**, 1508 (2009)

[Hei08] S. Hein, P. Podemski, G. Sęk, J. Misiewicz, P. Ridha, A. Fiore, G. Patriarche, S. Höfling, and A. Forchel, *Appl. Phys. Lett.* **94**, 241113 (2008)

[Hu_01] J. Hu, L.-S. Li, W. Yang, L. Manna, L.-W. Wang, A. P. Alivisatos, *Science* **292**, 2060 (2001)

[Ike11] Y. Ikeuchi, T. Inoue, M. Asada, Y. Harada, T. Kita, E. Taguchi, and H. Yasuda, *Appl. Phys. Express* **4**, 062001 (2011)

[Ima99] A. Imamoglu, D. D. Awschalom, G. Burkard, D. P. DiVincenzo, D. Loss, M. Sherwin, and A. Small, *Phys. Rev. Lett.* **83**, 4204 (1999)

[Ito91] T. Ito, and M. Furumiya, *J. Lumin.* **48-9**, 704 (1991)

[Jia 97-1] H. Jiang, and J. Singh, *Appl. Phys. Lett.* **71**, 3239 (1997)

[Jia97-1] H. Jiang, and J. Singh, *Phys. Rev. B* **56**, 4696 (1997)

[Jia98] H. Jiang, and J. Singh, *IEEE J. Quantum Electron.* **34**, 1188 (1998)

[Jo_10] M. Jo, T. Mano, and K. Sakoda, *Appl. Phys. Exp.* **3**, 045502 (2010)

[Kac10] P. Kaczmarkiewicz, A. Musiał, G. Sęk, P. Podemski, P. Machnikowski, and J. Misiewicz, *Acta Phys. Pol. A*. **118**, 333 (2010)

[Kac11] P. Kaczmarkiewicz, A. Musial, G. Sęk, P. Podemski, P. Machnikowski, J. Misiewicz, *Acta Phys. Pol. A* **119**, 633 (2011)

[Kac12] P. Kaczmarkiewicz, P. Machnikowski, *Semicond. Sci. Technol.* **27**, 105012 (2012)

[Kad10] E. Kadantsev, and P. Hawrylak, *Phys. Rev. B* **81**, 045311 (2010)

[Khi06] G. Khitrova, H. M. Gibbs, M. Kira, S. W. Koch, and A. Scherer, *Nature Phys.* **2**, 81 (2006)

[Kim98] J. Kim, L.-W. Wang, and A. Zunger, *Phys. Rev. B* **57**, R9408 (1998)

[Kim03] J. S. Kim, J. H. Lee, S. U. Hong, W. S. Han, H.-S. Kwack, and D. K. Oh, *Appl. Phys. Lett.* **83**, 3785 (2003)

[Kim05] J. S. Kim, J. H. Lee, S. U. Hong, H.-S. Kwack, B. S. Choi, and D. K. Oh, *Appl. Phys. Lett.* **87**, 053102 (2005)

[Kit02] T. Kita, O. Wada, H. Ebe, Y. Nakata, and M. Sugawara, *Jpn. J. Appl. Phys.* **41**, L1143 (2002)

[Kog91] N. Koguchi, S. Takahashi, and T. Chikyow, *J. Cryst. Growth* **111**, 688 (1991)

[Kou04] A. V. Koudinov, I. A. Akimov, Yu. G. Kusrayev, and F. Henneberger, *Phys. Rev. B* **70**, 241305 (2004)

[Kow07] K. Kowalik, O. Krebs, A. Golnik, J. Suffczyński, P. Wojnar, J. Kossut, J. A. Gaj, and P. Voisin, *Phys. Rev. B* **75**, 195340 (2007)

[Lau86] P. Lautenschlager, M. Garriga, S. Logothetidis, and M. Cardona, *Phys. Rev. B* **34**, 2458 (1986)

[Leo94] D. Leonard, K. Pond, and P. M. Petroff, *Phys. Rev. B* **50**, 11687 (1994)

[Leo98] R. Leon, and S. Fafard, *Phys. Rev. B* **58**, 1726 (1998)

[Li_02] H. Li, T. Daniels-Race, and M.-A. Hasan, *Appl. Phys. Lett.* **80**, 1367 (2002)

[Lia98] X. Z. Liao, J. Zou, X. F. Duan, and D. J. Cockayne, R. Leon, and C. Lobo, *Phys. Rev. B* **58**, 4235 (1998)

[Liu00] N. Liu, J. Tersoff, O. Baklenov, A. L. Holmes Jr., and C. K. Shih, *Phys. Rev. Lett.* **84**, 334 (2000)

[Liu05] Z. Liu, B. B. Goldberg, S. B. Ippolito, A. N. Vamivakas, M. S. Ünlü, and R. Mirim, *Appl. Phys. Lett.* **87**, 071905 (2005)

[Löf06] A. Löffler, J. P. Reithmaier, A. Forchel, A. Sauerwald, D. Peskes, T. Kümmell, and G. Bacher, *J. Cryst. Growth* **286**, 6 (2006)

[Mäd94] K. A. Mäder, and A. Zunger, *Phys. Rev. B* **50**, 17393 (1994)

[Maj11] M. A. Majid, D. T. D. Childs, H. Shahid, R. Airey, K. Kennedy, R. A. Hogg, E. Clarke, P. Spencer, and R. Murray, *Electron. Lett.* **47**, 44 (2011)

[Mar13] A. Maryński, G. Sęk, A. Musiał, J. Andrzejewski, J. Misiewicz, C. Gilfert, J. P. Reithmaier, A. Capua, O. Karni, D. Gready, G. Eisenstein, G. Atiya, W. D. Kaplan, S. Kölling, 'Electronic structure, morphology and emission polarization of enhanced symmetry InAs quantum-dot-like structures grown on InP substrates by molecular beam epitaxy', submitted to *J. Appl. Phys.* (2013)

[Mas02] Y. Masumoto, T. Takagahara (ed.), *Semiconductor Quantum Dots: Physics, Spectroscopy and Applications,* Springer (2002)

[Mas11] Y. Masumoto, S. Yoshida, M. Ikezawa, S. Tomimoto, and Y. Sakuma, *Appl. Phys. Lett.* **98**, 061905 (2011)

[Men03] T. Mensing, L. Worschech, R. Schwertberger, J. P. Reithmaier, and A. Forchel, *Appl. Phys. Lett.* **82**, 2799 (2003)

[Mli09] V. Mlinar, and A. Zunger, *Phys. Rev. B* **79**, 115416 (2009)

[Mic03] P.Michler (ed.), *Single Quantum Dots: Fundamentals, Applications and New Concepts*, Springer (2003)

[Mis04] P. Miska, J. Even, C. Platz, B. Salem, T. Benyattou, C. Bru-Chevalier, G. Guillot, G. Bremond, Kh. Moumanis, F. H. Julien, O. Marty, C. Monat, and M. Gendry, *J. Appl. Phys.* **95**, 1074 (2004)

[Moe03] S. Moehl, H. Zhao, B. Dal Don, S. Wachter, and H. Kalt, *J. Appl. Phys.* **93**, 6265 (2003)

[Moo13] G. Moody, R. Singh, H. Li, I. A. Akimov, M. Bayer, D. Reuter, A. D. Wieck, A. S. Bracker, D. Gammon, and S. T. Cundiff, *Phys. Rev. B* **87**, 041304 (2013)

[Mus12] A. Musiał, P. Podemski, G. Sęk, P. Kaczmarkiewicz, J. Andrzejewski, P. Machnikowski, J. Misiewicz, S. Hein, A. Somers, S. Höfling, J. P. Reithmaier, and A. Forchel, *Semicond. Sci. Technol.* **27**, 105022 (2012)

[Mus12-1] A. Musiał, P. Kaczmarkiewicz, G. Sęk, P. Podemski, P. Machnikowski, J. Misiewicz, S. Hein, S. Höfling, and A. Forchel, *Phys. Rev. B* **85**, 035314 (2012)

[Nar05] G. A. Narvaez, G. Bester, and A. Zunger, *Phys. Rev. B* **72**, 245318 (2005)

[Nar06] G. A. Narvaez, G. Bester, A. Franceschetti, and A. Zunger, *Phys. Rev. B* **74**, 205422 (2006)

[Ohn11] S. Ohno, S. Adachi, R. Kaji, S. Muto, and H. Sasakura, *Appl. Phys. Lett.* **98**, 161912 (2011)

[Ort04] G. Ortner, D. R. Yakovlev, M. Bayer, S. Rudin, T. L. Reinecke, S. Fafard, Z. Wasilewski, and A. Forchel, *Phys. Rev. B* **70**, 201301 (2004)

[Pet11] P. Gold, 'Magneto-optische Spektroskopie an Quantenpunkt-Mikrosäulenresonatoren', Diplomarbeit, (2011), unpublished

[Pod08] P. Podemski, G. Sęk, K. Ryczko, J. Misiewicz, S. Hein, S. Höfling, A. Forchel, and G. Patriarche, *Appl. Phys. Lett.* **93**, 071910 (2008)

[Pol06] P. Poloczek, G. Sęk, J. Misiewicz, A. Löffler, J. P. Reithmaier, and A. Forchel, *J. Appl. Phys.* **100**, 013503 (2006)

[Pre08] D. Press, T. D. Ladd, B. Zhang, and Y. Yamamoto, *Nature* **456**, 218 (2008)

[Pry98] C. Pryor, *Phys. Rev. B* **57**, 7190 (1998)

[Rei04] J. P. Reithmaier, G. Sęk, A. Löffler, C. Hofmann, S. Kuhn, S. Reitzenstein, L. Keldysh, V. Kulakovskii, T. L. Reinecke, and A. Forchel, *Nature* **432**, 197 (2004)

[Rei07] J. P. Reithmaier, G. Eisenstein, and A. Forchel, *Proc. of IEEE* **95**, 1779 (2007)

[Rei09] S. Reitzenstein, S. Münch, P. Franeck, A. Rahimi-Iman, A. Löffler, S. Höfling, L. Worschech, and A. Forchel, *Phys. Rev. Lett.* **103**, 127401 (2009)

[Rid07] P. Ridha, L. Liore, A. Fiore, G. Patriarche, M. Mexis, and P. M. Smowton, *Appl. Phys. Lett.* **91**, 191123 (2007)

[Roy10] R. Roy-Guay, P. J. Poole, and S. Raymond, *Semicond. Sci. Tech.* **25**, 045001 (2010)

[Ru_03] E. C. Le Ru, P. Howe, T. S. Jones, and R. Murray, *Phys. Rev. B* 67, 165303 (2003)

[Rud05] W. Rudno-Rudziński, G. Sęk, K. Ryczko, R. Kudrawiec, J. Misiewicz, A. Somers, R. Schwertberger, J. P. Reithmaier, and A. Forchel, *Appl. Phys. Lett.* **86**, 101904 (2005)

[Rud06] S. Rudin, T. L. Reinecke, and M. Bayer, *Phys. Rev. B* **74**, 161305 (2006)

[Rud06-1] W. Rudno-Rudziński, R. Kudrawiec, P. Podemski, G. Sęk, J. Misiewicz, A. Somers, R. Schwertberger, J. P. Reithmaier, and A. Forchel, *Appl. Phys. Lett.* **89**, 031908 (2006)

[Ryc13] K. Ryczko, G. Sęk, and J. Misiewicz, 'Lateral coupling within the ensemble of InAs/InGaAlAs/InP quantum dashes', submitted to *Acta Phys. Pol. A* (2013)

[Sai08] T. Saito, H. Ebe, Y. Arakawa, and M. Sugawara, *Phys. Rev. B* **77**, 195318 (2008)

[Sal05] B. Salem, N. Chauvin, T. Benyattou, G. Guillot, C. Bru-Chevallier, G. Bremond, C. Monat, P. Rojo-Romeo, and M. Gendry, *Nanotechnology* **16**, 444 (2005)

[Sau05] A. Sauerwald. T. Kümmel, G. Bacher, A. Somers, R. Schwertberger, J. P. Reithmaier, and A. Forchel, *Appl. Phys. Lett.* **86**, 253112 (2005)

[Sch93] R. W. Schoenlein, D. M. Mittleman, J. J. Shiang, A. P. Alivisatos, and C. V. Shank, *Phys. Rev. Lett.* **70**, 1014 (1993)

[Sch02] R. Schwertberger, D. Gold, J. P. Reithmaier, and A. Forchel, *IEEE Photonics Technol. Lett.* **14**, 735 (2002)

[Sch07] A. Schliwa, M. Winkelnkemper, and D. Bimberg, *Phys. Rev. B* **76**, 205324 (2007)

[Sch09] A. Schliwa, M. Winkelnkemper, and D. Bimberg, *Phys. Rev. B* **79**, 075443 (2009)

[Seg05] R. Seguin, A. Schliwa, S. Rodt, K. Pötschke, U. W. Pohl, and D. Bimberg, *Phys. Rev. Lett.* **95**, 257402 (2005)

[Sęk01] G. Sęk, K. Ryczko, J. Misiewicz, M. Bayer, F. Klopf, J. P. Reithmaier, and A. Forchel, *Solid State Commun.* **117**, 401 (2001)

[Sęk10] G. Sęk, A. Musiał, P. Podemski, M. Syperek, J. Misiewicz, A. Löffler, S. Höfling, L. Worschech, and A. Forchel, *J. Appl. Phys.* **107**, 096106 (2010)

[Sen05] P. Senellart, E. Peter, J. Hours, A. Cavanna, and J. Bloch, *Phys. Rev. B* **72**, 115302 (2005)

[She08] W. Sheng, and S. J. Xu, *Phys. Rev. B* **77**, 113305 (2008)

[Sri07] N. Sritirawisarn, F. W. M. van Otten, T. J. Eijkemans, and R. Nötzel, *J. Cryst. Growth* **305**, 63 (2007)

[Sri09] N. Sritirawisarn, and R. Nötzel, *Jpn. J. Appl. Phys.* **48**, 04C121 (2009)

[Sti99] O. Stier, M. Grundmann, and D. Bimberg, *Phys. Rev. B* **59**, 5688 (1999)

[Sti01] O. Stier, A. Schliwa, R. Heitz, M. Grundmann, and D. Bimberg, *Phys. Status Solidi b* **224**, 115 (2001)

[Sti03] A. Stintz, T. J. Rotter, and K. J. Malloy, *J. Crys. Growth* **255**, 266 (2003)

[Sug95] M. Sugawara, *Phys. Rev. B* **51**, 10743 (1995)

[Syp10] M. Syperek, A. Musiał, G. Sęk, P. Podemski, J. Misiewicz, A. Löffler, S. Höfling, L. Worschech, and A. Forchel, *AIP Conf. Proc.* **1399**, 563 (2010)

[Syp13] M. Syperek, Ł. Dusanowski, J. Andrzejewski, W. Rudno-Rudziński, G. Sęk, J. Misiewicz, and F. Lelarge, 'Carrier relaxation dynamics in InAs/GaInAsP/InP(001) quantum dashes emitting near 1.55 μm', accepted to *Appl. Phys. Lett.* (2013)

[Syp13-1] M. Syperek, M. Baranowski, G. Sęk, J. Misiewicz, A. Löffler, S. Höfling, S. Reitzenstein, M. Kamp, and A. Forchel, *Phys. Rev. B* **87**, 125305 (2013)

[Tsi01] E. Tsitsishvili, *Phys. Status Solidi b* **228**, 671 (2001)

[Ukh02] A. A. Ukhanov, R. H. Wang, T. J. Rotter, A. Stintz, L. F. Lester, P. G. Eliseev, and K. J. Malloy, *Appl. Phys. Lett.* **81**, 981 (2002)

[Usk01] A. V. Uskov, I. Magnusdottir, B. Tromborg, J. Mørk, and R. Lang, *Appl. Phys. Lett.* **79**, 1679 (2001)

[Usm11] M. Usman, T. Inoue, Y. Harda, G. Klimeck, and T. Kita, *Phys. Rev. B* **84**, 115321 (2011)

[Ust98] V. M. Ustinov, A. E. Zhukov, A. Y. Egorov, A. R. Kovsh, S. V. Zaitsev, N. Y. Gordeev, V. I. Kopchatov, N. N. Ledentsov, A. F. Tsatsul'nikov, B. V. Volovik, P. S. Kop'ev, Z. I. Alferov, S. S. Ruvinov, Z. Liliental-Weber, and D. Bimberg, *Electron. Lett.* **34**, 670 (1998)

[Utz96] T. Utzmaier, P. A. Postigo, J. Tamaya, R. Garcia, and F. Briones, *Appl. Phys. Lett.* **69**, 2674 (1996)

[Var67] Y. P. Varshni, *Physica (Amsterdam)* **34**, 149 (1967)

[Vog07] M. M. Vogel, S. M. Ulrich, R. Hafenbrak, P. Michler, L. Wang, A. Rastelli, and O. G. Schmidt, *Appl. Phys. Lett.* **91**, 051904 (2007)

[Vur01] I. Vurgaftman, J. R. Meyer, and L. R. Ram-Mohan, *J. Appl. Phys.* **89**, 5815 (2001)

[Wal01] T. Walther, A. G. Cullis, D. J. Norris, and M. Hopkinson, *Phys. Rev. Lett.* **86**, 2381 (2001)

[Wan01] R. H. Wang, A. Stintz, P. M. Varangis, T. C. Newell, H. Li, K. J. Malloy,and L. F. Lester, *IEEE Photon. Technol. Lett.* **13**, 767 (2001)

[Wan08] B. R. Wang, B. Q. Sun, Y. Ji, X. M. Dou, Z. Y. Xu, Zh. M. Wang, and G. J. Salamo, *Appl. Phys. Lett.* **93**, 011107 (2008)

[Wei05] J. H. Wei, and K. S. Chan, *J. Appl. Phys.* **97**, 123524 (2005)

[Wim06] M. Wimmer, S. V. Nair, and J. Shumway, *Phys. Rev. B* **73**, 165305 (2006)

[Yam09] Y. Yamamoto, T. D. Ladd, D. Press, S. Clark, K. Sanaka, C. Santori, D. Fattal, K. M. Fu, S. H¨ofling, S. Reitzenstein, and A. Forchel, *Physica Scripta* **T137**, 014010 (2009).

[Yu_99] P. Yu, W. Langbein, K. Loesson, J. M. Hvam, N. N. Ledentsov, D. Bimberg, V. M. Ustinov, A. Yu. Egorov, A. E. Zhukov, A. F. Tsatsul'nikov, and Yu. G. Musikhin, *Phys. Rev. B* **60**, 16680 (1999)

[Yua01] Z. L. Yuan, E. R. S. D. Foo, J. F. Ryan, D. J. Mowbray, M. S. Skolnick, and M. Hopkins, *Phys. Status Solidi b* **224**, 409 (2001)

[Zie10] M. Zieliński, M. Korkusiński, and P. Hawrylak, *Phys. Rev. B* **81**, 085301 (2010)

[Zie12] M. Zieliński, *Phys. Rev. B* **86**, 115424 (2012)